

THÈSE DE DOCTORAT EN COTUTELLE

ÉTUDE DE L'EFFET DU TRAITEMENT THERMIQUE ET DU  
TAUX DE REFROIDISSEMENT SUR LES PROPRIÉTÉS D'HYDROGÉNATION  
DES ALLIAGES TIFE AVEC ADDITIFS

*STUDY OF THE EFFECT OF HEAT TREATMENT AND COOLING RATE  
ON HYDROGENATION OF TIFE ALLOYS WITH ADDITIVES*

THÈSE PRÉSENTÉE À  
L'UNIVERSITÉ DU QUÉBEC À TROIS-RIVIÈRES  
ET À  
INDIAN INSTITUTE OF TECHNOLOGY BOMBAY  
COMME EXIGENCE PARTIELLE DU  
DOCTORAT EN SCIENCES DE L'ÉNERGIE ET DES MATÉRIAUX

PAR  
ABHISHEK KUMAR PATEL

OCTOBRE 2020

Université du Québec à Trois-Rivières

Service de la bibliothèque

Avertissement

L'auteur de ce mémoire ou de cette thèse a autorisé l'Université du Québec à Trois-Rivières à diffuser, à des fins non lucratives, une copie de son mémoire ou de sa thèse.

Cette diffusion n'entraîne pas une renonciation de la part de l'auteur à ses droits de propriété intellectuelle, incluant le droit d'auteur, sur ce mémoire ou cette thèse. Notamment, la reproduction ou la publication de la totalité ou d'une partie importante de ce mémoire ou de cette thèse requiert son autorisation.

# Study of the effect of heat treatment and cooling rate on hydrogenation of TiFe alloys with additives

*Submitted in partial fulfilment of the requirements  
of the degree of*

**Doctor of Philosophy**

*By:*

***Abhishek Kumar Patel***

*(Roll no. 121170009)*

Under the supervision of:

**Prof. Pratibha Sharma**

**And**

**Prof. Jacques Huot**



***Department of Energy Science & Engineering***

***IIT Bombay***

2020

## Thesis Approval

This thesis entitled “Study of the effect of heat treatment and cooling rate on hydrogenation of TiFe alloys with additives” by Abhishek Kumar Patel is approved for the degree of Doctor of Philosophy.

### Examiners



---

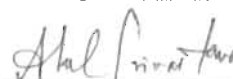
Prof. Anil Kumar Emadabathuni



---

Prof. Srinivas Seethamraju

### Chairman



---

Prof. Atul Srivastava

### Supervisors



Prof. Pratibha Sharma (IITB)



---

Prof. Jacques Huot (UQTR)

Dated: 14-08-2020

## **Declaration**

I declare that this written submission represents my ideas in my own words and where others' ideas or words have been included, I have adequately cited and referenced the original sources. I also declare that I have adhered to all principles of academic honesty and integrity and have not misrepresented or fabricated or falsified any idea/data/fact/source in my submission. I understand that any violation of the above will be cause for disciplinary action by the Institute and can also evoke penal action from the sources which have thus not been properly cited or from whom proper permission has not been taken when needed.



-----

Date: 05/08/2020

Abhishek Kumar Patel

(121170009)

# **Dedication**

To my Parents

## Résumé

Des considérations économiques et environnementales nécessitent de remplacer les combustibles fossiles par des options renouvelables. Dans cette perspective, l'hydrogène est considéré comme un bon candidat comme vecteur énergétique pour les applications mobiles et stationnaires. Les moyens classiques pour stocker l'hydrogène sont sous forme liquide à très basse température (20K) ou à l'état gazeux dans des réservoirs haute pression (350 ou 700bar). Cependant, ces deux techniques présentent des défis liés à la manipulation et à la sécurité liées à la basse température ou à la haute pression. Le stockage à l'état solide est une méthode sûre, volumétriquement efficace et simple pour le stockage de l'hydrogène. Les hydrures métalliques sont de bons candidats parmi les matériaux de stockage à l'état solide, où l'hydrogène est chimiquement lié à des atomes métalliques. Dans les hydrures métalliques, l'hydrogène peut être stocké de manière compacte à température et pression modérées, rendant ainsi cette technique particulièrement sûre. Cependant, pour utiliser les hydrures métalliques à grande échelle, le coût des hydrures métalliques doit être réduit. Le but de cette étude est de comprendre l'effet comparatif de Zr, Mn et V sur les caractéristiques d'hydrogénation de l'alliage TiFe, en utilisant du Fe de qualité industrielle (ASTM 10005) et Ti (ASTM B265 grade 1) comme matière première. L'effet du traitement thermique et de la vitesse de refroidissement ont également été étudiés afin d'optimiser les paramètres de synthèse. La structure cristalline des alliages TiFe avec et sans ajout d'additifs a été étudiée par diffraction des rayons X. La morphologie et la composition ont été étudiées respectivement par microscopie électronique à balayage (SEM) et spectroscopie à rayons X à dispersion d'énergie (EDX). Nous avons constaté que l'ajout de manganèse rend possible l'activation à température ambiante, mais la cinétique était très lente. L'alliage avec 2% en poids de Zr n'a pas absorbé d'hydrogène. Cependant, avec l'addition de 4% en poids de Zr, l'alliage a absorbé très rapidement 1,2% en poids d'hydrogène. Une synergie a été trouvée lorsque le zirconium a été ajouté avec du manganèse. L'alliage avec 1% en poids de Mn et 2% en poids de Zr avait une meilleure cinétique que l'alliage ayant seulement Mn ou seulement Zr. La capacité maximale d'hydrogène obtenue était également plus élevée, atteignant ~ 1,8% en poids en 7 heures. Une combinaison de 4% en poids de Zr et de 2% en poids de Mn a absorbé 2% en poids d'hydrogène en 5 heures. L'alliage avec 2 et 4% en poids de V n'a pas du tout absorbé d'hydrogène. Cependant, la combinaison de 2% en poids de Zr + 2% en poids de V conduit à une meilleure cinétique que l'alliage avec un additif individuel (Zr ou V) et absorbe 1,6% en poids d'hydrogène. La combinaison de trois additifs

Zr + Mn + V avec chacun à un niveau de concentration de 2% en poids s'est avérée également bénéfique en termes d'amélioration de la cinétique et de minimisation du niveau de concentration des additifs. Une autre combinaison de Mn et V était également efficace pour l'activation de l'alliage TiFe à un niveau de concentration de 2% en poids Mn et 2% en poids V. L'étape limitative de vitesse  $v$  pour chaque alliage activé s'est avérée être contrôlée par diffusion avec une vitesse d'interface décroissante. Le principal effet du traitement thermique était de réduire l'abondance de la phase secondaire. Le changement dans la composition de la phase TiFe et des phases secondaires était relativement limité. Malgré les changements relativement mineurs dans les structures cristallines, la première cinétique d'hydrogénation était beaucoup plus lente et la capacité d'hydrogène plus petite pour les échantillons traités thermiquement par rapport à leurs homologues tels que coulés. Le mécanisme responsable de la cinétique d'hydrogénation plus lente peut être la modification de la composition chimique de l'interface entre la phase TiFe et la phase secondaire. L'effet de la vitesse de refroidissement a été étudié en utilisant un moule à gradins d'une épaisseur de 25, 13, 6 et 3 mm. Il a été constaté qu'une vitesse de refroidissement plus élevée conduit à une solidification rapide et une distribution plus fine de la phase secondaire. Il n'y avait aucun effet de la vitesse de refroidissement sur la composition chimique des différentes phases présentes pour toutes les épaisseurs de moule. Cependant, une vitesse de refroidissement plus rapide conduit à une cinétique de première hydrogénation plus rapide. La raison en est que la vitesse de la première cinétique d'hydrogénation est proportionnelle au périmètre entre la phase TiFe et la phase secondaire. Pendant l'activation, l'étape de limitation de la vitesse d'hydrogénation pour tous les alliages s'est avérée être une croissance 3D, diffusion contrôlée avec une vitesse d'interface décroissante. Le mécanisme de passerelle pour la cinétique améliorée de la première hydrogénation a été confirmé et il a été constaté que l'hydrogène entre d'abord dans la phase secondaire puis passe à la phase principale de TiFe. Quatre échantillons de  $Ti_xFe_{2-x} + 4\%$  en poids Zr, où  $x = 1.1, 1.05, 0.99, 0.94$  ont été préparés afin de comprendre l'effet de la phase riche en Ti sur la première cinétique d'hydrogénation de l'alliage TiFe. L'analyse de la microstructure et du diagramme de diffraction des rayons X révèle la formation de la phase principale TiFe avec des phases secondaires de type  $Ti_2Fe$  et  $TiFe_2$ . Lorsque  $x = 1.1$ , une distribution fine et homogène de la phase secondaire a été observée dans la microstructure de l'alliage TiFe. Lorsque le rapport Ti/Fe diminue, la première cinétique d'hydrogénation est plus lente et la capacité maximale d'hydrogène diminue également. Le meilleur alliage était  $Ti_{1.1}Fe_{0.9} + 4\%$  en poids de Zr en termes de capacité



maximale d'hydrogène et de cinétique.  $Ti_{1.1}Fe_{0.9}$  + 4% en poids Zr absorbe 2% en poids d'hydrogène et atteint sa capacité maximale en deux heures.

## Abstract

Economic and environmental considerations necessitate to replace the fossil fuels by renewable options. In this perspective, hydrogen is considered to be a good candidate as an energy carrier for mobile and stationary applications. The conventional ways to store hydrogen are in the liquid form at a very low temperature (20K) or in a gaseous state in high-pressure tanks (350 or 700bar). However, these two techniques have challenges associated with handling and safety related to either low temperature or high pressure. Solid state storage is a safe, volumetrically efficient and simple method for hydrogen storage. Metal hydrides are good candidate among the solid state storage materials, where the hydrogen is chemically bonded to metal atoms. In metal hydrides, the hydrogen could be stored in a compact way at moderate temperature and pressure thus making this technique particularly safe. However, in order to use metal hydrides on large scale, the cost of metal hydrides must be reduced. The aim of this study is to understand the comparative effect of Zr, Mn and V on hydrogenation characteristics of TiFe alloy, using industrial grade Fe (ASTM 10005) and Ti (ASTM B265 grade 1) as a raw material. Effect of heat treatment and cooling rate has also been studied in order to optimize synthesis parameters. Crystal structure of TiFe alloys with and without addition of additives were studied using X-ray diffraction. Morphology and composition were studied by Scanning electron microscopy (SEM) and energy dispersive X-ray spectroscopy (EDX) studies respectively.

We found that addition of manganese makes possible the activation at room temperature, but kinetics was very sluggish. Alloy with 2 wt% Zr did not absorb hydrogen. However, with addition of 4 wt% Zr, the alloy absorbed 1.2 wt% of hydrogen very fast. A synergetic effect was found when zirconium was added along with manganese. Alloy with 1 wt% Mn and 2 wt% Zr had better kinetics than the alloy having only Mn or only Zr. The maximum hydrogen capacity achieved was also higher, reaching ~ 1.8 wt% in 7 hours. Combination of 4 wt% Zr and 2 wt% Mn absorbed 2 wt% of hydrogen in 5 hours. Alloy with 2 and 4 wt% V did not absorb hydrogen at all. However, combination of 2 wt% Zr + 2 wt% V leads to better kinetics than the alloy with individual additive (Zr or V) and absorbs 1.6 wt% hydrogen. Combination of three additives Zr + Mn + V with each at a concentration level of 2 wt% was found to be also beneficial in terms of improving kinetics and minimizing the concentration level of additives. Another combination of Mn and V was also effective for the activation of TiFe alloy at concentration level of 2 wt% Mn and 2 wt% V. The

rate limiting step for each activated alloy was found to be diffusion controlled with decreasing interface velocity.

The main effect of heat treatment was to reduce the abundance of the secondary phase. Change in the composition of the TiFe phase and the secondary phases was relatively limited. Despite the relatively minor changes in crystal structures, the first hydrogenation kinetics was much slower and hydrogen capacity smaller for heat-treated samples compared to their as-cast counterparts. The mechanism responsible for the slower hydrogenation kinetics may be the modification in the chemical composition of the interface between the TiFe phase and the secondary phase.

Effect of cooling rate was studied by using a step mold with a thickness of 25, 13, 6 and 3 mm. It was found that higher cooling rate leads to a rapid solidification and finer distribution of the secondary phase. There was no effect of cooling rate on the chemical composition of the different phases present for all mold thicknesses. However, faster cooling rate leads to faster first hydrogenation kinetics. The reason is that rate of the first hydrogenation kinetic is proportional to the perimeter between the TiFe phase and the secondary phase. During activation, the hydrogenation rate limiting step for all alloys was found to be 3D growth, diffusion controlled with decreasing interface velocity. The gateway mechanism for the enhanced first hydrogenation kinetics has been confirmed and it was found that hydrogen entering first the secondary phase and then transfer to the main TiFe phase.

Four samples of  $\text{Ti}_x\text{Fe}_{2-x} + 4 \text{ wt\% Zr}$ , where,  $x = 1.1, 1.05, 0.99, 0.94$  was prepared in order to understand the effect of Ti-rich phase on the first hydrogenation kinetics of TiFe alloy. Microstructure and X-ray diffraction pattern analysis reveal the formation of TiFe main phase with  $\text{Ti}_2\text{Fe}$ -like and  $\text{TiFe}_2$ -like secondary phases. When  $x = 1.1$ , a fine and homogeneous distribution of secondary phase was seen in the microstructure of TiFe alloy. When Ti/Fe ratio decreases, first hydrogenation kinetics is slower and maximum hydrogen capacity also decreases. The best alloy was  $\text{Ti}_{1.1}\text{Fe}_{0.9} + 4 \text{ wt\% Zr}$  in terms of maximum hydrogen capacity and kinetics.  $\text{Ti}_{1.1}\text{Fe}_{0.9} + 4 \text{ wt\% Zr}$  absorbs 2 wt% of hydrogen and reaches its maximum hydrogen capacity within 2 hours.

## **Acknowledgement**

First and foremost, I would like to express my sincere gratitude towards my supervisors Prof. Pratibha Sharma and Prof. Jacques Huot for their excellent guidance, moral support, and valuable ideas throughout the journey of pursuing PhD from IIT Bombay and UQTR Canada through exchange program. I am thankful to my both supervisors for their helpful discussion, creating a good working environment, and providing the best laboratory facility.

I am heartily thankful to my research progress committee member, Prof. Sankara Sarma V Tatiparti, Prof. Prakash Chandra Ghosh and Prof. Srinivas Seethamraju for their valuable suggestions and queries, which help me to improve my thesis and the research works a lot. I am also thankful to HOD Prof. Rangan Banerjee for giving me the opportunity to pursue the doctoral degree in the DESE, IITB department and allowing me to join exchange program at UQTR Canada. I would like to thank Prof. Balasubramaniam Kavaipatti for his guidance during my M.Sc. project.

I would like to acknowledge my jury members Prof. Jean Hamelin and Prof. Adam Duong for their suggestions and valuable inputs during the PhD examination at UQTR Canada. I am grateful to CMQ (Quebec Metallurgy Center) and GKN powder metallurgy for providing me facilities at industrial scale. I am also thankful to Dr. Bernard Tougas and Dr. Chris Schade for their collaboration in this PhD project. Specially, I would like to thank Dr. Bernard Tougas for his help and providing me SEM and XRD facilities at CMQ and CEGEP, Trois-Rivières. I am heartily thankful to Mr. Cedric Garceau and Mr. Alexandre Duguay for their help and participation in this project. I would like to thank Queen Elizabeth Scholars (QES) for fellowship during my stay in Canada. Sincere thanks to Ms. Genevieve Cote for her help during joining the QES program at UQTR.

I am grateful to my senior IITB lab mates, Dr. Devendra Pareek, Dr. Joydev Manna, Dr. Binayak Roy, Dr. Bharati Patro for their helpful suggestions and invaluable help during my research journey. I would also like to thank my IITB lab mates Ms. Mahvash Afzal, Mr. Saurabh Tiwari, Mr. Vinit Kumar, Mr. Animesh Hajari, Mr. Meraj Alam, Ms. Meenakshi Sahu, Mr. Ravi Prakash, Ms. Ankita Bishnoi, Mr. Vishnulal, Mr. Nandlal for their helpful discussion and creating a good working and friendly environment. Specially, I am thankful to Saurabh and Vinit for their help and

moral support. I would like to give my best wishes to new researchers Mr. Ravi Prakash, Ms. Ankita Bishnoi, Mr. Vishnulal, for their PhD project. My sincere thanks to Mr. Rahul for his kind help whenever I needed.

I am thankful to my UQTR lab mates, Dr. Peng Lyu, Dr. Volatiana, Dr. Amol G. Kamble, Dr. Viney Dixit, and Mrs. Salma for their help during my stay in Canada. Specially, I would like to thank Dr. Peng Lyu for his help and suggestion during the conduction of experiment.

I am grateful to my BHU friends Mr. Abhijeet Singh, Mr. Ravi Kant Rai, Mr. Ajeet Yadav, Mr. Prateek Yadav, Mr. Amit Mishra for their help and encouragement during the time of M.Sc. and graduation. I would like to thank my friends in IITB Mr. Himanshu Singh, Mr. Vivek Singh, Mr. Shushant Singh, Mr. Anuj Singh, Mr. Sandeep Maurya, Mr. Vinay Yadav, Mr. Deepak Rai, Mr. Rishabh Kumar, Mr. Kisan Jaiswal, and Mr. Niteen Kumar for giving me moral support and providing me a friendly environment in IIT Bombay.

I am heartily thankful to my friends in Canada Mr. Midhun Mohan, Ms. Aneeshma Peter. Mr. Kiran Todkar, Mrs. Shweta Todkar, Mr. Sanil Rajak for making me feel like home in Canada and for their help during my stay in Canada. They were always with me and I believe they will be during my tough time.

I would like to thank my uncles and aunties (chacha, chachi and bua and fufa) who lives in Mumbai: Mr. Yogesh Singh, Mr. Umesh Singh, Mr. Ramasre Singh, Mr. Rambrat Singh, Mrs. Usha Singh, Mrs. Beena Singh, Mrs. Vimla Singh, Mrs. Kamla Singh for sharing the joy and happiness during festival times and for always being supportive during my tough times. I am thankful to my cousins who live in Mumbai: Shubhda, Vibha, Aabha, Kshijit, Namrata, Jaya, Sandhya, Kaushal, Divya, and Vaibhav for their love and support. I have great time in Mumbai with all of you.

I am thankful to my brothers Mr. Mukesh and Mr. Vikas for their love, belief and moral support. They always encourage me to give my best during all difficulties and challenges in life. Sincere thanks to my sister in law Mrs. Beena, Mrs. Pratima for their moral support during my difficult time.

Finally, I would like to thank my parents Mr. Dharendra Kumar Singh and Mrs. Asha Devi for their love, moral support and who worked hard and did whatever need to make my education possible and who never stopped encouraging me.

# Table of Contents

---

Chapter 1.....	1
Introduction	
.....	1
1.1 Hydrogen energy .....	1
1.2 Hydrogen as a fuel .....	1
1.3 Hydrogen storage.....	3
1.4 Compressed Hydrogen storage.....	4
1.5 Liquid Hydrogen storage.....	4
1.6 Hydrogen storage in solids .....	4
1.6.1 Physisorption .....	5
1.6.2 Chemisorption.....	5
1.6.2.1 Complex hydrides .....	5
1.6.2.2 Metal hydrides.....	6
1.7 Thermodynamics of Metal Hydrides .....	6
1.7.1 Effect of temperature increase .....	8
1.8 Hydriding process .....	10
1.9 AB <sub>5</sub> -type alloys.....	11
1.10 AB <sub>2</sub> -type (Lave phase) alloys .....	12
1.11 Solid solution alloys.....	13
1.12 A <sub>2</sub> B-type alloys.....	14
1.13 AB-type alloys.....	14
1.14 Motivation .....	15
1.15 Objectives.....	17
1.16 Thesis structure.....	17
Chapter 2.....	18

Literature review on TiFe

---

.....	18
2.1 Introduction .....	18
2.2 Effect of substitution and additives on TiFe alloy .....	19
2.3 Mechanical activation processes.....	26
Chapter 3.....	28

Experimental Details

---

.....	28
3.1 Introduction .....	28
3.2 Starting material .....	28
3.3 Alloy synthesis .....	28
3.3.1 TiFe with Zr, V and Mn (synthesized by Industry).....	29
3.3.2 Heat treatment.....	31
3.3.3 Cooling rate .....	31
3.3.4 Synthesis of $Ti_xFe_{2-x} + 4 \text{ wt\% Zr}$ , ( $x = 1.1, 1.05, 0.99, 0.94$ ) .....	32
3.4 Alloy characterization .....	33
3.4.1 Scanning electron microscopy (SEM).....	33
3.4.2 X-ray diffraction .....	34
3.4.3 X-ray fluorescence .....	35
3.4.4 Sieverts apparatus .....	36
Chapter 4.....	39

Microstructure and hydrogen storage properties of TiFe alloys with Zr, V and Mn as additives

---

.....	39
4.1 Introduction .....	39
4.2 Activation kinetics of alloys (in granules form) shown in Table 3.1 .....	39



4.3 TiFe alloys with only Zr, only Mn and combination of Zr + Mn as additives .....	41
4.3.1 Result and discussion .....	42
4.3.1.1 Morphology .....	42
4.3.1.2 Structural characterization .....	48
4.3.1.3 Activation kinetics.....	51
4.3.1.4 Rate limiting step of first hydrogenation .....	53
4.3.2 Summary .....	55
4.4 TiFe alloy with V only, Zr + V and combination of Zr + Mn + V as additives .....	56
4.4.1 Result and discussion .....	57
4.4.1.1. Morphology.....	57
4.4.1.2. Structural characterization .....	61
4.4.1.3. Activation kinetics.....	62
4.4.1.4 Rate limiting step of first hydrogenation .....	63
4.4.2 Summary .....	64
4.5 TiFe alloy with Mn + V as additives .....	65
4.5.1 Result and discussion .....	65
4.5.1.1. Morphology.....	65
4.5.1.2. Structural characterization .....	69
4.5.1.3 Activation kinetics.....	70
4.4.1.4 Rate limiting step of first hydrogenation .....	71
4.5.2 Summary .....	72
Chapter 5.....	73
Effect of heat treatment on microstructure and hydrogenation properties of TiFe + X wt% Zr (X = 4, 8)	
.....	73
5.1 Introduction .....	73
5.2 Result and discussion.....	73
5.2.1 Morphology .....	73
5.2.1.1 TiFe with 4 wt% Zr (as-cast and heat-treated).....	75

5.2.1.2 TiFe with 8 wt% Zr (as-cast and heat-treated).....	77
5.2.2 Structural characterization.....	78
5.2.3 Activation kinetics.....	79
5.3 Summary.....	80
Chapter 6.....	81
Effect of cooling rate on the microstructure and hydrogen storage properties of TiFe with 4 wt% Zr as an additive.....	81
<hr/>	
.....	81
6.1 Introduction.....	81
6.2 Result and discussion.....	81
6.2.1 Morphology.....	81
6.2.2 Structural characterization.....	85
6.2.3 Activation kinetics.....	88
6.3 Summary.....	91
Chapter 7.....	92
Microstructure and hydrogen storage properties of $Ti_xFe_{2-x} + 4 \text{ wt\% Zr}$ , ( $x = 1.1, 1.05, 0.99, 0.94$ )	
<hr/>	
.....	92
7.1 Introduction.....	92
7.2 Result and discussion.....	93
7.2.1 Morphology.....	93
7.2.2 Structural characterization.....	97
7.2.3 Activation kinetics.....	99
7.3 Summary.....	100
Chapter 8.....	101

Conclusion and future work

---

..... 101

List of publications and conferences

---

..... 102

Reference

---

..... 104

## List of Figures

---

Figure 1.1: P-C-T curve for metal hydrides .....	7
Figure 1.2: (a) The effect of temperature on PCT curve (b) van't Hoff plot of equilibrium pressure with respect to $1/T$ .....	8
Figure 1.3: Different steps in the hydrogenation process.....	11
Figure 2.1: P-C-T plot for FeTi-H system.....	18
Figure 2.2: First hydrogenation curve of pure TiFe alloy and with 4 wt% additives under 2 MPa $H_2$ at 40 °C .....	20
Figure 2.3: Desorption Curve of TiFe with 4 wt% additives under 0.1 MPa $H_2$ at 40 °C .....	21
Figure 2.4: PCT curve of TiFe with different additives .....	21
Figure 2.5: The activation behaviour of $Ti_{0.95}FeZr_{0.05}$ , $TiFe_{0.95}Zr_{0.05}$ and $TiFeZr_{0.05}$ alloys at room temperature under 2 MPa hydrogen pressure .....	22
Figure 2.6: Initial hydriding curves of $TiFe_{0.9}Mn_{0.1}Ce_x$ ( $x = 0, 0.02, 0.04, 0.06$ ) at 353 K and under initial pressure of 4.0 MPa.....	23
Figure 3.1: Arc melting facility at UQTR and Induction melting facility at industry.....	29
Figure 3.2: Step molds for varying cooling rate during alloy synthesis .....	32
Figure 3.3: The set-up of scanning electron microscope .....	34
Figure 3.4: Schematic diagram for the formulation of Bragg's diffraction .....	35
Figure 3.5: Schematic diagram of production of X-ray fluorescence radiation .....	36
Figure 3.6: Real time picture and schematic diagram of Sieverts apparatus with different components.....	37
Figure 4.1: Activation curve of TiFe + 2 wt% Mn + 4 wt% Zr (in granules form) at room temperature under 20 bar hydrogen pressure.....	39
Figure 4.2: Activation curve of TiFe + 2 wt% Mn + 4 wt% Zr at room temperature, 75 °C, and 90 °C under 40 bar hydrogen pressure.....	40
Figure 4.3: Microstructure of (a) as-cast TiFe alloy, TiFe with (b) 2 wt% Zr, (c) 4 wt% Zr, (d) 1 wt% Mn, (e) 6 wt % Mn, (f) 1 wt% Mn + 2 wt% Zr and (g) 2 wt% Mn + 4 wt% Zr .....	43
Figure 4.4: Microstructure of TiFe + 2 wt% Mn + 4 wt% at 20 $\mu m$ scale.....	44
Figure 4.5: EDX analysis and elemental mapping of TiFe .....	44
Figure 4.6: EDX analysis of TiFe with Zr as additive (a) 2 wt% Zr and (b) 4 wt% Zr .....	45

Figure 4.7: EDX analysis of TiFe alloy with Mn (a) 1 wt%, (b) 6 wt%.....	46
Figure 4.8: EDX analysis of TiFe alloy with Zr and Mn .....	47
Figure 4.9: X-ray pattern of TiFe alloys without any additives and with Zr, Mn, and Zr + Mn as additives.....	49
Figure 4.10: Activation kinetics of all alloys at room temperature under 20 bar hydrogen pressure .....	52
Figure 4.11: Linear fitting of each rate limiting step model for each activated alloy (a) for 4 wt % Zr, (b) 1 wt% Mn, (c) 6 wt% Mn, (d) 1 wt% Mn + 2 wt% Zr and (e) 2 wt% Mn + 4 wt% Zr .....	54
Figure 4.12: Back-scattered electron micrograph of TiFe alloy with (a) 2 wt% V, (b) 4 wt% V, (c) 2 wt% Zr + 2 wt% V and (d) 2 wt% Zr + 2 wt% V + 2 wt% Mn as additives.....	57
Figure 4.13: EDX analysis of TiFe with the addition of V only(a) 2 wt% V and (b) 4 wt% V ...	58
Figure 4.14: EDX analysis of TiFe with the simultaneous addition of 2 wt% Zr + 2 wt% V .....	59
Figure 4.15: EDX analysis of TiFe alloy with the simultaneous addition of 2 wt% Zr + 2 wt% V + 2 wt% Mn .....	60
Figure 4.16: X-ray pattern of TiFe alloys with the addition of V only, Zr + V, and Zr + V + Mn .....	61
Figure 4.17: Activation kinetics of TiFe alloy with V, Zr + V and Zr + V + Mn under 20 bar H <sub>2</sub> pressure at room temperature.....	62
Figure 4.18: Linear fitting of each rate limiting step model for each activated alloy.....	63
Figure 4.19: Back-scattered micrograph of TiFe alloy with (a) 2 wt% Mn + 1 wt% V, (b) 2 wt% Mn + 2 wt% V, (c) 2 wt% Mn + 4 wt% V and (d) 4 wt% Mn + 4 wt% V as additives .....	66
Figure 4.20: EDX analysis of TiFe alloy with the combination of (a) 2wt% Mn + 1 wt% V, (b) 2 wt% Mn + 2 wt% V, (c) 2 wt% Mn + 4 wt% V and (d) 4 wt% Mn + 4 wt% V as additives .....	67
Figure 4.21: X-ray pattern of TiFe alloys with the combination of Mn + V as additives.....	69
Figure 4.22: First hydrogenation curve of TiFe alloys with the combination of Mn + V as additives at room temperature and 20 bar hydrogen pressure .....	70
Figure 4.23: Linear regression of different kinetic model for each TiFe alloy with the combination of Mn and V as additives.....	71
Figure 5.1: Backscatter electron micrograph of TiFe + X wt% Zr (X= 4, 8) alloys before (a, c) and after heat treatment (b, d) .....	74

Figure 5.2: Elemental mapping of TiFe + X wt% Zr (X= 4, 8) alloys before (a, c) and after heat treatment (b, d).....	75
Figure 5.3: EDX analysis of TiFe + 4wt% Zr as-cast (a) and after heat treatment (b).....	76
Figure 5.4: EDX analysis of TiFe + 8 wt% Zr as cast (a) and after heat treatment (b) .....	77
Figure 5.5: X-ray diffraction patterns of TiFe + X wt% Zr (X = 4, 8) as-cast and heat-treated at 1173 K .....	78
Figure 5.6: First hydrogenation curve of TiFe + X wt% Zr (X = 4, 8) alloys before and after heat treatment .....	79
Figure 6.1: Backscattered micrographs of TiFe + 4 wt% Zr at different step mold thickness (a) 25 mm, (b) 13 mm, (c) 6 mm and (d) 3 mm.....	82
Figure 6.2: EDX analysis with mapping of an alloy having a 25 mm thickness of step mold .....	83
Figure 6.3: X-ray diffraction patterns of each alloy at a different thickness of step mold .....	86
Figure 6.4: Activation at room temperature and under 20 bars of hydrogen of TiFe+4wt% Zr at different thicknesses of step mold.....	88
Figure 6.5: Linear fitting of each rate limiting step model for 3 mm thickness .....	90
Figure 6.6: Activation kinetics rate constant as a function of the perimeter of the secondary phase .....	91
Figure 7.1: Ti-Fe binary phase diagram.....	92
Figure 7.2: Back-scattered micrograph of $Ti_xFe_{2-x}$ with 4 wt% Zr as additive, where $x = 1.1, 1.05, 0.99$ and $0.94$ .....	94
Figure 7.3: Chemical composition analysis of $Ti_xFe_{2-x}$ with 4 wt% Zr as additive, where $x = 1.1, 1.05, 0.99$ and $0.94$ .....	95
Figure 7.4: X-ray diffraction patterns of $Ti_xFe_{2-x}$ with 4 wt% Zr as additive, where $x = 1.1, 1.05, 0.99$ and $0.94$ .....	98
Figure 7.5: Activation kinetics of $Ti_xFe_{2-x}$ with 4 wt% Zr as additive at room temperature under 20 bar hydrogen pressure .....	100

## List of Tables

---

Table 1.1: Properties of hydrogen fuel and other conventional fuels .....	2
Table 1.2: Technical targets: onboard hydrogen storage systems .....	3
Table 1.3: Hydrogen absorption/desorption properties of various intermetallic hydrides .....	15
Table 2.1: The hydrogenation properties of various substituted TiFe alloys.....	24
Table 2.2: The hydrogenation properties of TiFe via different mechanical activation methods...27	
Table 3.1: Chemical composition (in mass %) of samples synthesized by GKN Powder Metallurgy.....	30
Table 4.1: Bulk chemical analysis: nominal and as measured by XRF (X-ray fluorescence) spectrometer of all alloys. Uncertainty on all values is $\pm 1$ at. %.....	41
Table 4.2: Chemical composition of different phases present in TiFe (uncertainty on all values is $\pm 1$ ) .....	45
Table 4.3: Chemical composition of each phase present in alloys with Zr only as additive (uncertainty on all values is $\pm 1$ ).....	46
Table 4.4: Chemical composition of different phases present in each alloy having Mn (uncertainty on all values is $\pm 1$ ).....	47
Table 4.5: Chemical composition of different phases present in each alloy having Zr and Mn (uncertainty on all values is $\pm 1$ ).....	48
Table 4.6: Phase fraction, lattice parameter and crystallite size for each alloy composition .....	50
Table 4.7: Model equations for rate limiting step determination .....	53
Table 4.8: Adjusted $R^2$ value for the linear regression of Model equations shown in Table 4.7 ..	55
Table 4.9: Bulk chemical analysis: nominal and as measured by XRF (X-ray fluorescence) spectrometer of all alloys. Uncertainty on all values is $\pm 1$ at%.....	56
Table 4.10: Chemical composition of each phase present in alloys with V only (uncertainty on all values is $\pm 1$ ).....	58
Table 4.11: Chemical composition of each phase present in TiFe with the simultaneous addition of 2 wt% Zr + 2 wt% V (uncertainty on all values is $\pm 1$ ) .....	59
Table 4.12: Chemical composition of TiFe + 2 wt% Zr + 2 wt% V + 2 wt% Mn (uncertainty on all values is $\pm 1$ ).....	60
Table 4.13: Adjusted $R^2$ value for the linear regression of different kinetic model .....	64

Table 4.14: Bulk chemical analysis: nominal and as measured by XRF (X-ray fluorescence) spectrometer of all alloys. Uncertainty on all values is $\pm 1$ at. %.....	65
Table 4.15: Chemical composition of area 1 (Grey phase) in all alloys (uncertainty on all values is $\pm 1$ ).....	67
Table 4.16: Chemical composition of area 2 (dark grey phase) in all alloys (uncertainty on all values is $\pm 1$ ).....	68
Table 4.17: Chemical composition of area 3 (light grey phase) in all alloys (uncertainty on all values is $\pm 1$ ).....	68
Table 4.18: Adjusted $R^2$ value for linear fitting of different kinetic model .....	72
Table 5.1: Area percentages of different phases for TiFe + X wt% Zr micrographs shown in Figure 4.1. Uncertainty on all values is $\pm 1$ .....	74
Table 5.2: Chemical compositions of TiFe + 4 wt% Zr in as-cast and heat-treated states. Uncertainty on all values is $\pm 1$ .....	76
Table 5.3: Chemical compositions of TiFe + 8 wt% Zr in as-cast and heat-treated states. Uncertainty on all values is $\pm 1$ .....	77
Table 5.4: Lattice parameter and crystallite size of all alloys .....	79
Table 6.1: Perimeter of the secondary phase over the total area of micrograph as calculated by ImageJ software.....	83
Table 6.2: Chemical composition of grey phase (Area 1) of TiFe + 4 wt% Zr at the different cooling rate. Uncertainty on all values is $\pm 1$ at. % .....	84
Table 6.3: Chemical composition of light grey phase (Area 2) of TiFe + 4 wt% Zr at the different cooling rate. Uncertainty on all values is $\pm 1$ at. % .....	84
Table 6.4: Chemical composition of bright phase (Area 3) of TiFe + 4 wt% Zr at the different cooling rate. Uncertainty on all values is $\pm 1$ at. % .....	85
Table 6.5: The weighted profile factor R-factor ( $R_{wp}$ ) and the expected R-factor ( $R_{exp}$ ) in Rietveld's analysis for each alloy .....	86
Table 6.6: Phase fraction, lattice parameter and crystallite size of each alloy having different thicknesses .....	87
Table 6.7: Rate constant in case of diffusion model equation for each thickness. Error on the last significant digit is in parentheses.....	90



Table 7.1: Area fraction (%) of different phases in the micrograph of  $Ti_xFe_{2-x}$  with 4 wt% Zr as additive, where  $x = 1.1, 1.05, 0.99$  and  $0.94$  (uncertainty on all values is  $\pm 1$ ).....93

Table 7.2: Chemical composition of each phase for  $x = 1.1$  (uncertainty on all values is  $\pm 1$ ) ...96

Table 7.3: Chemical composition of each phase for  $x = 1.05$  (uncertainty on all values is  $\pm 1$ ) ..96

Table 7.4: Chemical composition of each phase for  $x = 0.99$  (uncertainty on all values is  $\pm 1$ ) ..97

Table 7.5: Chemical composition of each phase for  $x = 0.94$  (uncertainty on all values is  $\pm 1$ ) ..97

Table 7.6: Evaluated Phase fraction, lattice parameter and crystallite size values for each phase in of  $Ti_xFe_{2-x}$  alloys with 4 wt% Zr as additive .....99

## Abbreviation

---

XRD (X-ray diffraction)

SEM (Scanning electron microscope)

EDX (Energy dispersive X-ray spectroscopy)

JMA (Johnson, Mehl, and Avrami )

GB3D (Ginstling-Brounshtein three dimensional)

# Chapter 1

## Introduction

---

### 1.1 Hydrogen energy

Evolution of industrial sectors and increase in human population increased the global energy demand. Energy systems of most of the countries worldwide depend on fossil fuels (coal, oil and natural gas). Emission of CO<sub>2</sub> and other greenhouse gases due to the intensive use of these fossil fuels necessitates the development of alternative clean energy systems [1, 2]. These alternative clean energy systems could be developed using the renewable and sustainable energy resources such as solar, wind, wave and geothermal. Dependence of solar and wind energy on weather conditions limits the use of these renewable resources-based energy system. Wave energy and geothermal energy are strongly location dependent. The intermittency associated with most of the renewables impose the requirement of storage integrated with these so as to have an uninterrupted supply of energy and meet the demand.

One of the alternative solutions to tackle the current energy crisis and environmental concerns is considered to be hydrogen economy. Hydrogen is a potential energy carrier and can store and transport energy easily due to its light weight, high gravimetric energy density. Hydrogen is the most abundant element but only found in compound form, i.e. water and hydrocarbon; only 1% exists as molecular hydrogen. Thus, the first issue in developing hydrogen economy is the large-scale production of hydrogen via economic and environment friendly routes. Water splitting using solar, photoelectrochemical and nuclear are very promising and might lead to cost reduction in hydrogen production. Hydrogen economy includes the productions, storage, distribution and usage of hydrogen. Hydrogen based energy conversion devices are more efficient for e.g. a fuel cell, further the only by product released on producing electricity is water.

### 1.2 Hydrogen as a fuel

Hydrogen is the lightest of all elements. Its combustion results in water as the main byproduct i.e. it's non-polluting. It is colorless, odorless and nontoxic in gaseous form. Hydrogen gas has very low density of 0.08 kg/m<sup>3</sup> (7 % of the density of air) at normal temperature (293.15 K) and pressure (101.325 kPa). However, liquid hydrogen has a density 71 kg/m<sup>3</sup> (7% of water density). In liquid form, hydrogen has boiling point (~ 20.3 K) because of which it requires a very energy intensive

liquefaction process and insulation to maintain liquid state. There are several advantages of using hydrogen as a fuel over other fuels. A technical comparison of properties of hydrogen as a fuel with other conventional fuels is shown in **Table 1.1**. Hydrogen has the best energy to weight ratio (heating value) of any fuel, but its energy to volume ratio is poor. The HHV (higher heating value) of hydrogen is 141.78 MJ/kg of H<sub>2</sub> and its lower heating value is 120 MJ/kg of H<sub>2</sub>.

Other properties listed in the lower half of **Table 1.1** are important for safety consideration. Diffusivity of hydrogen in air is very fast in comparison to other fuels. Its upper flammability limit in air is very high and it requires very low ignition energy to ignite compared to other fuels. It has a remarkably higher flame velocity than other fuels. These properties make the hydrogen a unique fuel from both safety and utilization aspects.

**Table 1.1: Properties of hydrogen fuel and other conventional fuels [3]**

<b>Property</b>	<b>Hydrogen</b>	<b>Petroleum</b>	<b>Methanol</b>	<b>Methane</b>	<b>Propane</b>
Normal Boiling point, K	20.3	350-400	337	111.7	230.8
Liquid density, kg/m <sup>3</sup> , NBP*	71	702	797	425	507
Gas density, kg/m <sup>3</sup> , NTP**	0.08	4.68	-	0.66	1.87
Heat of vaporization, kJ/kg	444	302	1168	577	388
Higher heating value, MJ/kg	141.6	46.7	22.7	55.5	50.3
Lower heating value, MJ/kg	120.0	44.38	18.0	50.0	45.6
Lower heating value (liquid), MJ/m <sup>3</sup>	8960	31170	16020	21250	23520
Diffusivity in air, cm <sup>2</sup> s <sup>-1</sup>	0.63	0.08	0.16	0.20	0.10
Lower flammability limit vol. % (in air)	4	1	7	5	2
Upper flammability limit vol. % (in air)	75	6	36	15	10
Ignition temperature in air, °C	585	222	385	534	466
Ignition energy, MJ	0.02	0.25	-	0.30	0.25
Flame velocity, cm/s	270	30	-	34	38

\*Normal boiling point, \*\* Normal temperature (293.15 K) and pressure (101.325 kPa).

### 1.3 Hydrogen storage

Hydrogen storage is a crucial aspect for the development of the hydrogen economy. Solid-state storage is a safe and volumetric efficient method to store hydrogen. Today's most research into hydrogen storage is focused on developing a material that can store hydrogen in a compact way and work in the range of practical applications. There are more challenges for vehicular application than stationary application. For the vehicular application, material should have low cost, high hydrogen capacity, fast kinetics and work at near room temperature under mild pressure condition. The U.S. DOE (department of energy) has set technical targets for onboard hydrogen storage systems (**Table 1.2**). These targets mainly focus on the research and development of material-based technologies in order to compete with conventional fossil fuel based vehicles in the market place. These targets show the importance of both gravimetric and volumetric capacity, as one does not want the store to be heavy (limiting the range of the vehicle) or too voluminous (limiting the luggage space).

**Table 1.2: Technical targets: onboard hydrogen storage systems [4]**

Storage parameter	Units	2020	2025	Ultimate
System gravimetric capacity	kWh/kg	1.5	1.8	2.2
System volumetric capacity	kWh/L	1.0	1.3	1.7
Storage system cost	\$/kWh net	10	9	8
	(\$/kg H <sub>2</sub> )	(333)	(300)	(266)
Fuel cost at pump	\$/gge	4	4	4
System filling time for 5 kg H <sub>2</sub>	min	4.2	3.3	2.5
	(kg H <sub>2</sub> / min)	(1.2)	(1.5)	(2.0)

*Note:* 1 gasoline gallon equivalent (gge) 1 kg hydrogen.

A lot of research work has been carried out for the storage of hydrogen in gaseous, liquid and solid-state forms. These three ways of hydrogen storage are briefly discussed in the following section.

## **1.4 Compressed Hydrogen storage**

High compression ratio is required to store a sufficient amount of hydrogen to run a vehicle for about 500 km. Due to pressure involved, the safety of storage and integrity of the tank is an issue. High strength steel is good from strength perspective, but the weight of the tank is then high. There is also problem of high diffusivity and hydrogen embrittlement. Other options are austenitic steel or composite cylinders. Commercially available tanks are four types (type I, II, III and IV) which can store hydrogen up to pressure of 700 bar [5]. Commercially available type I hydrogen tanks are made of stainless steel with hydrogen pressures varying from 200 to 300 bar [6]. Type I tanks are quite heavy with an energy density of 0.4 kWh/kg. In type II, III and IV tanks, steel is replaced by composite materials and stability is given by carbon fibers or synthetic materials. These hydrogen tanks are lighter and safer than the steel tanks but very expensive.

## **1.5 Liquid Hydrogen storage**

Hydrogen gas was first liquefied by J. Dewar in 1898 [7]. The major issue with liquid state hydrogen storage is boil off losses. Liquefaction process is also highly energy intensive. The energy utilized for cooling from gaseous to liquid hydrogen requires an estimated 30% of LHV of hydrogen, which is very large compared to compression energy required for high pressure tanks. Despite excellent insulation, within a period of time, the liquid hydrogen gains heat from the surroundings and convert into gas. This gas has to be released to avoid excess pressure. These boil off losses are estimated to be around 4% per day for a 4.6 kg tank, but losses are small in bigger volume tank. The cryo-compressed hydrogen storage is a response to these issues and insulated pressure vessels which are heavier than compressed hydrogen storage [8, 9].

## **1.6 Hydrogen storage in solids**

There are two main ways to store hydrogen in a solid: physisorption and chemisorption. Hydrogen molecules are adsorbed on the material surface area in physisorption. In chemisorption, hydrogen forms a chemical compound (e.g. metal hydrides, chemical hydrides and complex hydrides) after reacting with the materials.

### **1.6.1 Physisorption**

The mechanism by which hydrogen molecule adsorbed without dissociating on the surface of solid material is called physisorption. The hydrogen molecule held at the surface of solid due to weak van der Waals forces between the atoms of solid material and hydrogen molecule. Adsorption of hydrogen on the surface of solid is an exothermic process i.e. heat is released during adsorption. This heat value is very low, in the range of 1-10 kJ/mol, due to weak van der Waals force. Porous materials which have received considerable attention include high surface area materials such as carbon nanotubes (CNT), metal organic frameworks (MOF), zeolites and recently investigated polymers of intrinsic porosity (PIMs).

### **1.6.2 Chemisorption**

Hydrogen molecule when coming in contact with a solid surface with the appropriate properties, could dissociate into two hydrogen atoms which diffuse in the solid and form a chemical bond with the solid. This phenomenon is known as chemisorption. Many metals and alloy react reversibly with hydrogen to form hydride. Complex hydrides are also used to store hydrogen chemically.

#### **1.6.2.1 Complex hydrides**

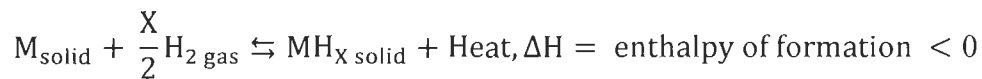
Complex hydrides are salt like materials in which hydrogen is covalently bound to the center atoms, in this way a crystal structure consisting of complex anions is formed. In general, the complex hydrides have the formula  $A_xMe_yH_z$  compounds where A is generally an element of the first and second groups of the periodic table and Me is usually boron or aluminum. Complex hydrides are known as “one pass” hydrogen storage systems which mean that the materials once release hydrogen doesn't take back that hydrogen i.e. are irreversible. Sodium, lithium and beryllium are the only elements lighter than magnesium that can also form solid state compounds with hydrogen. The hydrogen content is as high as 18 wt% for  $LiBH_4$  [5]. Use of complex hydrides for hydrogen storage is challenging because of both kinetic and thermodynamic limitations. Intense research interest has been developed in low weight complex hydrides such as alanates, amides, imides and borohydrides.

### 1.6.2.2 Metal hydrides

Metal hydrides are excellent candidates for hydrogen storage application. The main advantages of storing hydrogen in a metal hydride are the high volumetric densities (sometimes higher than in liquid hydrogen), safe method, optimum operating conditions and the possibility to absorb and desorb hydrogen with a small change of hydrogen pressure [10]. These features are particularly attractive for small portable systems and stationary applications. Metal hydrides can be categorized based on the type of bonding between the host metal and hydrogen. There are elemental, ionic, covalent and metallic hydrides. In metal hydrides, intermetallic compound is also an alternative way to store hydrogen. Intermetallic compounds are generally synthesized by alloying a metal which easily forms stable hydrides (A) and another element which does not form stable hydrides (B). There are different types of intermetallic compounds based on their stoichiometry such as  $AB_5$ ,  $AB_2$ ,  $A_2B$  and  $AB$ . Solid solution alloys with body-centered cubic (BCC) structure are also another type of intermetallic compound. A brief literature survey on these types of intermetallic compounds is given in the following sections after discussing the thermodynamics and hydriding process of metal hydrides.

## 1.7 Thermodynamics of Metal Hydrides

Metal hydrides are generally formed by simply exposing the metal to hydrogen gas. A reversible reaction of hydrogen with metal, forming metal hydride can be written as



Where M is the metal element or alloy,  $MH_X$  is the metal hydride and  $\Delta H$  is the enthalpy of formation of the metal hydride. Here, forward reaction is exothermic ( $\Delta H < 0$ ), that means heat is released, whereas the reverse reaction is endothermic ( $\Delta H > 0$ ), there is a need to add heat to release the hydrogen. The reaction of the metal or alloy with hydrogen gas is illustrated in **Figure 1.1** by pressure -composition - temperature curve (PCT curve).

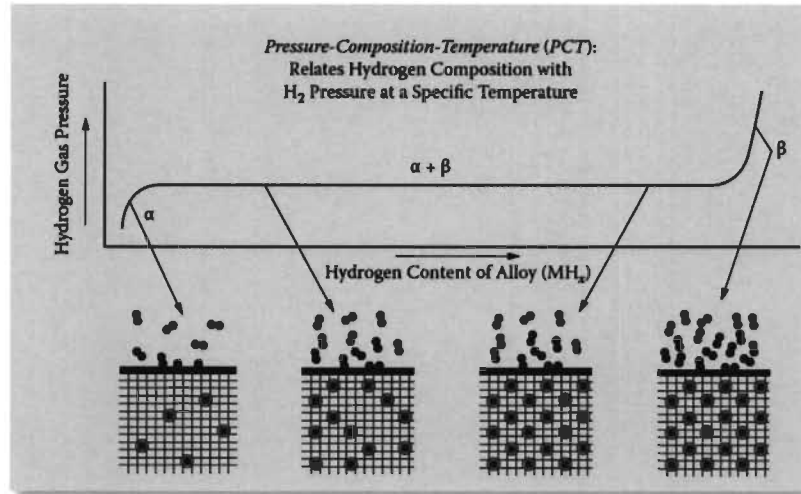


Figure 1.1: P-C-T curve for metal hydrides [7]

When at a given temperature, hydrogen gas is introduced into a vessel containing metal or alloy, firstly, hydrogen molecule dissociates into hydrogen atom on the material surface. Then hydrogen atom dissolves in crystal lattice of the metal or alloy to form a solid solution (designated as the  $\alpha$ -phase). Further increase in pressure of hydrogen, leads to more dissolved hydrogen.

When saturation limit of the solid solution phase is reached, the metal hydride begins to form as a distinct second solid phase (designated as  $\beta$ -phase). Pressure of the hydrogen remains constant and hydrogen to metal ratio increases with progressive conversion of  $\alpha$ -phase into  $\beta$ -phase. This pressure is known as plateau pressure. The plateau continues, as long as there are two distinct phases, as required by Gibbs' phase rule:

$$F = C - P + 2$$

But temperature is fixed, so

$$F = C - P + 1$$

Where  $F$  is the degree of freedom,  $P$  is the number of phases and  $C$  is the number of components. In plateau pressure region,  $C = 2$  (Hydrogen gas and metal),  $P = 2$  ( $\alpha$ -phase and  $\beta$ -phase), so

$$F = 1$$

The plateau region is the most important segment of the PCT curve. The value of plateau pressure represents the pressure of hydrogen in equilibrium with the metal-metal hydride ( $\alpha + \beta$ ) phases, or, also known as dissociation pressure of the metal hydride at a certain temperature. Its value indicates the thermal stability of the metal hydride and can be used as an index of the relative thermal stabilities of different metal hydrides at a given temperature.



### 1.7.1 Effect of temperature increase

The effect of temperature on PCT curve is shown in **Figure 1.2 (a)**. In particular, increase of the isotherm temperature causes the plateau pressure to increase and at the same time, reduces the width of the plateau which represents the miscibility regime of the  $\alpha$ -phase and  $\beta$ -phase. At a certain critical temperature ( $T_c$ ), the width of the plateau pressure completely reduces where the miscibility of the two phases is zero and  $\alpha$ -phase converts continuously into the  $\beta$ -phase.

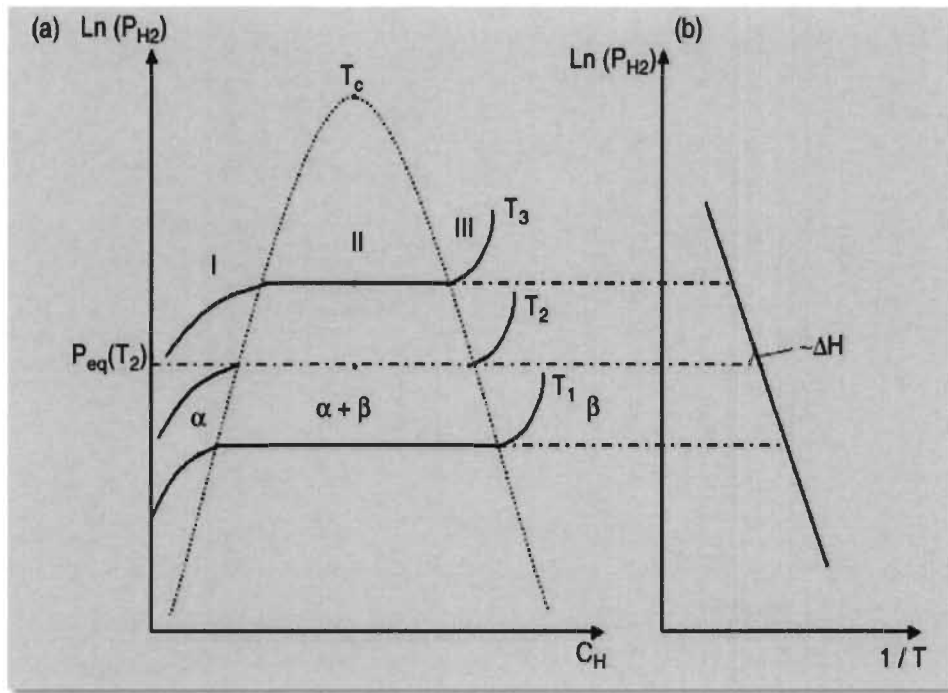


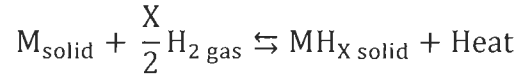
**Figure 1.2: (a) The effect of temperature on PCT curve (b) van't Hoff plot of equilibrium pressure with respect to  $1/T$  [5]**

The thermodynamics for the formation of a metal hydride can be derived from the van't Hoff relation between the equilibrium pressure ( $P_{H_2}$ ) and the absolute temperature ( $T$ ), at constant hydrogen concentration in metal. This relation is given as

$$\frac{d \ln K}{dT} = \frac{\Delta H}{RT^2}$$

Where  $R$  is the gas constant,  $T$  is the temperature,  $\Delta H$  is the heat of reaction or enthalpy and  $K$  is the equilibrium constant.  $K$  can be written in the term of activities of the products and reactants.

The reaction of the metal hydride is written as



So, K for this reaction is given by

$$K = \frac{a_{MH_X}}{a_M \times a_{H_2}}$$

The activities of the metal and metal hydride ( $a_M$  and  $a_{MH_X}$ ) might be taken as equal to unity, since these refer essentially to pure solid phases, and  $a_{H_2}$  may be substituted by  $P_{H_2}$  in atm. Hence above equation for K reduces to

$$K = P_{H_2}^{-X/2}$$

By putting this value in this equation,

$$\frac{d \ln K}{dT} = \frac{\Delta H}{RT^2}$$

$$d \ln \left( P_{H_2}^{-\frac{X}{2}} \right) = \left( \frac{\Delta H}{RT^2} \right) dT$$

$$\ln P_{H_2} = \frac{2\Delta H}{XRT} + C$$

Where C is the constant of integration. If the hydride is stoichiometric and the solubility of hydrogen is small in the  $\alpha$ -phase, then enthalpy of formation can be determined from the slope of a plot of  $\ln P_{H_2}$  with respect to  $1/T$  as shown in **Figure 1.2 (b)**. Where  $P_{H_2}$  represents the plateau pressure at a certain temperature T. The practical significance of  $\Delta H$  is that it indicates the thermal stability of a metal hydride. If  $\Delta H$  value is high, then metal hydride is more stable and dissociation

pressure is lowered. Therefore, high temperature is needed to decompose the metal hydride and liberate the hydrogen.

Since, standard Gibbs free energy can be written as

$$\Delta G^{\circ} = -RT \ln P_{H_2}$$

Since,  $\Delta G^{\circ} = H^{\circ} - TS^{\circ}$ , so, we find an equation from where, value of entropy directly calculated by the intercept of van't Hoff plot.

$$\ln P_{H_2} = \frac{\Delta H^{\circ}}{RT} - \frac{\Delta S^{\circ}}{R}$$

In general, entropy change of the metal hydride formation is mainly given by the loss of standard entropy of the hydrogen gas when it enters the metal lattice. It means the entropy does not depend significantly on the nature of the metal. So, entropy value is usually considered to be constant.

## 1.8 Hydriding process

The hydrogenation process is generally made of five steps: migration of hydrogen molecules (step 1), physical adsorption (step 2), dissociation of hydrogen molecule (step 3), chemisorption (step 4), and hydride formation (step 5). These steps are shown in **Figure 1.3**. The dehydrogenation process is just the reverse of hydriding process. The slowest step among these steps gives us idea about the kinetics behaviour of alloys. There are different kinetic models that have been developed for the determination of rate limiting step. A detailed discussion on these kinetic models is given in chapter 4.

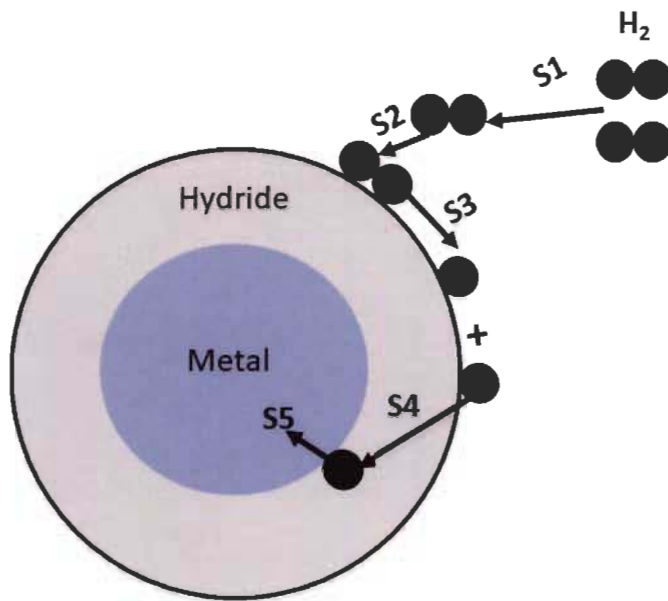
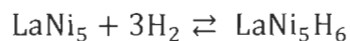


Figure 1.3: Different steps in the hydrogenation process

### 1.9 AB<sub>5</sub>-type alloys

AB<sub>5</sub>-type alloys are mainly combination of rare earth metals and d-block metals. Generally, AB<sub>5</sub> compounds form hydrides at equilibrium pressure of a few atmospheres and at temperature up to 100 °C [11]. These alloys have good hydrogen storage capacity (~1.5 wt%), low hysteresis, resistance to the gaseous impurities and easy activation in the initial cycle. These alloys have a hexagonal structure with CaCu<sub>5</sub> type lattice. The most studied alloy in this group is LaNi<sub>5</sub>, which reacts with hydrogen as follows:



However, nickel and lanthanum are the main metals in LaNi<sub>5</sub> which makes it costly. Upon hydrogenation, the crystal structure remains hexagonal but with a lattice expansion of about 25%. Here, La has strong affinity for hydrogen and Ni does not absorb hydrogen or absorb little. However, the major issues with LaNi<sub>5</sub> alloy are high cost of raw material and low theoretical hydrogen capacity (1.5 wt%). Several research work on tackling these two major issues of LaNi<sub>5</sub> alloy has been reported in literature [12-16]. Partial substitution of Ni changes the thermodynamic properties and also reduces the degradation during pressure cycling [11]. Effect of partial

substitution of Ni with Al, Cr, Cu, Sn, Fe, Mn, Co, Ga, Zn or other metals has been investigated by Sharma et al. and they found that partial substitution of Ni with Al, Co and Mn provides a wide range of thermodynamic properties [14]. Sharma et al. also found that partial substitution of Ni with Al improves cycling stability and also reduces the plateau pressures significantly. Partial substitution of La with Ce in  $\text{LaNi}_5$  was also investigated in order to improve its hydrogen storage capacity and plateau pressures for high pressure applications [16]. However,  $\text{CeNi}_5$  requires several activation cycles under high hydrogen pressure before first absorption in order to absorb hydrogen [17]. Jain et al. [18] studied the effect of partial substitution of Ni with Cr in  $\text{CeNi}_5$  on the hydrogen storage properties of  $\text{CeNi}_5$  alloy and results reveals that maximum hydrogen storage capacity of substituted alloys was higher than parent alloy ( $\text{CeNi}_5$ ) with a value of 3.5 and 3.8 for  $\text{CeNi}_4\text{Cr}$ ,  $\text{CeNi}_3\text{Cr}_2$ , respectively. Partial substitution of Ce with La in  $\text{CeNi}_3\text{Cr}_2$  was also investigated by Jain et al. [19] as a continuation of previous study [18] and they found that increase in La content improves the maximum hydrogen storage capacity while decreases the plateau pressure. Partial substitution of Ni with Zr in  $\text{CeNi}_5$  was also performed by Jain et al. [20] and results clearly indicates that maximum hydrogen capacity was around 4 and 4.3 for the  $\text{CeNi}_4\text{Zr}$  and  $\text{CeNi}_3\text{Zr}_2$  alloy, respectively at operating temperature (293–333 K) under 3.2 MPa pressure conditions.

### **1.10 AB<sub>2</sub>-type (Lave phase) alloys**

In AB<sub>2</sub>-type alloys, A can be one or more of titanium, zirconium, hafnium and rare earth elements and B can be one or more of vanadium, chromium, manganese and iron. It consists of three structure type which are cubic  $\text{MgCu}_2$  (C15), hexagonal  $\text{MgZn}_2$  (C14) and hexagonal  $\text{MgNi}_2$  (C36). This family of structure types is known as Laves phase. Laves phase makes a large group of alloys, therefore, it has wide range of properties. In AB<sub>2</sub> alloys, mostly, Zr based alloys has been studied previously due to their good hydrogen storage capacity (~2 wt%) and kinetics, long cycling life and low cost [21]. However, these alloys are more sensitive to the gaseous impurities and their hydrides are too stable at room temperature. Multicomponent systems  $\text{Zr}_{1-x}\text{T}_x(\text{Mn, Cr})_{2-y}\text{M}_y$  where  $\text{T} = \text{Ti, Y, Hf, Sc, Nb}$  and  $\text{M} = \text{V, Mo, Mn, Cr, Fe, Co, Ni, Cu, Al, Si, Ge}$  is an effective way to optimize the hydrogenation properties of AB<sub>2</sub>-type alloys [17, 22-25]. A systematic investigation on the hydrogen storage properties of vanadium (V)-containing or V-free AB<sub>2</sub>-type alloys has been shown by Young et al. [24]. They observed that hydrogen storage capacity of V-free ( $\text{Ti}_{10}\text{Zr}_{27}\text{Ni}_{35}\text{Co}_5\text{Mn}_{15}\text{Cr}_8\text{Al}_{0.1}$ ) alloy was larger in gaseous phase compared to the V-based alloy

( $\text{Ti}_{12}\text{Zr}_{21.5}\text{V}_{10}\text{Ni}_{37.7}\text{Mn}_{13.5}\text{Cr}_{4.5}\text{Al}_{0.5}\text{Sn}_{0.3}$ ). Partial substitution with other transition metals in  $\text{ZrFe}_{1.8}\text{M}_{0.2}$  alloy where  $\text{M} = \text{V}, \text{Cr}, \text{Mn}, \text{Fe}, \text{Co}, \text{Ni}, \text{Cu}, \text{Mo}$  was studied by Mitrokhin et al. [17] in order to improve the hydrogenation properties and they found the larger hydrogen storage capacity  $\sim 1.8$  wt% for V, Cr and Mn substitution than other substituted alloys. Young et al. also investigated the effect of cobalt (Co) with yttrium (Y) on the hydrogen storage performance of  $\text{Zr}_{21.5}\text{V}_{10}\text{Cr}_{7.5}\text{Mn}_{8.1}\text{Co}_{8.0}\text{Ni}_{32.2}\text{Sn}_{0.3}\text{Al}_{0.4}$  alloys [25] and they found that maximum reversible hydrogen storage capacity (1.36 wt%) could be obtained at 333 K for the 2 at % Y. These previous studies on  $\text{AB}_2$  alloys suggest improvement in the hydrogen storage capacity and that the alloys are more attractive for stationary applications.

### 1.11 Solid solution alloys

Ti-based Laves phase alloys of  $\text{AB}_2$ -type contains the body-centered cubic (BCC) and Laves phases, where both phases contribute to the hydrogenation. These phases show the same equilibrium pressure. Due to this reason, this new class of alloys has been called Laves phase related solid solution alloys. In solid solution alloys, vanadium-based solid solution alloys with body-centered cubic (BCC) structures have been extensively studied because of their good hydrogen storage capacity ( $\sim 4$  wt%), low hydrogen absorption/desorption temperature and fast first hydrogenation kinetics. However, these alloys are still considered to be not satisfactory for vehicular application due to the involvement of activation step before first hydrogenation. Several methods have been applied earlier to the BCC solid solution alloys in order to improve the first hydrogenation kinetics such as annealing [26], surface modification [27], element substitution [28]. Young et al. studied the effect of annealing on Laves phase related BCC (body-centered-cubic) solid solution metal hydride alloys [26]. They found that annealing at  $800^\circ\text{C}$  and  $900^\circ\text{C}$  promotes the formation of the main hydrogen storage BCC phase abundance and reduced C14 and TiNi catalytic phases. Ti-based solid solution alloys with BCC structure such as Ti–V–Cr, Ti–V–Mn and Ti–Cr–Mo were also studied previously because it has good hydrogen capacity  $\sim 2$  wt% and fast absorption kinetics [29, 30]. These Ti-based alloys such as  $\text{Ti}_{0.5}\text{V}_{0.5}\text{Mn}$  has fast first absorption/desorption kinetics and high reversible hydrogen capacity  $\sim 1.9$  wt% at 260 K temperature under 35 MPa [31]. All these previous investigations on BCC solid solution make possible hydrogen absorption at reasonable temperature and pressure and suggest that these can be potential hydrogen storage material.

### 1.12 A<sub>2</sub>B-type alloys

In A<sub>2</sub>B-type alloys, A mostly represents alkali earth metals or transition metals and B represents the transition metals. Among A<sub>2</sub>B-type alloys, Ti<sub>2</sub>Ni and Mg<sub>2</sub>Ni are the most studied alloys because of its desirable structural and hydrogen storage properties [32, 33]. It was found that Mg<sub>2</sub>Ni can absorb ~ 3.6 wt% at a temperature of 250 °C [33]. Partial substitution of magnesium (Mg) with neodymium (Nd) in Mg<sub>2</sub>Ni alloy was also performed by Xie et al. [34]. They prepared Mg<sub>2-x</sub>Nd<sub>x</sub>Ni ( $x = 0, 0.1, 0.2, 0.3$ ) using induction melting under helium atmosphere. The best alloy's composition was found to be Mg<sub>1.9</sub>Nd<sub>0.1</sub>Ni and it absorbed 3.50 wt% at 350 °C temperature. Effect of Partial substitution of Zr on the hydrogenation behaviour of Ti<sub>2</sub>Ni alloy was investigated by Zhao et al. [32]. Substitution of Zr resulted an increase in hydrogen desorption capacity and the cyclic stability.

### 1.13 AB-type alloys

AB-type alloys have good volumetric and gravimetric reversible hydrogen storage capacities compared to AB<sub>5</sub> and AB<sub>2</sub> alloys. In this group of alloys, most studied alloy is TiFe because it can absorb hydrogen ~ 1.9 wt% at room temperature under mild pressure condition [35]. It crystallizes in CsCl-type structure. However, one issue with TiFe alloy is that activation step is needed such as element substitution, annealing or mechanical activation before first hydrogenation in order to break the oxide layer at the surface. A detailed review on the process of improvement in the first hydrogenation of TiFe alloy has been discussed in chapter 2.

The hydrogen absorption/desorption properties of different intermetallic compounds have been shown in **Table 1.3**. These intermetallics hydrides have high hydrogen storage capacity at moderate temperature and pressure conditions.

**Table 1.3: Hydrogen absorption/desorption properties of various intermetallic hydrides [36]**

<b>Intermetallic compound</b>	<b>Temperature (K)</b>	<b>Pressure (MPa)</b>	<b>Hydrogen storage capacity (wt%)</b>
CeNi <sub>4</sub> Zr	T <sub>des</sub> : 293–333	3.200	4.00
CeNi <sub>4</sub> Cr	T <sub>des</sub> : 293–333	3.100	4.30
CeNi <sub>3</sub> Cr <sub>2</sub>	T <sub>des</sub> : 293–333	3.250	3.80
LaNi <sub>4.5</sub> Sn <sub>0.5</sub>	T <sub>abs</sub> : 298	0.750	0.95
Zr <sub>0.9</sub> Ti <sub>0.1</sub> Cr <sub>0.8</sub> V <sub>0.8</sub> Ni <sub>0.4</sub>	T <sub>des</sub> : 373	0.100	2.00
Zr <sub>21.5</sub> V <sub>10</sub> Cr <sub>7.5</sub> Mn <sub>8.1</sub> Co <sub>6.0</sub> Y <sub>2.0</sub> Ni <sub>32.2</sub> Sn <sub>0.3</sub> Al <sub>0.4</sub>	T <sub>abs</sub> : 333 T <sub>des</sub> : 333	0.056	1.36
Ti <sub>0.5</sub> V <sub>0.5</sub> Mn	T <sub>des</sub> : 260	35.000	1.90
Ti <sub>0.47</sub> V <sub>0.46</sub> Mn	T <sub>des</sub> : 303	12.000	1.53

### 1.14 Motivation

Two of the major characteristics of metal hydrides should have in order to fulfill the requirements for mobile and stationary applications are low cost and utilization in a practical range of temperature and pressure (0-100°C, 1-10 atm) [37-39]. TiFe alloy is a promising candidate to meet these requirements. TiFe alloy has low cost of raw material, good hydrogen capacity (maximum hydrogen capacity ~1.9 wt% at room temperature) and works at room temperature under mild pressure [35, 40]. One major problem with this alloy is that the first hydrogenation, the so-called activation, is difficult. The alloy must be exposed to high temperature and high hydrogen pressure in order to absorb hydrogen. This makes the production of this metal hydride more complicated and costly.

Addition or partial substitution of transition metals or rare-earth metals to TiFe alloy is an effective method to improve this activation step. Recently, Jain et al. found that addition of small amount



of Zr to TiFe made the activation possible at room temperature [41, 42]. First hydrogenation of TiFe alloy can also be improved by partial substitution of Fe and/or Ti with transition metals such as Cr, Mn, Ni [43, 44], V [45]. A faster and easier activation means a cost reduction and thus more attractive for practical applications. However, one issue is the production of this alloy at industrial scale. Therefore, TiFe alloy with Zr, Mn and V were synthesized by using industrial grade Fe and Ti and hydrogen storage properties of these alloys have been studied.

Another way towards easy activation is by producing an ultra-fine microstructure. There are different methods such as ball milling [46, 47], cold rolling [48], high-pressure torsion [48, 49] to alter the microstructure of alloys. Annealing of the alloy is also an effective method to alter the crystallinity, chemical composition, phase abundance and catalytic properties of alloys. In the case of metal hydrides, the flatness of the plateau region in PCT curve (Pressure-composition isotherm) of hydrogen storage alloys is important for practical applications. Usually, annealing has the effect of flattening the plateau region [50, 51]. Therefore, annealing is widely used during alloy synthesis. Abe and Kuji observed that plateau pressure decreases ( $\sim 1$  MPa) for TiFe prepared by the combination of ball milling and post-annealing [52]. All these investigations show that annealing reduces the hysteresis in PCT curve and also improve activation of alloys. All these results motivated us to investigate the effect of heat treatment on hydrogen storage properties and microstructure of TiFe alloys with Zr as additive.

The cooling rate is another important parameter during synthesis of alloys for determining the microstructure of the alloys [53, 54]. Higher cooling rate leads to less solidification time and reduces the grain size of the cast alloy and thus increasing grain density [55]. Chen et al. studied the effect of cooling rate on the microstructure and mechanical properties of TiFe alloy [56]. They found that lamellar structures become finer as the cooling rate increase. To our knowledge, there are no previous investigations in which effect of cooling rate on the hydrogenation behavior of TiFe alloy has been reported.

From previous investigations, it is known that addition of 4 wt% Zr enhances the activation (first hydrogenation) kinetics of TiFe alloy [41, 42, 57, 58]. It was also found that the microstructure plays an important role via the beneficial effects of the zirconium-rich secondary phase in this alloy. For industrial scale synthesis, it is important to know the effect of cooling rate on the

microstructure and thereby on the hydrogen storage properties. In this investigation, we studied the effect of cooling rate on hydrogen storage properties of TiFe with 4 wt% Zr as an additive.

### **1.15 Objectives**

The objective of this work is to study the effect of heat treatment and cooling rate on the microstructure and hydrogen storage properties of TiFe alloys with additives. The ultimate objective will be to optimize the chemical composition of the alloy and synthesis parameters of industrial methods, in order to have a TiFe alloy that will absorb hydrogen quickly and reversibly at low temperature. In order to work with industrial-scale facilities, this project was done in collaboration with the 'Quebec Metallurgy Center' CMQ.

### **1.16 Thesis structure**

Introduction, background studies, and objectives of the work are mentioned in chapter 1. Literature review on the different methods for improvement in the activation kinetics behaviour of TiFe alloys has been reviewed in chapter 2. Experimental details are described in chapter 3. Study on the microstructure and hydrogen storage properties of TiFe with Zr, Mn, and V (as a single additive or as a combination of two or three additives) are reported in chapter 4. Effect of heat treatment on TiFe with Zr additive is explained in chapter 5. Effect of cooling rate on the microstructure and hydrogenation behaviour of TiFe with Zr is described in chapter 6. Chapter 7 mainly focused on the study of microstructure and hydrogen storage properties of  $Ti_xFe_{2-x} + 4 \text{ wt\% Zr}$ , where,  $x = 1.1, 1.05, 0.99, 0.94$ . Conclusion and future scope are included in chapter 8.

## Chapter 2

### Literature review on TiFe

---

#### 2.1 Introduction

TiFe alloy is an alloy of AB group which is low cost and absorb hydrogen at a low equilibrium pressure at room temperature. TiFe as a hydride was first recognized by J.J. Reilly and Wiswall [35]. There are two stable intermetallics formed by Ti-Fe alloy, TiFe and TiFe<sub>2</sub>. TiFe<sub>2</sub> does not absorb hydrogen appreciably. TiFe crystallizes in the form of CsCl type structure. When hydrogen is exposed to the TiFe then there are two hydrides formed FeTiH and FeTiH<sub>2</sub>. The solid solution takes up hydrogen to a composition of FeTiH<sub>0.10</sub> ( $\alpha$ -phase). After solubility limit, these following two reactions occur:

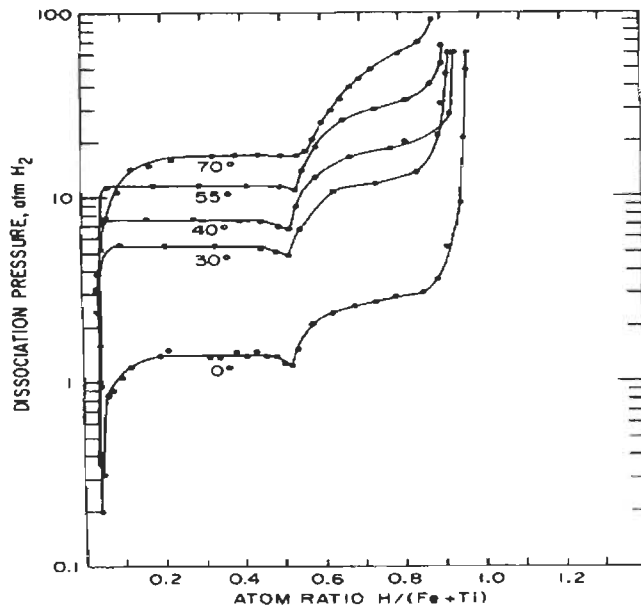
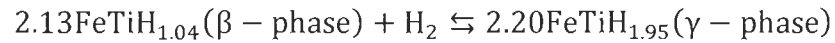
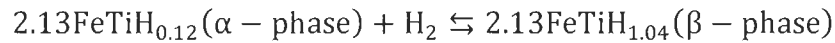


Figure 2.1: P-C-T plot for FeTi-H system [35]

The P-C isotherms for FeTi-H system are shown in **Figure 2.1**. These P-C isotherms were obtained at a set of temperatures from 0 °C to 70 °C. The isotherms exhibit two plateaus. First plateau is for monohydride ( $\beta$ -phase) and second is for dihydride ( $\gamma$ -phase). The enthalpy values by van't Hoff plots were obtained -28.14 kJ/mol of hydrogen and -30.66 kJ/mole of hydrogen for monohydride and dihydride, respectively. It is necessary to initially activate TiFe before it could react to hydrogen at a practical rate [59]. The reason is the presence of an oxide layer of  $\text{TiO}_2$  that is formed due to air exposure. The presence of  $\text{TiO}_2$  layer on TiFe alloy hinders the dissociation of hydrogen molecules, thereby decreasing the absorption rate. In TiFe alloy, its oxide layer can be broken by heating the sample at a very high temperature for several days. The process of heating alloy at high temperature and pressure is known as activation step. Activation step can be improved by addition of elements to alloy or substitution of one of the two elements with other elements. Mechanical alloying, severe plastic deformation such as high-pressure torsion, plastic deformation using groove or cold rolling and annealing are also other ways to ease the activation step. A detailed literature survey on these methods of improving hydrogenation properties of TiFe alloy is presented in the following sections.

## **2.2 Effect of substitution and additives on TiFe alloy**

Addition or substitution of elements in TiFe alloy leads to ease in the activation step and also improve the first hydrogenation kinetics. Substitution of Fe with Be and Al in TiFe was done by Bruzzone et al. [60]. Beryllium and aluminum were selected because of their low atomic weight, in view of practical applications. Substitution of Fe with Be [60] and Al [61] in TiFe alloy leads to low hysteresis compared to reported TiFe alloy's PCT [35]. However, Beryllium is extremely hazardous for health. The requirement of annealing of alloys at 1000 °C for 4 days before hydrogenation has been also reported. Further, substitution of Fe with Al in TiFe up to 1-5 at. % has been carried out by Lim et al. [62] and it was found that higher aluminum content results in low hysteresis but the maximum hydrogen capacity decreases. Partial substitution of Ti with Zr in TiFe was also studied in order to improve activation step [63-65]. Jang et al. [63], Nagai et al. [64] and Nishimiya et al. [65] investigated the composition  $\text{Ti}_{1-a}\text{FeZr}_a$  (where  $a = 0.01, 0.1$  and  $0.2, 0.02$  [63],  $0.1, 0.2$  and  $0.3$  [64] and  $0.1, 0.2$  and  $0.5$  [65]). They found that partial substitution of Zr improves the first hydrogenation kinetics and lowers the equilibrium pressure. Addition of Ni to TiFe alloy was also found to effective in terms of improving kinetics and maximum hydrogen capacity without any activation process [66]. Jain et al. showed the effect of individual elements

Zr, Ni and simultaneous addition of these two elements ( $Zr_7Ni_{10}$ ) to understand the effect on hydrogenation properties of TiFe alloy [41]. First hydrogenation curves were obtained at 40 °C under 2 MPa  $H_2$  pressure as shown in **Figure 2.2**. TiFe with Zr was reported to absorb more hydrogen (~ 1.6wt %) at a higher rate than Ni,  $Zr_7Ni_{10}$  and the supply pressure of hydrogen can also be reduced to 2 MPa.

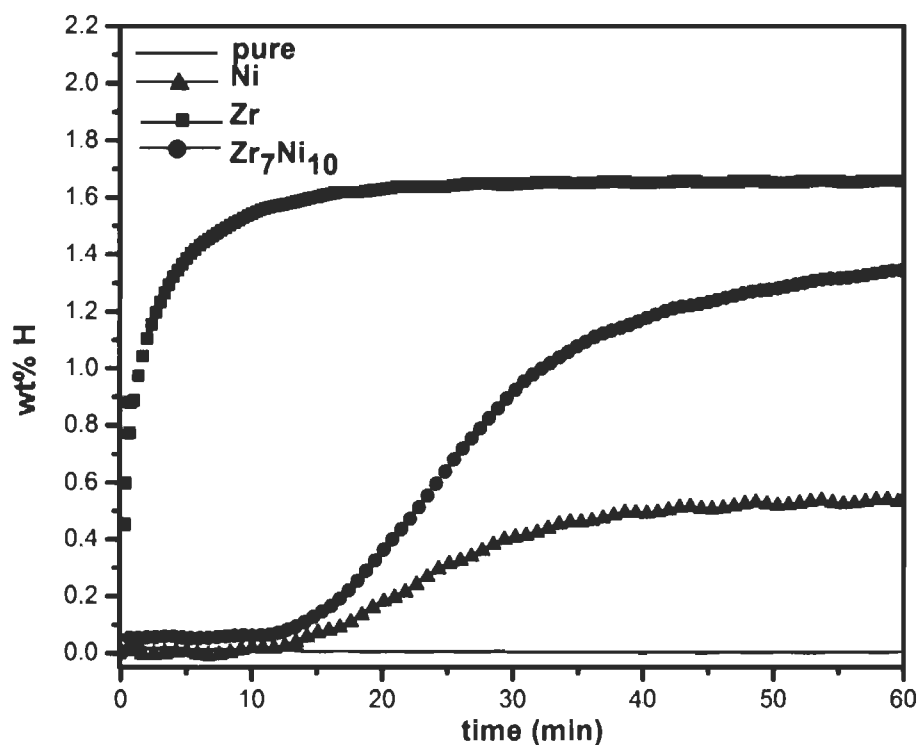


**Figure 2.2: First hydrogenation curve of pure TiFe alloy and with 4 wt% additives under 2 MPa  $H_2$  at 40 °C [41]**

The desorption curves obtained under 0.1 MPa of hydrogen for TiFe alloys with additives are shown in **Figure 2.3**. Alloys with the addition of Zr only and  $Zr_7Ni_{10}$  as additives desorbed hydrogen around 1.2 wt% with faster kinetics than Ni. The value of desorbed hydrogen is same for Zr and  $Zr_7Ni_{10}$ . This indicates that addition of only Zr is sufficient for activation improvement.

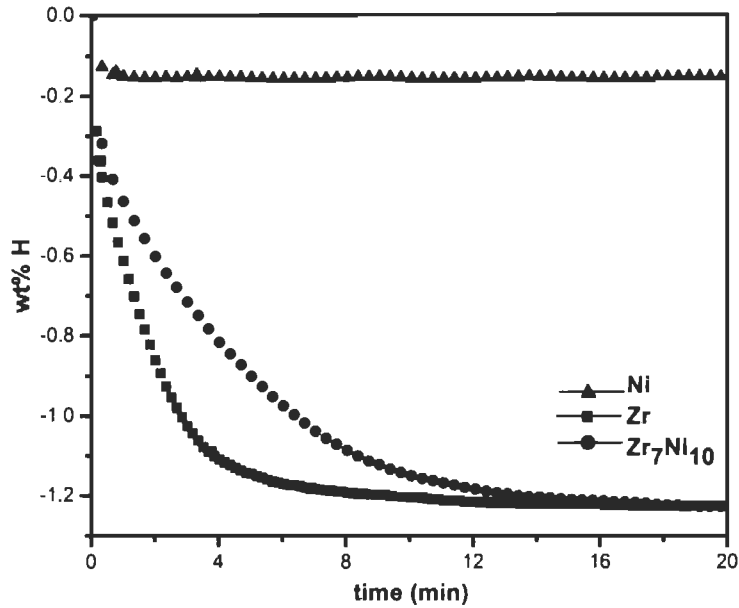


Figure 2.3: Desorption Curve of TiFe with 4 wt% additives under 0.1 MPa H<sub>2</sub> at 40 °C [41]

After first hydrogenation cycle, P-C isotherms for the alloys having Zr, Ni and Zr<sub>7</sub>Ni<sub>10</sub> were measured at 40 °C and reported which are as shown in Figure 2.4. From PCI desorption curves, it was concluded that additives lower the plateau pressure of TiFe alloy. For Zr and Zr<sub>7</sub>Ni<sub>10</sub>, plateau pressure was respectively 0.3 MPa and 0.12 MPa.

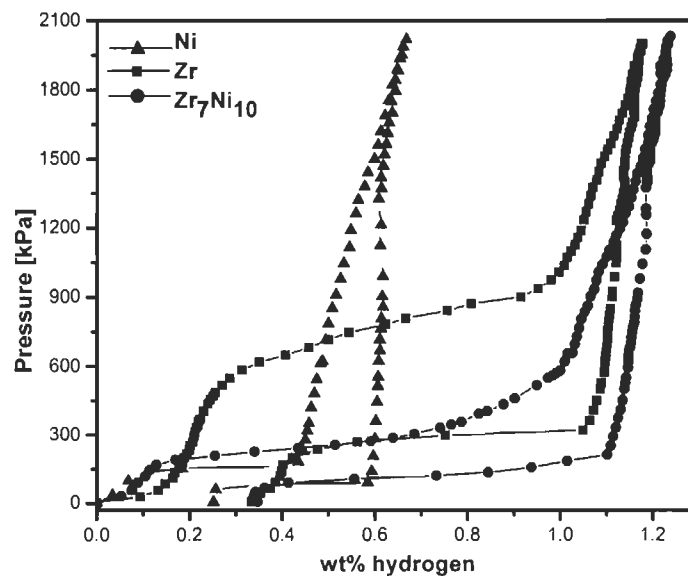
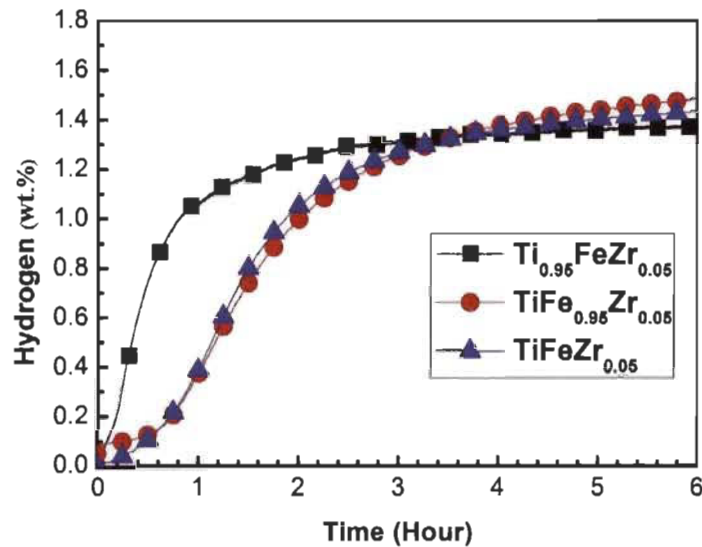


Figure 2.4: PCT curve of TiFe with different additives [41]

The reduced plateau pressure obtained by using  $Zr_7Ni_{10}$  alloy is mainly due to nickel, as the plateau pressure of TiFe alloy with 4 wt% Ni was also found to have the same value. No change in the width of the plateau pressure was found with changing the additive material from  $Zr_7Ni_{10}$  to Zr. However, the isotherm exhibits large hysteresis with Zr additive in comparison to  $Zr_7Ni_{10}$  additive. Recently, a comparative study on the addition of Zr and substitution of Ti or Fe with Zr has been shown by Peng et al. [67]. A clear difference in the first hydrogenation kinetics of  $Ti_{0.95}FeZr_{0.05}$ ,  $TiFe_{0.95}Zr_{0.05}$  and  $TiFeZr_{0.05}$  could be seen in **Figure 2.5**. A faster first hydrogenation kinetics for  $Ti_{0.95}FeZr_{0.05}$  than for the other two alloys was seen. The cause for this discrepancy was reported to be the finer distribution of secondary phase in the microstructure of  $Ti_{0.95}FeZr_{0.05}$  alloy.



**Figure 2.5: The activation behaviour of  $Ti_{0.95}FeZr_{0.05}$ ,  $TiFe_{0.95}Zr_{0.05}$  and  $TiFeZr_{0.05}$  alloys at room temperature under 2 MPa hydrogen pressure [67]**

Effect of addition of Zr at higher concentration level; TiFe + X wt% Zr with X = 4, 8, 12, and 16 on the first hydrogenation kinetics was studied by Gosselin et al. [57]. It was found that increasing the Zr content from 4 to 16 wt% greatly increases the kinetics and also maximum hydrogen capacity.

Addition or substitution of Mn is also an effective way to improve the first hydrogenation kinetics of TiFe alloy [43, 44, 68]. Partial substitution of Fe and/or Ti in TiFe with transition metals such as Cr, Mn and Ni [43, 44] resulted in improving the reaction kinetics and also avoiding the activation step. However, in these works, samples were either annealed at 900 °C [44] or at 400 °C [43] prior to hydrogenation. Lanyin et al. studied the hydriding characteristics of composition;  $Ti_{1+x}Fe_{1-y}Mn_yMm_z$  (X = 0.01–0.09, Y = 0.1–0.2, Z = 0.002–0.028) and it was found that

combination of misch metal (Mm; mainly Ce and La) and Mn leads the easy activation at room temperature without any annealing and reaches 2.05-2.15 wt% hydrogen capacity [68]. Recently, substitution or addition of other elements to Mn substituted TiFe alloys has been carried out [69-71]. Leng et al. found that introduction of small amount of Ce to  $\text{TiFe}_{0.9}\text{Mn}_{0.1}$  alloys remarkably improved activation properties as could be seen in **Figure 2.6** [70]. Hydrogen absorption was possible at 353 K under an initial hydrogen pressure of 4.0 MPa but only  $\sim 1$  wt% maximum hydrogen storage capacity was achieved.

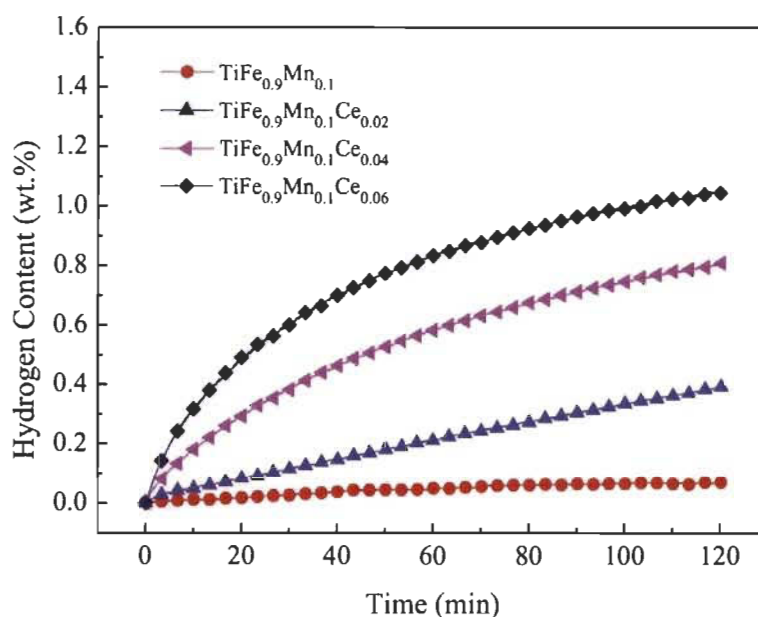


**Figure 2.6: Initial hydriding curves of  $\text{TiFe}_{0.9}\text{Mn}_{0.1}\text{Ce}_x$  ( $x = 0, 0.02, 0.04, 0.06$ ) at 353 K and under initial pressure of 4.0 MPa [70]**

In several other literature studies, the effect of simultaneously adding over-stoichiometrical Ti and addition or partial substitution of elements on hydrogen storage properties of TiFe alloy has been reported [68, 72-76]. Guéguen et al. showed the effect of addition of vanadium on the microstructure and hydrogen storage properties of  $\text{TiFe}_{0.9}\text{V}_x$  and  $\text{TiFe}_{0.8}\text{Mn}_{0.1}\text{V}_x$  where  $x = 0, 0.05$  and  $0.1$  [45]. Addition of vanadium results in a decrease of plateau pressure and also in flattening the plateau region of  $\text{TiFe}_{0.8}\text{Mn}_{0.1}$ . Hydrogenation properties of different substituted TiFe alloys, TiFe alloy with addition of elements or TiFe alloys with excess of Ti are summarized in **Table 2.1**.



**Table 2.1: The hydrogenation properties of various substituted TiFe alloys**

<b>Alloy composition</b>	<b>Maximum hydrogen capacity (wt%)</b>	<b>Desorption plateau pressure, P (atm)</b>	<b>Temperature (°C)</b>	<b>References</b>
TiFe (MP)	1.9	~ 5	30	[35]
TiFe + 4 wt% Zr	~ 1.15	2.96	40	[41]
Ti <sub>0.95</sub> FeZr <sub>0.05</sub>	~ 1.25	~ 2.66	25	[67]
TiFe <sub>0.95</sub> Zr <sub>0.05</sub>	~ 1.43	~ 1 (sloping plateau)	25	[67]
TiFeZr <sub>0.05</sub>	1.3	~ 2.66	25	[67]
TiFe <sub>0.86</sub> Mn <sub>0.1</sub> (MP)	1.9	~ 5.9 (sloping plateau)	45	[69]
TiFe <sub>0.86</sub> Mn <sub>0.04</sub> Co <sub>0.06</sub>	1.85	~ 4.8	45	[69]
TiFe <sub>0.85</sub> Mn <sub>0.15</sub> (MP)	~ 1.28	~ 1 (sloping plateau)	20	[71]
TiFe <sub>0.9</sub> Mn <sub>0.1</sub>	1.72	~ 6.9	40	[70]
TiFe <sub>0.9</sub> Mn <sub>0.1</sub> Ce <sub>0.04</sub>	1.72	~ 6.9	40	[70]
Ti <sub>1.1</sub> Fe <sub>0.8</sub> Mn <sub>0.2</sub> (MP)	1.8	1.8 (sloping plateau)	40	[75, 76]
Ti <sub>1.09</sub> Pr <sub>0.01</sub> Fe <sub>0.8</sub> Mn <sub>0.2</sub>	~ 1.8	2.3 (sloping plateau)	40	[75]
Ti <sub>1.09</sub> Sm <sub>0.01</sub> Fe <sub>0.8</sub> Mn <sub>0.2</sub>	1.8	2.5 (sloping plateau)	40	[75]

**Table 2.1 (continue)**

<b>Alloy composition</b>	<b>Maximum hydrogen capacity (wt%)</b>	<b>Desorption plateau pressure, P (atm)</b>	<b>Temperature (°C)</b>	<b>References</b>
Ti <sub>1.09</sub> Nd <sub>0.01</sub> Fe <sub>0.8</sub> Mn <sub>0.2</sub>	~ 1.75	2.63 (sloping plateau)	40	[75]
Ti <sub>1.1</sub> Fe <sub>0.9</sub> Ni <sub>0.1</sub>	1.3	~ 1 (sloping plateau)	40	[77]
Ti <sub>1.09</sub> Mg <sub>0.01</sub> Fe <sub>0.9</sub> Ni <sub>0.1</sub>	~ 1.3	~ 1	40	[77]
TiFe <sub>1-x</sub> Ni <sub>x</sub> (x = 0 – 0.4)	~ 0.8-1.12	~ 7-9.8 (sloping plateau)	40	[78]
TiFe + 4 wt% Ni	0.65	1.2	40	[41]
TiFe <sub>0.86</sub> Mn <sub>0.1</sub> Y <sub>0.05</sub> Cu <sub>0.05</sub>	1.89	~ 1.3 (sloping plateau)	10	[79]
TiFe <sub>0.9</sub> (MP)	1.62	4.7	25	[45]
TiFe <sub>0.9</sub> V <sub>0.05</sub> (MP)	1.88	1.9	25	[45]
TiFe <sub>0.9</sub> V <sub>0.1</sub> (MP)	1.96	1.5	25	[45]
TiFe <sub>0.8</sub> Mn <sub>0.1</sub> (MP)	1.68	1.4	25	[45]
TiFe <sub>0.8</sub> Mn <sub>0.1</sub> V <sub>0.05</sub> (MP)	1.71	~1	25	[45]
TiFe <sub>0.8</sub> Mn <sub>0.1</sub> V <sub>0.1</sub> (MP)	1.76	~1	25	[45]

MP: multiple plateau

### 2.3 Mechanical activation processes

Grain refinement techniques or mechanical activation methods are also an alternative solution to improve the hydrogenation properties of alloys. These processes result in altering the microstructure of alloys and lead to the formation of cracks, vacancies and new grain boundaries which help in easy activation. Ball milling, high pressure torsion, cold rolling and annealing are effective methods for the microstructural modification of alloys.

A lot of research work on the synthesis of TiFe by ball milling (mechanical alloying) of elementary powders [46, 47, 52, 80-84] or ball milling TiFe alloy [43, 66, 80, 83, 85-88] have been reported. In these references, several authors reported that TiFe alloy readily activate after ball milling and no pre activation treatment is required in order to absorb hydrogen at room temperature [52], [83], [85], [86], [88].

Some authors also reported that ball milling process did not activate TiFe alloy, still requiring thermal treatment of milled TiFe compound at high temperature under high hydrogen pressure before first absorption [80], [82], [89]. Literature reports can be divided into two groups, while reviewing the articles since the 1990s. The first group can be called as the ones where *in situ* results are reported where absorption happens at the same place; means in the milling vial i.e. milling done under hydrogen environment [85], [86]. The second group of reports includes the *ex situ* results where milled TiFe compound was activated after milling [52], [83], [88]. Ball milling of TiFe compound by varying the composition (Ti-rich compound) has been also reported [90].

For the activation of alloys, treatment of alloys by severe plastic deformation such as high-pressure torsion (HPT) [91-93], plastic deformation using groove [48] or cold rolling [94] and annealing [50, 51] has been investigated in recent years. Edalati et al. showed the influence of microstructure on the activation of TiFe alloy by formation of cracks and grain boundaries using high-pressure torsion [48, 49, 95, 96]. Vega et al. investigated the effect of cold rolling on the hydrogen storage properties of TiFe [94]. They found that cold rolling of TiFe alloy in inert atmosphere leads to a rapid hydrogen absorption at room temperature. All these processes resulted in better activation kinetics of TiFe alloy. Abe and Kuji observed that plateau pressure decreases ( $\sim 1$  MPa) for TiFe prepared by the combination of ball milling and post-annealing [52].

A summary on the effect of various mechanical activation methods on the hydrogenation properties of TiFe alloy has been shown in **Table 2.2**.

**Table 2.2: The hydrogenation properties of TiFe via different mechanical activation methods**

<b>Activation method</b>	<b>Grain size (<math>\mu\text{m}</math>)</b>	<b>Maximum hydrogen capacity (wt%)</b>	<b>Desorption plateau pressure, P (atm)</b>	<b>Temperature (<math>^{\circ}\text{C}</math>)</b>	<b>References</b>
Annealing	~ 750	< 0.2	-	30	[95, 97]
Groove rolling	1	1.7	~ 4 (fifth cycle)	30	[48, 97]
HPT	0.1	~ 1.7	~ 4	30	[95, 97]
Ball milling	0.01	1.5	~ 1-7 (sloping plateau)	30	[88]
Cold rolling	0.01	1.4	-	Room temperature	[94]

# Chapter 3

## Experimental Details

---

### 3.1 Introduction

The experimental details of the work done are mentioned in this part of the chapter. They are divided into three parts: (1) alloy synthesis by arc melting or induction melting, (2) Characterization by scanning electron microscopy/energy-dispersive X-ray spectroscopy (SEM/EDS) and X-ray diffraction and (3) hydrogen sorption measurements on a Sieverts apparatus.

Synthesis of TiFe alloys with Zr, Mn and V as additives was carried out by GKN industry using induction melting. For the cooling rate effect, step mold was utilized for the melted composition using induction melting at CMQ industry. Heat treatment effect and Ti/Fe ratio effect were performed at laboratory scale at UQTR. Cooling rate and heat treatment effects were examined for TiFe with Zr as additive in order to optimize synthesis parameter. Effect of Ti/Fe ratio on the hydrogenation behaviour of TiFe + 4 wt% Zr was also studied in order to optimize chemical composition.

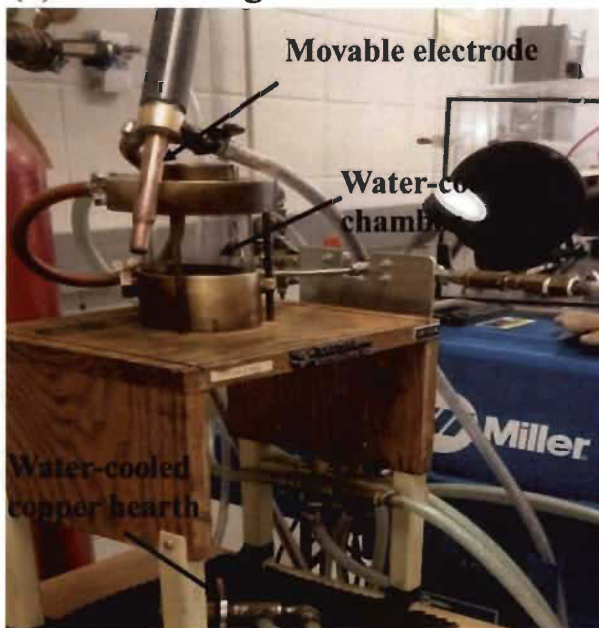
### 3.2 Starting material

Industrial steel grade (AISI 1005) and commercial titanium (ASTM B265 grade 1) were used as starting raw materials for the synthesis of TiFe alloy. Zirconium alloy 702 (99.2 wt% Zr), Ferrovandium (80.09 wt% V, 18.75 wt% Fe, 0.85 wt% Al, 0.04 wt% P, 0.23 wt% C, and 0.04 wt% S) and electrolytic manganese (99.7%) were used for the synthesis of TiFe alloy with the Zr, Mn and V additives. At laboratory scale, pure element Zr (99.5%) from Alfa Aesar was utilized for the synthesis of TiFe + 4 wt% Zr.

### 3.3 Alloy synthesis

Arc melting and induction melting were respectively used for the laboratory scale and industrial scale synthesis. **Figure 3.1** shows the arc melting furnace and induction melting furnace.

(a) Arc melting furnace



(b) Induction melting furnace



Figure 3.1: Arc melting facility at UQTR and Induction melting facility at industry

Arc melting consists of movable electrode, water-jacketed chamber, copper-cooled hearth and vacuum system. In arc melting, raw materials are heated by an electric arc. In induction melting process heat is applied through induction. At laboratory scale, ~3 g of sample was synthesized by arc melting. Consarc induction skull melting furnace (ISM) was utilized for the synthesis of industrial scale samples as shown in **Figure 3.2(b)**. The size of the melt was 6.5 kg.

### 3.3.1 TiFe with Zr, V and Mn (synthesized by Industry)

TiFe with Zr, V, and Mn (see **Table 3.1**) were synthesized by GKN Powder Metallurgy. In the first batch, nine alloys of TiFe base alloy with different additives were made. TiFe alloy without any additive (Heat#5) was used as a baseline. TiFe alloys with Zr, V and Mn as additives were synthesized to see the comparative effect of these additives on the hydrogenation properties of TiFe alloy. TiFe alloy with different combinations of additives (Zr and Mn, Mn and V, Heat#1, 2, 3 and 4) had also been synthesized to see the possible synergetic effect.

**Table 3.1: Chemical composition (in mass %) of samples synthesized by GKN Powder**

	<b>Fe</b>	<b>Ti</b>	<b>Mn</b>	<b>V</b>	<b>Zr</b>	<b>C</b>	<b>S</b>	<b>O</b>	<b>N</b>
<b>Heat#1</b>	46.11	50.74	1		2	0.026	0.001	0.17	0.006
<b>Heat#2</b>	44.61	49.14	2.48		3.6	0.013	0.001	0.13	0.003
<b>Heat#3</b>	45.84	49.69	2.32	1.94		0.014	0.001	0.16	0.006
<b>Heat#4</b>	44.92	49.42	1.73	3.78		0.009	0.001	0.15	0.011
<b>Heat#5</b>	53.9	45.94				0.011	0.001	0.15	0.004
<b>Heat#6</b>	51.5	46.48			1.85	0.008	0.001	0.13	0.004
<b>Heat#7</b>	50.6	45.63			3.72	0.023	0.001	0.09	0.002
<b>Heat#8</b>	52.19	45.88		1.88		0.019	0.001	0.11	0.003
<b>Heat#9</b>	50.83	45.65		3.5		0.012	0.001	0.07	0.007
<b>Heat#10</b>	50.48	47.69	1.75			0.013	0	0.07	0.0036
<b>Heat#12</b>	48.46	48.04	2.51	0.870		0.053	0.001	0.11	0.019
<b>Heat#15</b>	44.86	47.71	4.04	3.29		0.024	0.001	0.09	0.009
<b>STD</b>	45.4	48.7	5.9						
<b>Heat#25</b>	45.67	50.03		1.97	2	0.02		0.13	0.01
<b>Heat#26</b>	44.30	49.20	2.05	2.01	2.01	0.03		0.2	0.01

\* Heat#1-10, 12, 15, 25, 26 represents the name of the alloy which is given by Industry for different alloy's composition.

\*\* STD (standard) is notation given by Industry for 6 wt% of Mn.

There was not any sample of TiFe alloy only with Mn as an additive during the first batch sample. Therefore, in the second batch sample, TiFe with different weight percent of Mn (Heat#10, STD) were synthesized by GKN Powder Metallurgy. Two samples of TiFe with the combination of Mn and V (Heat#12 and Heat#15) were also synthesized by varying the weight percent of Mn and V. Combination of Zr and V (Heat#25) were also synthesized to compare with the samples having only Zr and only V. Three additives Zr, Mn and V were added simultaneously at a concentration level of 2 wt% (Heat#26) to see the effect on the hydrogenation properties and microstructure of TiFe alloy as compared to other additives.

### **3.3.2 Heat treatment**

Pellets of TiFe + X wt% Zr (X = 4, 8) of about 3 g were synthesized by arc melting. In the process of arc melting, alloys were turned over three times in order to get homogeneity. Two pellets of each composition were synthesized by arc melting: one was kept in as-cast condition and the other was heat-treated at 1173 K for 24 h under argon atmosphere. After heat treatment, the ingot's surface was scratched off using sandpaper to remove oxide layer on the surface. Also, it must be stressed that the ingots were crushed in a glove box before hydrogenation.

### **3.3.3 Cooling rate**

Ingots of TiFe + 4 wt% Zr were synthesized under vacuum using a Consarc induction skull melting furnace (ISM). The size of the melt was 6.5 kg. Industrial steel grade (AISI 1005), commercially pure titanium (ASTM B265 grade 1) and zirconium alloy 702 (99.2 wt% Zr) were used as raw material. Firstly, Fe was melted then Ti and Zr were added to synthesize the alloy. For varying the cooling rate, a ductile cast iron step mold of 25 mm, 13 mm, 6 mm and 3 mm thickness was used (**Figure 3.2**). The size of the cast part was 225 mm in length and 100 mm wide.



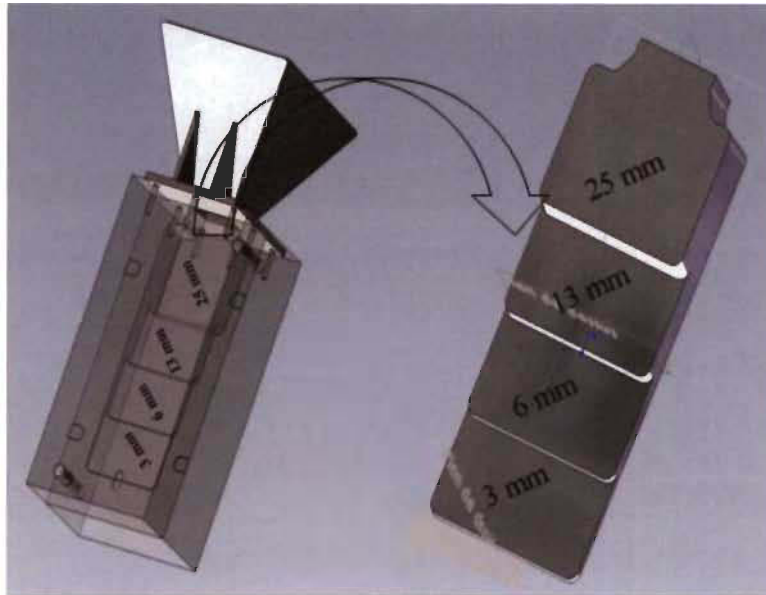


**Figure 3.2: Step molds for varying cooling rate during alloy synthesis**

The mold was placed in the chamber in the upright position. Temperature was taken with an infrared pyrometer from the top of the vacuum chamber. However, it should be pointed out that copper water cooled ISM (induction skull melting) does not permit giving high superheat to the melt. A balance between the heat extraction of the copper mold and the heat input by the induction happens and a superheat of only 75 to 150 °C can be obtained depending on the melt composition, i.e.: its heat conduction and coupling with the induction. As for the shrinkage in the cast part, the mold was designed so that the shrinkage was happening in the riser. Four samples at different cooling rates were prepared. All ingots of different thicknesses were crushed in air into small chunks for further experiments.

### **3.3.4 Synthesis of $Ti_xFe_{2-x} + 4 \text{ wt}\% \text{ Zr}$ , ( $x = 1.1, 1.05, 0.99, 0.94$ )**

Four samples of  $Ti_xFe_{2-x} + 4 \text{ wt}\% \text{ Zr}$ , where,  $x = 1.1, 1.05, 0.99, 0.94$ , ~ 3 g were synthesized by arc melting. Alloys were turned over three times during melting to acquire homogeneity. These alloys were prepared in order to optimize chemical composition and understand the effect of Ti-rich phase on the activation behaviour and microstructure of TiFe alloy.

### 3.4 Alloy characterization

The microstructure of all alloys and the chemical composition of each phase were recorded using Hitachi SU-3500 scanning electron microscope equipped with an EDX (Energy Dispersive X-ray) Spectrometer from Oxford Instruments. Metallographic observations were made in the cross-section of the ingots. All samples were polished before observation. For each phase and each sample, four small areas have been analyzed in order to estimate the uncertainty and reproducibility.

The crystal structure of all samples was determined from X-ray powder diffraction patterns acquired using a Bruker D8 Focus X-ray with Cu  $\alpha$  radiation. For the cooling rate investigation, the X-ray diffraction patterns were recorded using Panalytical X'Pert Pro (PW3050/60) X-ray diffraction with Co  $\alpha$  source. Lattice parameter and crystallite size were evaluated from Rietveld method using Topas software and fundamental parameters approach [98].

Hydrogen storage properties of all these samples were measured on a homemade Sieverts apparatus. Image J software was used to compute the area and perimeter of different phases in the SEM micrograph of each alloy [99].

#### 3.4.1 Scanning electron microscopy (SEM)

Scanning electron microscopy is widely used to study the morphology and chemical composition analysis of a range of materials. SEM consist of an electron gun producing an electron beam, magnetic lenses to focus the electrons, electron detector, vacuum chamber (**Figure 3.3**). When a high-energy electron beam focused through the magnetic lenses strikes the surface of the sample, the excited region produces many types of electrons such as secondary electrons, back-scattered electrons, Auger electrons and transmitted electron. Morphology and topography of samples can be studied by detecting secondary electrons. Back-scattered electrons strongly depend on atomic number of elements which is useful to study multiphase samples.

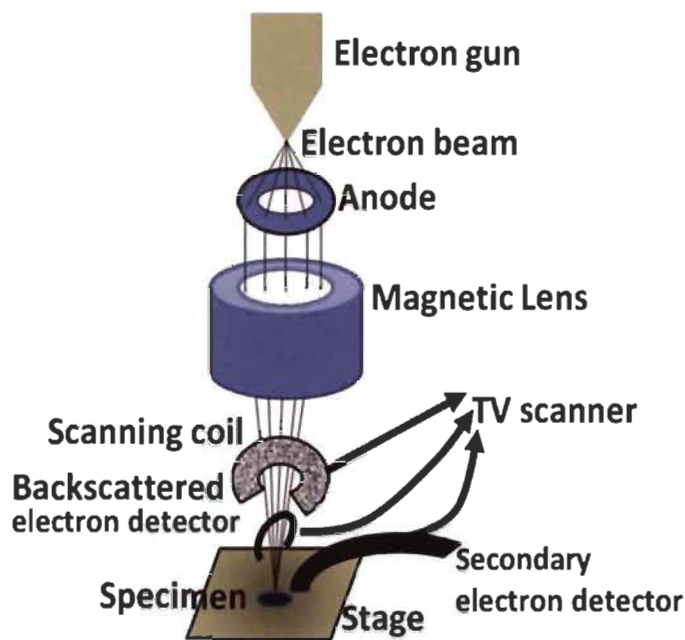
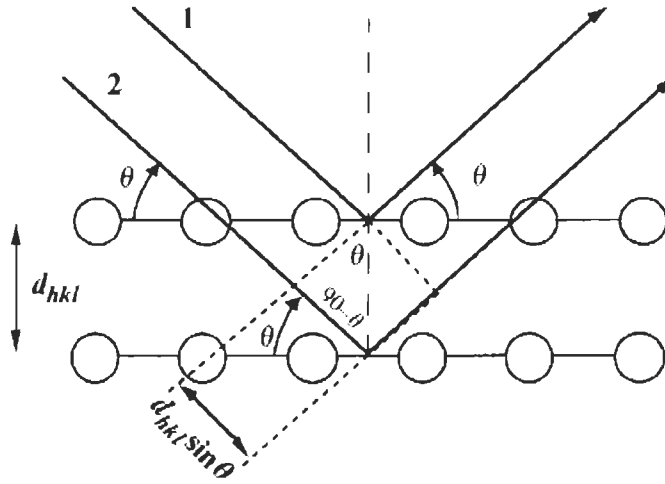


Figure 3.3: The set-up of scanning electron microscope [100]

When a high-energy electrons beam bombarded on specimen, it results in creating positively charged “electron holes” in the occupied bands. The “holes” are then filled by electrons of the higher states. Attraction of electron from the higher state to the “holes” results in the emission of X-rays. Each element gives a unique energy characteristic of X-rays. Energy dispersive spectroscopy detects the emitted X-rays and gives information about the elemental composition of the selected area or volume. Three consecutive measurements of EDX analysis were made for the same phase at different area in the back scattered image. Thereafter, the average value was calculated and accordingly gave the uncertainty.

### 3.4.2 X-ray diffraction

X-ray diffraction (XRD) technique is generally used to determine the crystal structure of crystalline matter. In 1913, Bragg proposed one theory to explain the pattern that was obtained from the scattering of X-rays after interaction with crystalline material [101]. Bragg’s observation can be illustrated by the schematic diagram shown in **Figure 3.4**. In this schematic diagram, each plane of atoms acts as a source of scattered radiation and diffraction occurs when the distance between sources is comparable to the wavelength of radiation.



**Figure 3.4: Schematic diagram for the formulation of Bragg's diffraction [102]**

Equation 3.1 is the Bragg's law equation which correlates the wavelength of electromagnetic radiation and the angle of scattered radiation with the crystal's inter-planar distance.

$$2d_{hkl} \sin \theta = n\lambda \quad (3.1)$$

Where  $\lambda$  is the wavelength,  $\theta$  is the Bragg's angle and  $d$  is the inter-planar distance. The inter-planar distance ( $d$ ) can be obtained by knowing the Miller indices ( $h, k, l$ ) and the lattice parameter ( $a, b, c$ ). For orthogonal crystal system, a correlation formula of  $d$  value with Miller indices and lattice parameters can be given by equation 3.2.

$$\frac{1}{d^2} = \frac{h^2}{a^2} + \frac{k^2}{b^2} + \frac{l^2}{c^2} \quad (3.2)$$

Each phase has its own specific crystal structure and lattice parameter. X-ray diffraction pattern analysis helps us in phase identification using important information such as lattice parameter, crystallite size, microstrain obtained from the pattern's analysis of a material.

### 3.4.3 X-ray fluorescence

X-ray fluorescence (XRF) technique is widely used for the elemental analysis of all kind of material. In XRF, when high energy X-ray photon irradiates the material, it results in the ejection of inner shell electron and creating a hole as shown in **Figure 3.5**. This hole can be occupied by the upper shell electron which results in producing X-ray fluorescence radiation. This x-ray

fluorescence radiation has specific characteristic for each element as energy emitted is proportional to the binding energy of the element.

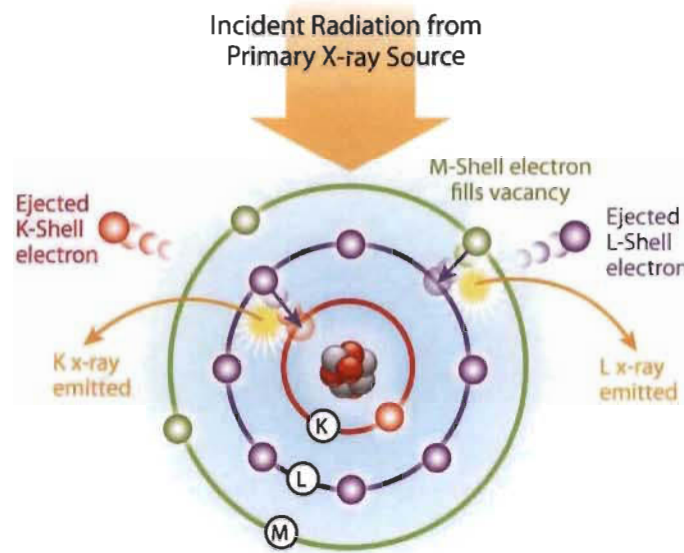


**Figure 3.5: Schematic diagram of production of X-ray fluorescence radiation [103]**

The incident X-ray energy must be higher than the binding energy of the electron in order to expel the electron from the inner shell. This technique is very useful in a broad range of applications.

### 3.4.4 Sieverts apparatus

In this research, all sorption measurements were carried out on a homemade Sieverts apparatus. Sieverts apparatus is the most widely used for hydrogen gas sorption measurement. This is also known as volumetric method. Schematically, in this method, there are two known volume  $V_1$  and  $V_2$  as shown in **Figure 3.6**. There are three valves A, B and C where valve A controls the hydrogen inlet, valve B controls the evacuation down to atmospheric pressure and valve C controls the vacuum outlet below atmospheric pressure. Valves D and E allow the introduction or removal of gas to or from volume  $V_1$  and  $V_2$  respectively. There are high and low-pressure gauges to measure the pressure. The hydrogen sorbed by a sample is calculated using real gas law,

$$PV = nZRT \quad (3.3)$$

Where  $n$  is the number of moles of hydrogen and  $Z$  is the gas compressibility,  $P$  is the pressure,  $V$  is the volume,  $R$  is the universal gas constant and  $T$  is the temperature.

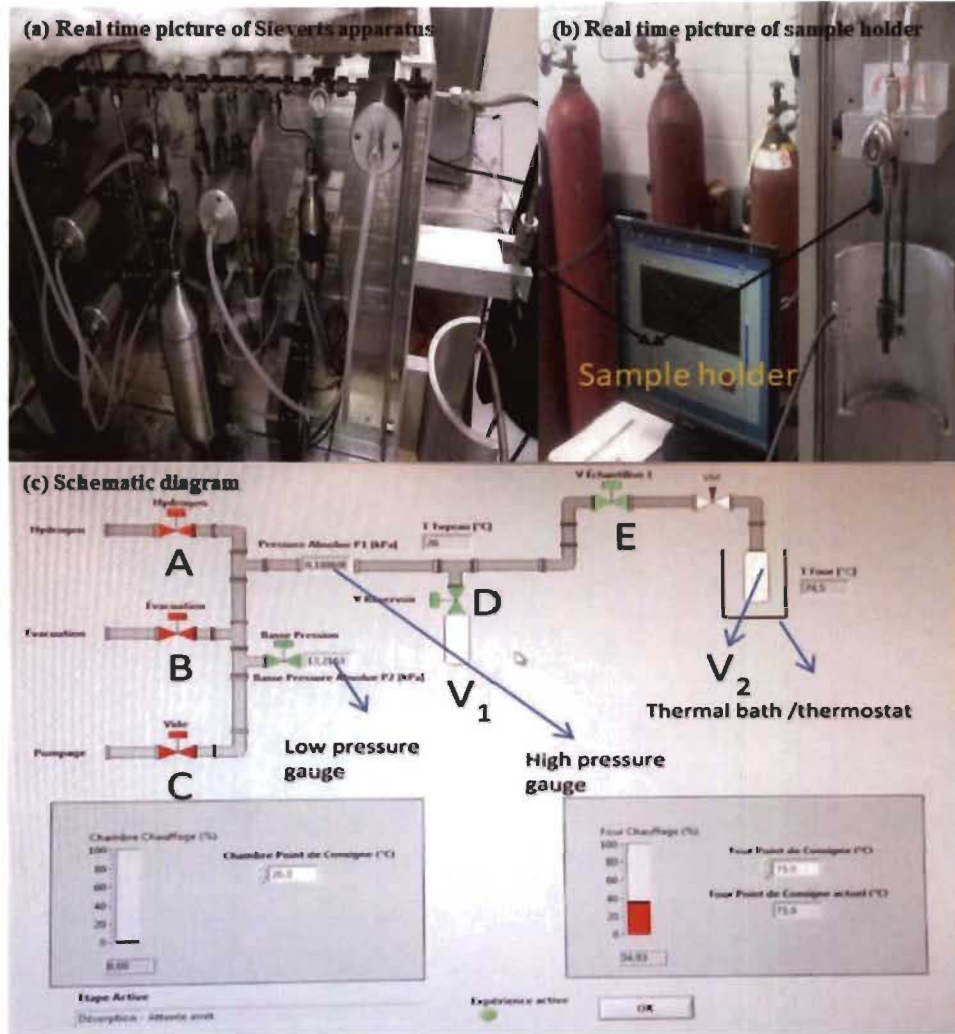


Figure 3.6: Real time picture and schematic diagram of Sieverts apparatus with different components

In sorption process, firstly, sample is loaded in sample holder and kept under dynamic vacuum for 1 hour by opening valve C and valve E. After that, hydrogen is allowed to the volume  $V_1$  by opening valve A and closing valve E with initial hydrogen pressure  $P_i$ . Thereafter, valve A is closed, and valve E is opened to fill  $V_2$ . Pressure will drop due to volume difference  $V_1$  and  $(V_1+V_2)$ . Any further drop of pressure will be due to the absorption of hydrogen by the sample. The experiment is performed at constant temperature  $T$  and the final measured pressure is  $P_f$ , the number of moles sorbed is given by,

$$\Delta n = \frac{P_i V_1}{Z_{i,T} RT} - \frac{P_f (V_1 + V_2)}{Z_{f,T} RT} \quad (3.4)$$

Where,  $Z_{i,T}$  and  $Z_{f,T}$  are the compressibility factor of hydrogen at temperature  $T$  and the pressure  $P_i$  and  $P_f$ , respectively.

The compressibility factor during hydrogen sorption measurements was taken 1 for hydrogen gas. For the hydrogen absorption or desorption measurements on a Sieverts apparatus, the synthesized samples were crushed into powder in an argon atmosphere using a hardened steel mortar and pestle and around 1 g of powder was filled in the reactor and kept under dynamic vacuum for one hour before hydrogen sorption measurements. First hydrogenation curve of all samples was measured at room temperature under 20 bar hydrogen pressure. Reactor temperature was controlled using an air furnace. To have a better heat conductivity and also a bigger thermal mass, an annulus of copper was in close thermal contact to the reactor. This restricted the temperature change during hydrogenation or dehydrogenation to a few degrees at maximum.

## Chapter 4

# Microstructure and hydrogen storage properties of TiFe alloys with Zr, V and Mn as additives

---

### 4.1 Introduction

In this chapter, the results of TiFe alloys with different additives i.e. Zr, V, and Mn are being reported. The reason for selection of these three elements is as follows: Zr is very effective to enhance the first hydrogenation [65]; Mn is also known to facilitate the activation kinetics [44] and V is a well-known catalyst for hydrogenation of various metal hydrides [45]. Combination of these elements has been made in order to study a possible synergy between these different additives. The study reported includes the results on the alloys cast by GKN Powder Metallurgy using industrial grade raw materials.

### 4.2 Activation kinetics of alloys (in granules form) shown in Table 3.1

Samples received from the company were in two forms: granules of about 40 mesh and ingots (Table 3.1). First form; the granules were in the vial with the closed lid for many days without any argon atmosphere and it was tested for activation by filling it in the reactor directly in the air. First hydrogenation (activation) curves of the granules of all samples were observed at room temperature under 20 bar hydrogen pressure.

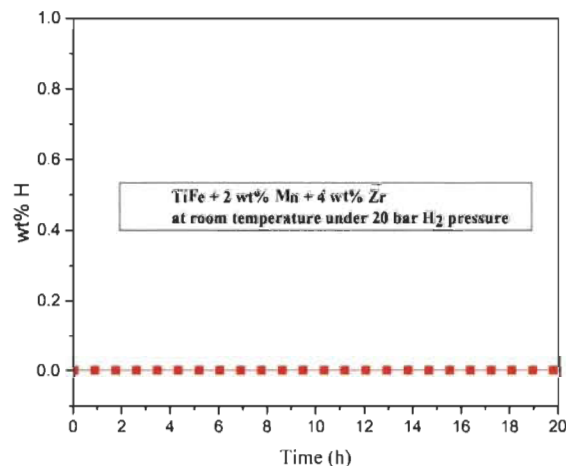
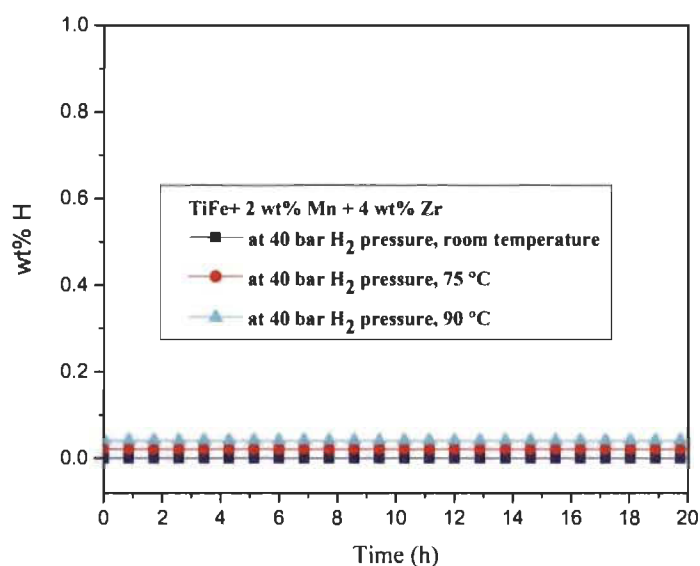


Figure 4.1: Activation curve of TiFe + 2 wt% Mn + 4 wt% Zr (in granules form) at room temperature under 20 bar hydrogen pressure



A representative graph of activation curve for TiFe + 2 wt% Mn + 4 wt% Zr (Heat#2) granules is shown in **Figure 4.1**. Under these conditions, none of the alloys absorbed hydrogen, which was a surprising result considering that, on a laboratory scale, TiFe alloys with Zr additive have been proved to be able to absorb hydrogen. In order to help the first hydrogenation, we decided to increase the temperature and pressure for selected alloys TiFe + 2 wt% Mn + 4 wt% Zr (Heat#2) and TiFe + 4 wt% Zr (Heat#7). These two compositions were selected because, in our opinion, they were the most susceptible to have good activation kinetics. Therefore, tests were performed on these two alloys at 75 °C and 90 °C under 40 bar of hydrogen. Results for TiFe + 2 wt% Mn + 4 wt% Zr as a representative of activation curve are shown in **Figure 4.2** and it is clear that even under these more drastic conditions there was no hydrogenation.



**Figure 4.2: Activation curve of TiFe + 2 wt% Mn + 4 wt% Zr at room temperature, 75 °C, and 90 °C under 40 bar hydrogen pressure**

For the measurement of laboratory scale samples, we usually synthesize a ~ 3 g pellet which is crushed in argon atmosphere and filled in reactor. In order to replicate the same procedure for the industrial samples, small chunks of all industrial samples were taken and crushed in argon atmosphere. First hydrogenation curves of all these samples were measured at room temperature under 20 bar hydrogen pressure (under the same pressure and temperature conditions as in case of

40 mesh powders of samples). Remarkably, when prepared this way, the samples could be activated.

### 4.3 TiFe alloys with only Zr, only Mn and combination of Zr + Mn as additives

In previous work, Peng et al. found that addition of 4 wt% (Zr + 2 Mn) to TiFe alloy improves the activation of TiFe alloy but kinetics is still slow [58]. This justified the study of the effect of individual elements (Zr, Mn) as additive and also combination of these two elements on the kinetics of first hydrogenation of TiFe alloy. The bulk composition of all alloys, as measured by X-ray fluorescence spectrometer (Bruker XRF S1titan), are shown in **Table 4.1** and compared with the nominal composition of each alloy. The measured composition is close to the nominal one but, it is seen that for manganese containing alloys the amount of titanium is higher and iron is lower than the nominal values. In fact, this discrepancy seems to get bigger as manganese concentration increases.

**Table 4.1: Bulk chemical analysis: nominal and as measured by XRF (X-ray fluorescence) spectrometer of all alloys. Uncertainty on all values is  $\pm 1$  at. %**

Alloy		Ti (at. %)	Fe (at. %)	Zr (at. %)	Mn (at. %)
<b>TiFe (Heat#5)</b>	Nominal composition	50	50		
	Measurement	50	50		
<b>TiFe + 2 wt% Zr (Heat#6)</b>	Nominal composition	50	49	1	
	Measurement	50	48	1	
<b>TiFe + 4 wt% Zr (Heat#7)</b>	Nominal composition	49	49	2	
	Measurement	50	48	2	
<b>TiFe + 1 wt% Mn (Heat#10)</b>	Nominal composition	50	49		<1
	Measurement	51	47		1
<b>TiFe + 6 wt% Mn (STD)</b>	Nominal composition	47	47		6
	Measurement	52	42		6
<b>TiFe + 1 wt% Mn + 2 wt% Zr (Heat#1)</b>	Nominal composition	49	49	1	<1
	Measurement	55	43	1	<1
<b>TiFe + 2 wt% Mn + 4 wt% Zr (Heat#2)</b>	Nominal composition	48	48	2	2
	Measurement	53	42	2	2

## 4.3.1 Result and discussion

### 4.3.1.1 Morphology

Microstructure of all the compositions is shown in **Figure 4.3**. In the microstructure of pure TiFe alloy, small secondary phase (bright grey phase over a uniform grey phase) could be clearly seen. It should be pointed out that, for pure TiFe alloy, the secondary phase abundance was very small. A close-up of a region with secondary phase but is not representative of the whole alloy is shown in **Figure 4.3 (a)**. The other compositions had a more uniform distribution of the secondary phases. The TiFe alloys with only Zr additive (2 wt% and 4 wt%) have grey phase, light grey phase, and a bright phase. The alloy with 2 wt% Zr has much more globular secondary phase compared to the 4 wt% Zr alloy. In the case of 2 wt% Zr, the bright phase is found to be at the edge of light grey phase. However, in the microstructure of TiFe alloy with 4 wt% Zr, the bright phase is more clearly embedded in the light grey phase. The microstructures of alloys with only Mn as additive are shown in **Figure 4.3 (d), (e)**. For low concentration level of manganese (1 wt% Mn), black precipitates and islands of dark grey phase within the main grey phase could be seen. For 6 wt% Mn alloy, the black precipitates are very small. The microstructures of alloys with Zr and Mn simultaneously as additives are shown in **Figure 4.3 (f) and (g)**.

For the addition of 1 wt% Mn and 2 wt% Zr (**Figure 4.3 (f)**), the alloy is made of a main grey phase and a secondary phase that is brighter at its edge. This change of brightness within the secondary phase indicates a variation in chemical composition. A similar situation is seen in alloy with 2 wt% Mn and 4 wt% Zr (**Figure 4.3 (g)**) but with a much more abundant secondary phase. Also, closer inspection (**Figure 4.4**) shows stripes of dark phase inside the secondary phase.

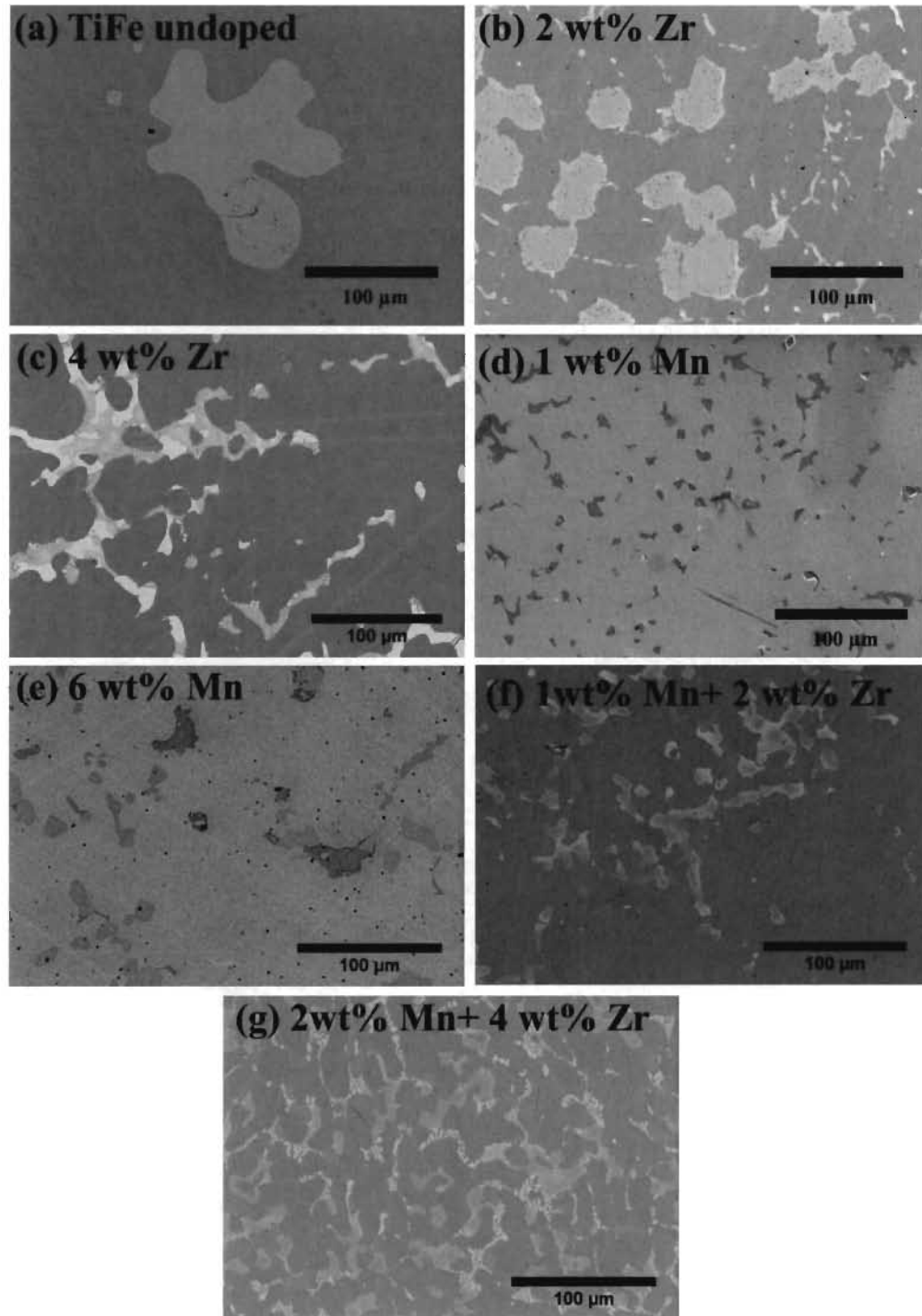


Figure 4.3: Microstructure of (a) as-cast TiFe alloy, TiFe with (b) 2 wt% Zr, (c) 4 wt% Zr, (d) 1 wt% Mn, (e) 6 wt% Mn, (f) 1 wt% Mn + 2 wt% Zr and (g) 2 wt% Mn + 4 wt% Zr

### 2 wt% Mn + 4 wt% Zr

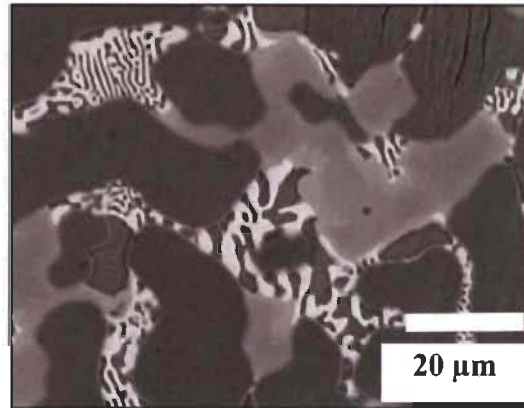


Figure 4.4: Microstructure of TiFe + 2 wt% Mn + 4 wt% at 20 μm scale

The chemical composition of each phase was evaluated by EDX analysis. Elemental mapping using EDX for TiFe alloy is shown in **Figure 4.5**. Area analysis of the grey and bright grey phases are presented in **Table 4.2**. It shows that the bright grey phase has a chemical composition very close to  $\text{TiFe}_2$  which is a phase expected from the phase diagram.

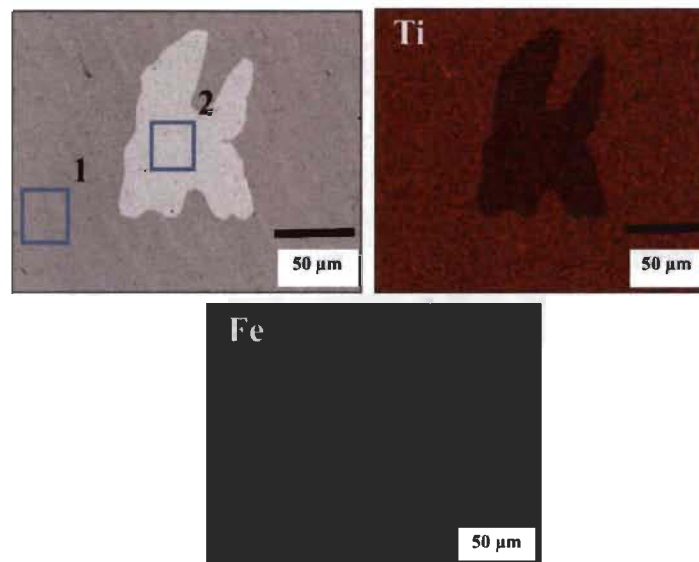
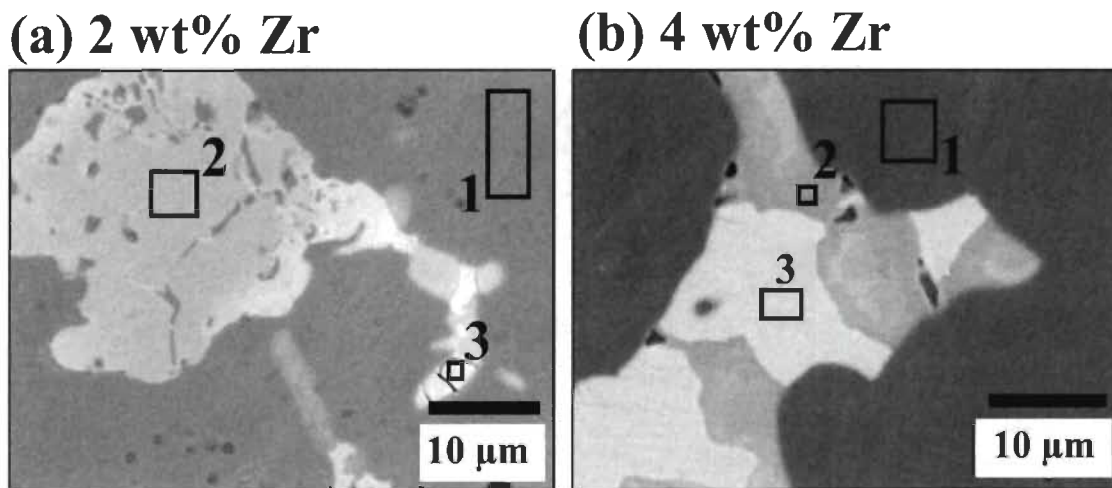


Figure 4.5: EDX analysis and elemental mapping of TiFe

**Table 4.2: Chemical composition of different phases present in TiFe (uncertainty on all values is  $\pm 1$ )**

TiFe	Ti (at. %)	Fe (at. %)
Area 1 (grey phase)	50	50
Area 2 (bright grey phase)	40	60

The area analysis of each phase in TiFe alloys with 2 and 4 wt% Zr only as additive is shown in **Figure 4.6**. The chemical composition of each phase is shown in **Table 4.3**. This confirms that the main grey phase is TiFe. For both alloys, zirconium is essentially concentrated in the bright phase. Bright phase has an average composition close to Ti 40 at. %, Fe 40 at. % and Zr 20 at.%. The light grey phase has a different chemical composition in the two alloys.



**Figure 4.6: EDX analysis of TiFe with Zr as additive (a) 2 wt% Zr and (b) 4 wt% Zr**

For 2 wt% Zr, light grey phase's composition is close to  $TiFe_2$  while for 4 wt% Zr, it is close to  $Ti_2Fe$ . However, it is clear from the micrographs that the bright phase and light grey phase are closely related. One explanation is that during solidification, zirconium is 'expelled' from the light grey phase to form the bright phase.

**Table 4.3: Chemical composition of each phase present in alloys with Zr only as additive (uncertainty on all values is  $\pm 1$ )**

Alloys	Ti (at. %)	Fe (at. %)	Zr (at. %)
<b>TiFe + 2 wt% Zr</b>			
<i>Area 1 (grey phase)</i>	50	50	
<i>Area 2 (light grey phase)</i>	39	58	3
<i>Area 3 (bright phase)</i>	39	42	17
<b>TiFe + 4 wt% Zr</b>			
<i>Area 1 (grey phase)</i>	51	49	< 1
<i>Area 2 (light grey phase)</i>	56	33	12
<i>Area 3 (bright phase)</i>	43	37	20

The EDX analysis of TiFe alloys with Mn only as additive at a concentration level of 1 and 6 wt% is shown in **Figure 4.7**.

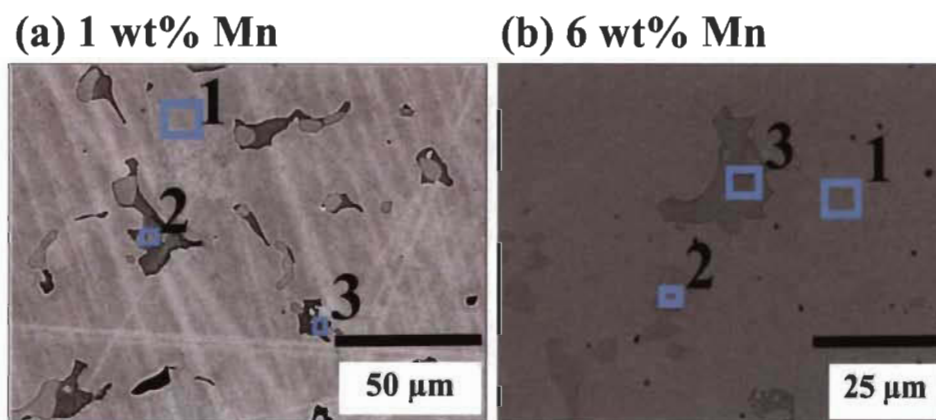


**Figure 4.7: EDX analysis of TiFe alloy with Mn (a) 1 wt%, (b) 6 wt%**

The chemical composition of each phase in TiFe alloys with Mn only as additive is shown in **Table 4.4**. As in the preceding cases, the grey phase is TiFe but here, as Mn content increases, the concentration of Mn in TiFe phase increases. It is also clear that manganese substitute for iron. Light grey phase has a composition close to  $Ti_2Fe$ . Dark grey phase is a Ti-rich phase.

**Table 4.4: Chemical composition of different phases present in each alloy having Mn (uncertainty on all values is  $\pm 1$ )**

Alloy	Ti (at. %)	Fe (at. %)	Mn (at. %)
<b>TiFe + 1 wt% Mn</b>			
Area 1 (grey phase)	52	48	< 1
Area 2 (light grey phase)	67	33	< 1
Area 3 (dark grey phase)	82	18	< 1
<b>TiFe + 6 wt% Mn</b>			
Area 1 (grey phase)	51	43	6
Area 2 (light grey phase)	63	32	6
Area 3 (dark grey phase)	77	17	6

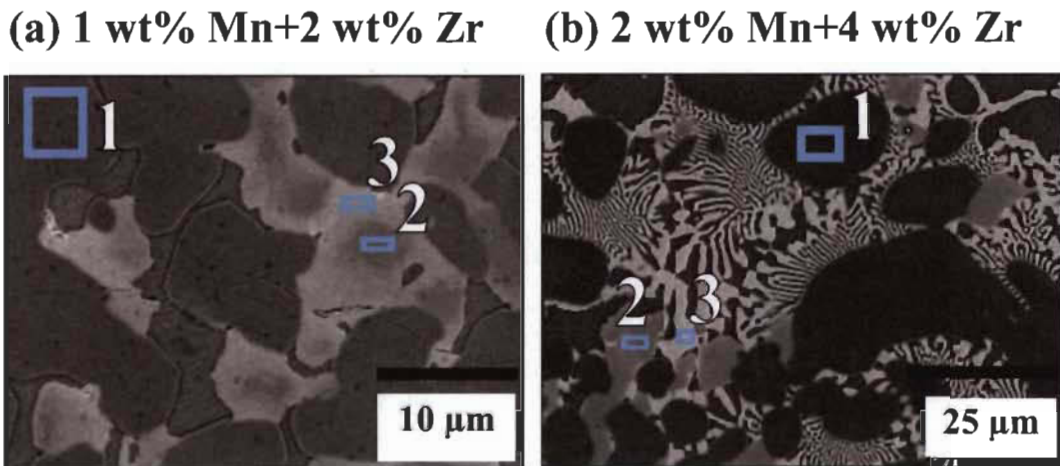


**Figure 4.8: EDX analysis of TiFe alloy with Zr and Mn**

The EDX analysis of alloy having Zr and Mn simultaneously is shown in **Figure 4.8**. The first alloy has 1 wt% Mn and 2 wt% Zr. The second alloy has twice this concentration. There are three phases present in each alloy: (1) grey phase; (2) light grey phase and (3) bright phase. The chemical composition of each phase is shown in **Table 4.5**. As for the other alloys, the grey phase is TiFe. Since, as manganese is one of the additives, the TiFe phase has some manganese that is substituted for iron.



**Table 4.5: Chemical composition of different phases present in each alloy having Zr and Mn (uncertainty on all values is  $\pm 1$ )**

Alloy	Ti (at. %)	Fe (at. %)	Zr (at. %)	Mn (at. %)
<b>TiFe + 1 wt % Mn+ 2 wt % Zr</b>				
Area 1(grey phase)	51	47		< 1
Area 2 (light grey phase)	62	32	4	< 1
Area 3 (bright phase)	56	32	11	< 1
<b>TiFe + 2 wt % Mn+ 4 wt % Zr</b>				
Area 1(grey phase)	50	47		3
Area 2 (light grey phase)	56	31	10	2
Area 3 (bright phase)	43	32	21	2

Light grey and bright phases are Zr-rich phases. The bright phase has a higher proportion of Zr compare to the other two phases. It could be seen that the light grey phase has Zr abundance about  $\frac{1}{2}$  of the abundance in the bright phase.

#### 4.3.1.2 Structural characterization

The X-ray pattern of each alloy is shown in **Figure 4.9** and confirms the presence of a main TiFe (space group Pm-3m) phase with, in most alloys, secondary phases of TiFe<sub>2</sub> type (space group P6<sub>3</sub>/mmc), Ti<sub>2</sub>Fe type (space group Fd-3m) and Ti (space group P6<sub>3</sub>/mmc). From Rietveld refinement, the crystallite size, lattice parameter and phase fraction have been evaluated and the results are shown in **Table 4.6**.

X-ray pattern of TiFe without any additives reveals a main TiFe phase with some minor peaks attributed to TiFe<sub>2</sub>. The presence of these phases in TiFe alloy without any additives is also evidenced by the result of chemical composition analysis of TiFe alloy as shown in **Table 4.2**. For the alloy with 2 wt% Zr only, presence of TiFe and TiFe<sub>2</sub> phases could be seen. At concentration level of 4 wt% Zr, appearance of minor peaks related to Ti<sub>2</sub>Fe phase could be seen along with TiFe main phase. Presence of these phases is in good agreement with the chemical composition analysis of alloys with only Zr (**Table 4.3**).

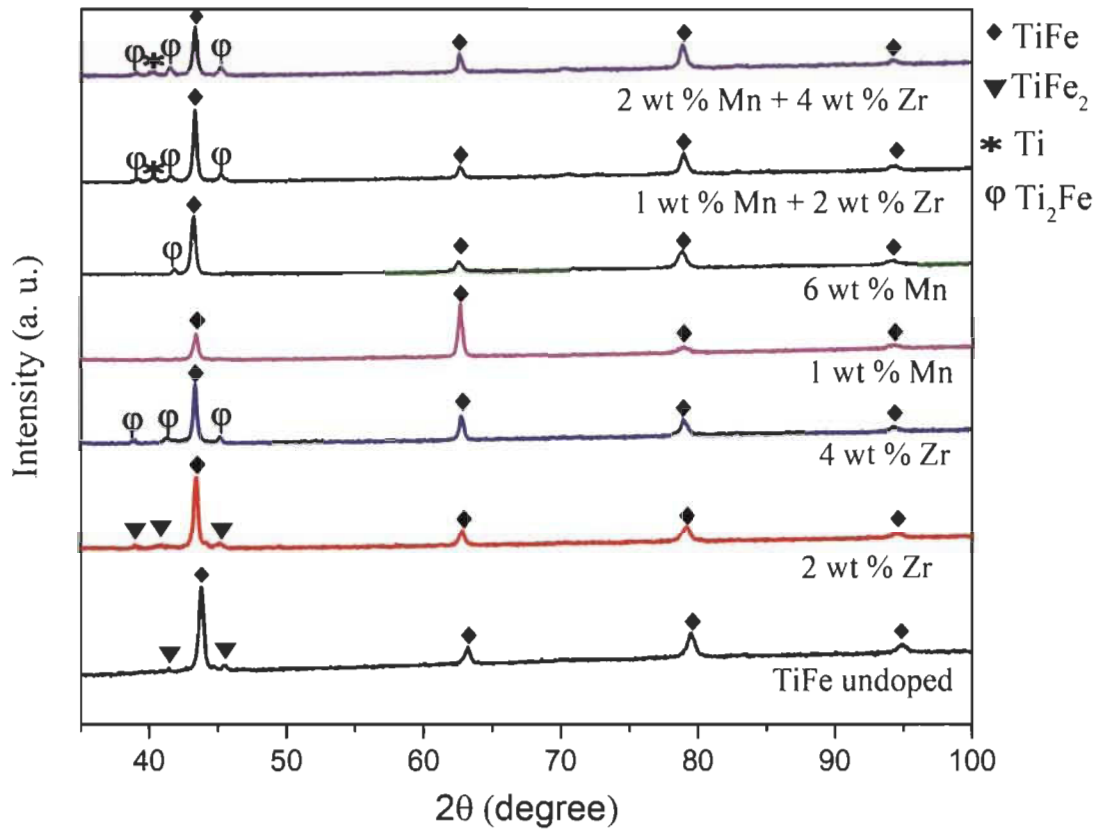


**Figure 4.9: X-ray pattern of TiFe alloys without any additives and with Zr, Mn, and Zr + Mn as additives**

The main cause of the appearance of  $Ti_2Fe$  phase was that addition of Zr at concentration level of 4 wt% leads to the formation of Ti-rich phase ( $Ti_2Fe$ ). X-ray pattern of TiFe alloy with only Mn (6 wt%) shows major peaks of TiFe alloy with minor peaks of  $Ti_2Fe$ . However, at 1 wt% level of Mn, minor peaks of  $Ti_2Fe$  totally disappeared. The main cause of presence of  $Ti_2Fe$  phase along with TiFe in the alloy with 6 wt% Mn only is that addition of Mn leads to a significant reduction of  $TiFe_2$  phase and the formation of Ti-rich phase as recently found by Shang et. al. [76].

**Table 4.6: Phase fraction, lattice parameter and crystallite size for each alloy composition**

Phase name	Phase fraction (%)	Lattice parameter (Å)	Crystallite size (nm)
<b>TiFe without additive</b>			
TiFe	93(1)	a = 2.98(1)	31(1)
TiFe <sub>2</sub>	7(1)	a = 4.71(1) c = 7.97(1)	36(2)
<b>2 wt% Zr</b>			
TiFe	89(1)	a = 2.98(1)	34(2)
TiFe <sub>2</sub>	11(1)	a = 4.84(1) c = 8.10(1)	23(2)
<b>4 wt% Zr</b>			
TiFe	73(1)	a = 2.98(1)	41(2)
Ti <sub>2</sub> Fe	27(1)	a = 11.48(1)	17(2)
<b>1 wt% Mn</b>			
TiFe	100(1)	a = 2.99(1)	40(1)
<b>6 wt% Mn</b>			
TiFe	90(1)	a = 2.99(1)	52(2)
Ti <sub>2</sub> Fe	10(1)	a = 11.32(1)	45(1)
<b>1 wt% Mn + 2 wt% Zr</b>			
TiFe	79(1)	a = 2.99(1)	44(1)
Ti <sub>2</sub> Fe	18(1)	a = 11.42(1)	45(2)
Ti	3(1)	a = 2.99(1) c = 4.67(1)	25(1)
<b>2 wt% Mn + 4 wt% Zr</b>			
TiFe	70(1)	a = 2.99(1)	33(1)
Ti <sub>2</sub> Fe	28(1)	a = 11.44(1)	45(1)
Ti	2(1)	a = 2.99(1) c = 4.77(1)	20(2)

Minor peaks of Ti and Ti<sub>2</sub>Fe phases were observed in the X-ray pattern of TiFe alloy with the combination of Zr and Mn. These minor phases were also seen in chemical composition analysis of alloys with the combination of Zr and Mn. For the Ti<sub>2</sub>Fe-like phase, a close inspection of the EDX results of **Table 4.5** shows that adding the abundance of Ti and Zr gives a total abundance very close to 66 at. % while the abundance of Fe is close to 33 at.%. Thus, it indicates that, in this phase, zirconium seems to substitute for titanium. All phases have almost the same lattice parameter in each alloy.

The crystallite size of TiFe increases with the zirconium content as shown in **Table 4.6**. Unfortunately, because of the limited numbers of data points, the functional form of this increase could not be established. In the same way, addition of manganese increases the crystallite size of TiFe. In this case, the increase is higher than in the zirconium case. An opposite trend is seen for the TiFe<sub>2</sub> phase when only Zr is added to TiFe. We see that the crystallite size of this phase is smaller for 2 wt% Zr addition than for the TiFe alloy. The Ti<sub>2</sub>Fe phase has a constant crystallite size for all alloys with only Mn while the crystallite size is much smaller in the alloy with only Zr addition. It could be concluded that addition of Zr and Mn has an impact on the crystallite size of the phases present in the alloys.

#### **4.3.1.3 Activation kinetics**

First hydrogenation (activation) curves of TiFe alloy with Zr (2, 4 wt%) only, Mn (1, 6 wt%) only, with 2 wt% Mn + 4 wt% Zr and with 1 wt% Mn + 2 wt% Zr as additives are shown in **Figure 4.10**. As it could be clearly seen that TiFe without any additive does not absorb hydrogen. Alloy having 2 wt% Zr could also not be activated. Addition of Zr only is beneficial but a minimum amount of Zr (~ 4 wt% Zr) is essential to activate under the present conditions. The alloys with only Mn addition present an incubation time that increases with increasing Mn content. However, the maximum capacity increases with Mn content. Adding both Zr and Mn brings the benefits of both elements (i.e. no incubation time and better capacity). Clearly, there is some synergetic effect because the kinetics and capacities are much better than what could be achieved by just the sum of what was seen for Zr and Mn alone. The alloy with 2 wt% Mn and 4 wt% Zr has the fastest kinetics and highest capacity. Therefore, it could be concluded that addition of Zr and Mn is beneficial for activation and hydrogen capacity of TiFe alloy.

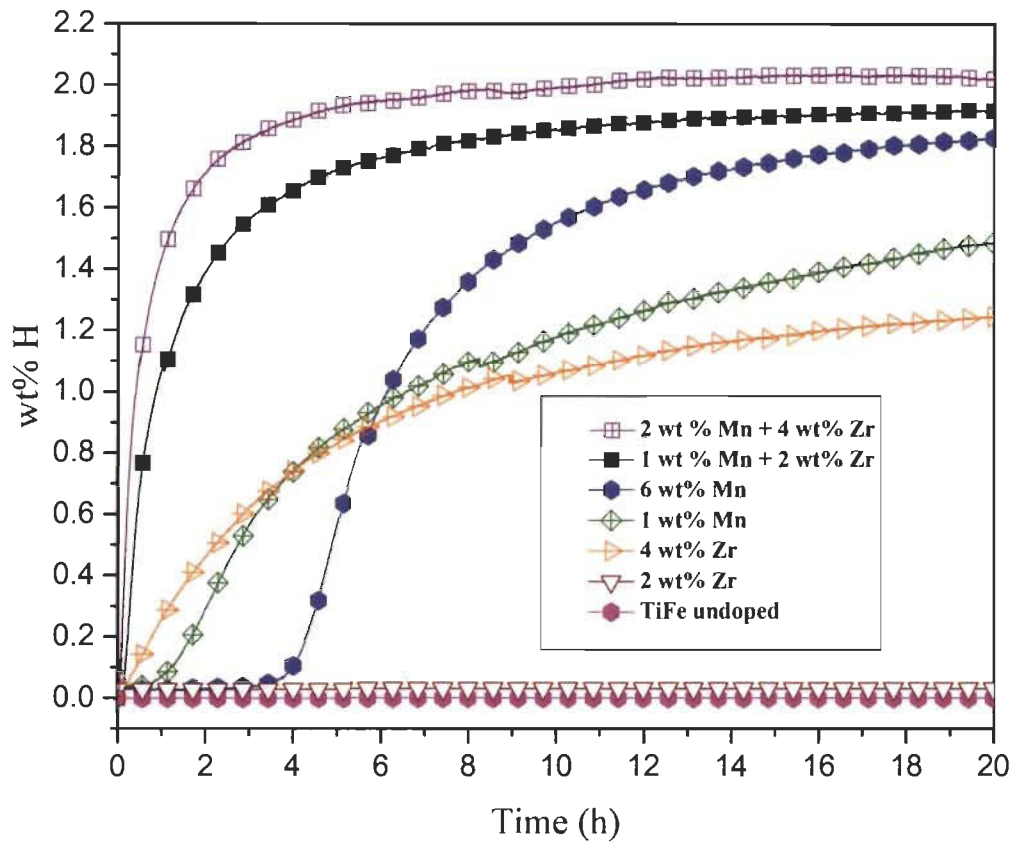


**Figure 4.10: Activation kinetics of all alloys at room temperature under 20 bar hydrogen pressure**

The reason for the faster kinetics and higher capacity of the TiFe alloy with 2 wt% Mn + 4 wt % Zr could be related to the microstructure and chemical composition of the phases. It was seen in **Figure 4.3** that compared to the other alloys, the secondary phase finely and homogeneously distributed within the TiFe phase in the alloy having 2 wt% Mn + 4 wt% Zr. The chemical composition of the secondary phases also plays a role. For both TiFe + 1 wt% Mn + 2 wt % Zr and TiFe + 2 wt% Mn + 4 wt % Zr alloys, the diffraction patterns showed the presence of Ti and Ti<sub>2</sub>Fe phases. It may be the presence of these phases that makes the first hydrogenation very quick and high capacity. Titanium could act as a gateway for hydrogen to enter the TiFe phase. However, more extensive study is needed to test this hypothesis. Guéguen et. al. already showed the importance of Ti-rich (Ti<sub>2</sub>Fe, Ti) phases for easy activation and improving kinetic [45].

#### 4.3.1.4 Rate limiting step of first hydrogenation

A clear difference among the first hydrogenation kinetics of activated alloys could be seen in **Figure 4.10**. Change in the rate limiting step may be the cause for the different first hydrogenation kinetics. The usual rate limiting step model equations are described in **Table 4.7** which summarizes the chemisorption, nucleation-growth-impingement, contracting volume and Ginstling-Brounshtein models. The best way to know the rate limiting step is to do the linear regression for the plot of the left side of the equation as a function of time for each model.

**Table 4.7: Model equations for rate limiting step determination**

Rate limiting step model name	Model equation	Description
Chemisorption	$X = kt$	Surface controlled [104]
Nucleation-growth-impingement model (JMA2D)	$[-\ln(1-X)]^{1/2} = kt$	2D growth of existing nuclei with constant velocity [104, 105]
Nucleation-growth-impingement model (JMA3D)	$[-\ln(1-X)]^{1/3} = kt$	3D growth of existing nuclei with constant velocity [104, 105]
Contracting volume (CV2D)	$1-(1-X)^{1/2} = kt$	2D growth with constant interface velocity [104]
Contracting volume (CV3D)	$1-(1-X)^{1/3} = kt$	3D growth with constant interface velocity [104]
Ginstling-Brounshtein model (GB2D)	$(1-X) \ln(1-X) + X = kt$	2D growth, diffusion controlled with decreasing interface velocity [106]
Ginstling-Brounshtein model (GB3D)	$1-(2X/3) - (1-X)^{2/3} = kt$	3D growth, diffusion controlled with decreasing interface velocity [104]

The best linear fitted model will give information about mechanism of hydrogenation. In these equations, X is the transformed factor which represents the ratio of the absorbed hydrogen quantity divided by the alloy's maximum hydrogen absorption capacity ( $X = \%H/\%H_{\max}$ ), k is the reaction constant and t is time. The linear regressions were performed for 10% to 90 % of the transformed factor ( X = 0.1 to 0.9) as shown in the previous rate limiting studies [107] and fitted curves are

shown in **Figure 4.11** for each activated alloys. The adjusted  $R^2$  values for the linear regression of each alloy's model curve are shown in **Table 4.8**. It shows that adjusted  $R^2$  value for GB3D model is closer to 1 than any other model. It clearly shows a good linear fitting for the GB3D model. Therefore, rate limiting step for each activated alloy was found to be three-dimensional growth, diffusion controlled with decreasing interface velocity.

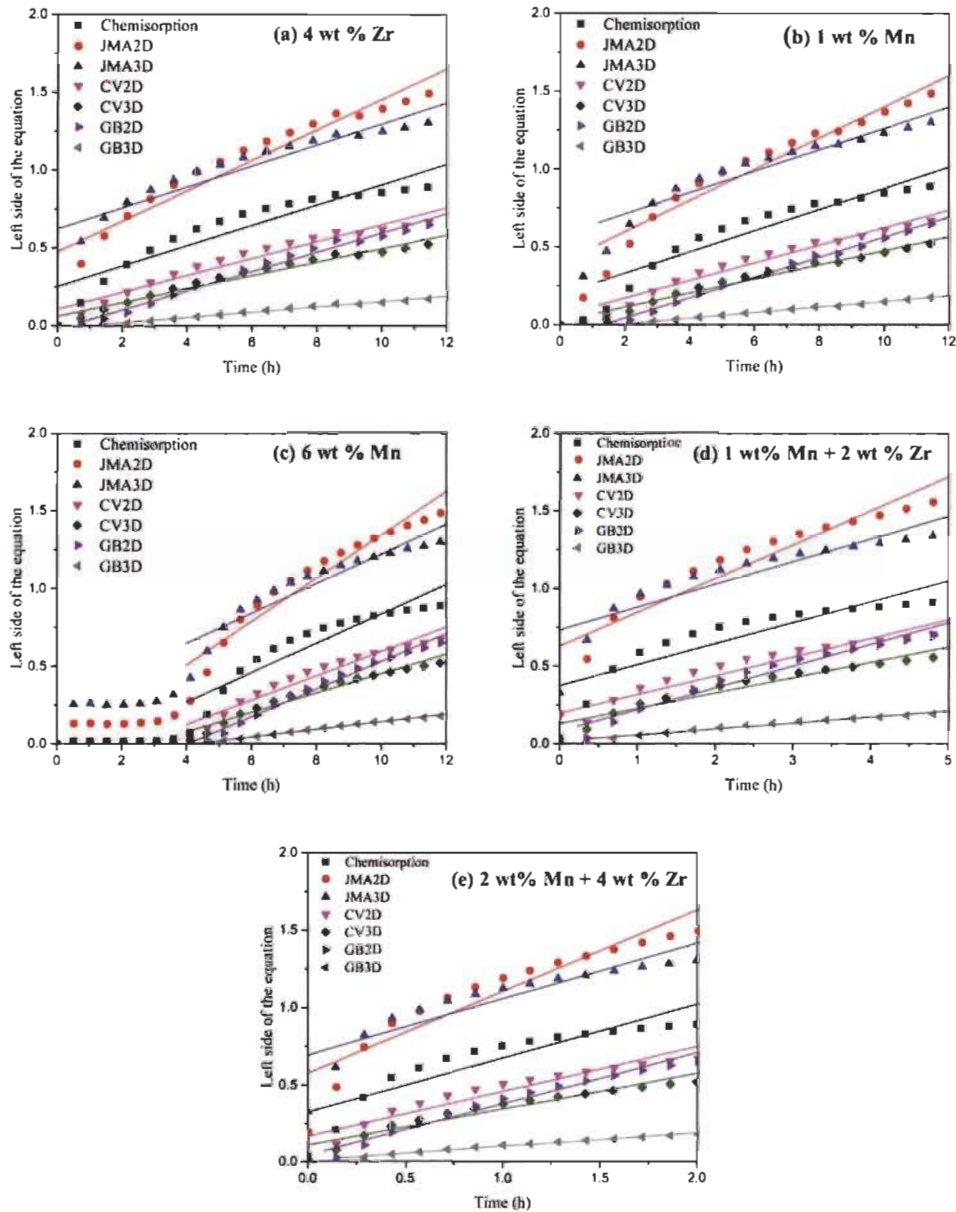


**Figure 4.11:** Linear fitting of each rate limiting step model for each activated alloy (a) for 4 wt % Zr, (b) 1 wt% Mn, (c) 6 wt% Mn, (d) 1 wt% Mn + 2 wt% Zr and (e) 2 wt% Mn + 4 wt% Zr

GB3D model is generally improvisation of Jander model where diffusion controlled reaction happens with the change in the interface diffusion area. While in the Jander, the constant interface diffusion area were assumed.

**Table 4.8: Adjusted R<sup>2</sup> value for the linear regression of Model equations shown in Table 4.7**

Adjusted R <sup>2</sup>	Chemisorption	JMA2D	JMA3D	CV2D	CV3D	GB2D	GB3D
<b>4 wt% Zr</b>	0.87440	0.93112	0.88798	0.944877	0.96724	0.98505	<b>0.99031</b>
<b>1 wt% Mn</b>	0.88476	0.94378	0.90872	0.95753	0.97452	0.98501	<b>0.99745</b>
<b>6 wt% Mn</b>	0.86447	0.92667	0.88734	0.94198	0.96201	0.98742	<b>0.99415</b>
<b>1 wt % Mn + 2 wt% Zr</b>	0.76697	0.86706	0.80557	0.89401	0.92768	0.96104	<b>0.97969</b>
<b>2 wt % Mn + 4 wt% Zr</b>	0.80465	0.87823	0.82225	0.90428	0.93182	0.97406	<b>0.98631</b>

### 4.3.2 Summary

Microstructure and hydrogen storage properties of TiFe without any additives and with addition of Zr or Mn or a combination of Zr and Mn were studied. The following conclusion could be drawn:

1. Addition of zirconium is effective in terms of improving first hydrogenation kinetics compared to TiFe alloy without any additive but a certain level of zirconium (4 wt%) is necessary.
2. Addition of 1 wt% Mn is effective, but kinetics is very sluggish.
3. Simultaneous addition of 1 wt% Mn + 2 wt% Zr to TiFe alloy results in better kinetics and hydrogen capacity compared to alloys having Zr only and Mn only. It absorbs 1.8 wt% of hydrogen in 7 hours.
4. The fastest and highest capacity measured was for the TiFe alloy with simultaneous addition of 2 wt% Mn and 4 wt% Zr. Hydrogen capacity for this alloy was 2 wt%. This fast first hydrogenation kinetics is attributed to the presence of a large proportion of Ti<sub>2</sub>Fe type phase into which zirconium substitute for titanium.
5. The rate limiting step during the first hydrogenation for activated alloys was found to be a three-dimensional growth where diffusion controlled with decreasing interface velocity.



#### 4.4 TiFe alloy with V only, Zr + V and combination of Zr + Mn + V as additives

In the previous section (section 4.3), industrial alloys with only Zr, or, only Mn either combination of these two elements were investigated. It was found that addition of Zr is effective but a certain level (4 wt%) of zirconium is essential. In this section, alloy with the combination of 2 wt% Zr + 2 wt% V has been studied to investigate the possibility of lowering the level of Zr. Alloy with only V (at concentration level of 2, 4 wt%) has also been synthesized to know the effect of individual elements on the first hydrogenation of TiFe alloy. From the preceding section 4.3, the most effective combination in terms of kinetics and maximum hydrogen capacity was the TiFe alloy with simultaneous addition of 2 wt% Mn and 4 wt% Zr. Simultaneous addition of 2 wt% Zr + 2 wt% Mn + 2 wt% V to TiFe alloy was also done in order to low the concentration level of individual elements as additives. The alloys with only V, Zr +V and Zr + Mn + V are shown in **Table 4.9**. Bulk chemical analysis of each alloy compared with the nominal composition for each alloy.

**Table 4.9: Bulk chemical analysis: nominal and as measured by XRF (X-ray fluorescence) spectrometer of all alloys. Uncertainty on all values is  $\pm 1$  at%**

Alloy		Ti (at. %)	Fe (at. %)	Zr (at. %)	V (at. %)	Mn (at. %)
<b>Heat#8</b> (TiFe+ 2 wt% V)	Nominal composition	49	49		2	
	Measurement	49	48		2	
<b>Heat#9</b> (TiFe+ 4 wt% V)	Nominal composition	48	48		4	
	Measurement	49	47		4	
<b>Heat#25</b> (TiFe+ 2 wt% Zr + 2 wt% V)	Nominal composition	48	48	1	2	
	Measurement	54	43	1	2	
<b>Heat#26</b> (TiFe+ 2 wt% Zr + 2 wt% Mn + 2 wt% V)	Nominal composition	48	47	1	2	2
	Measurement	53	41	1	2	2

It could be seen that bulk composition is close to nominal one, however, for alloy with 2 wt% Zr + 2 wt% V and alloy with 2 wt% Zr + 2 wt% Mn + 2 wt% V have more atomic percentages of Ti and low in Fe than the nominal values.

#### 4.4.1 Result and discussion

##### 4.4.1.1. Morphology

Back-scattered electron micrographs of TiFe alloy with only V (2, 4 wt%), 2 wt% Zr + 2 wt% V and 2 wt% Zr + 2 wt% V + 2 wt% Mn as additives are shown in **Figure 4.12**. Micrograph of these alloys mostly consists of a grey phase (TiFe) and secondary phases (light grey, bright, dark grey). TiFe alloy having 2 wt%, 4 wt% V have a minimum amount of secondary phase. Addition of 2 wt% Zr and 2 wt% V simultaneously to TiFe alloy produces a very fine distribution of secondary phase compared to alloys having 2, 4 wt% V only. When 2 wt% of Zr, 2 wt% of V and 2 wt% of Mn are simultaneously added to TiFe alloy, there is no significant improvement in the amount of secondary phase compared to alloy having 2 wt% Zr + 2 wt% V.

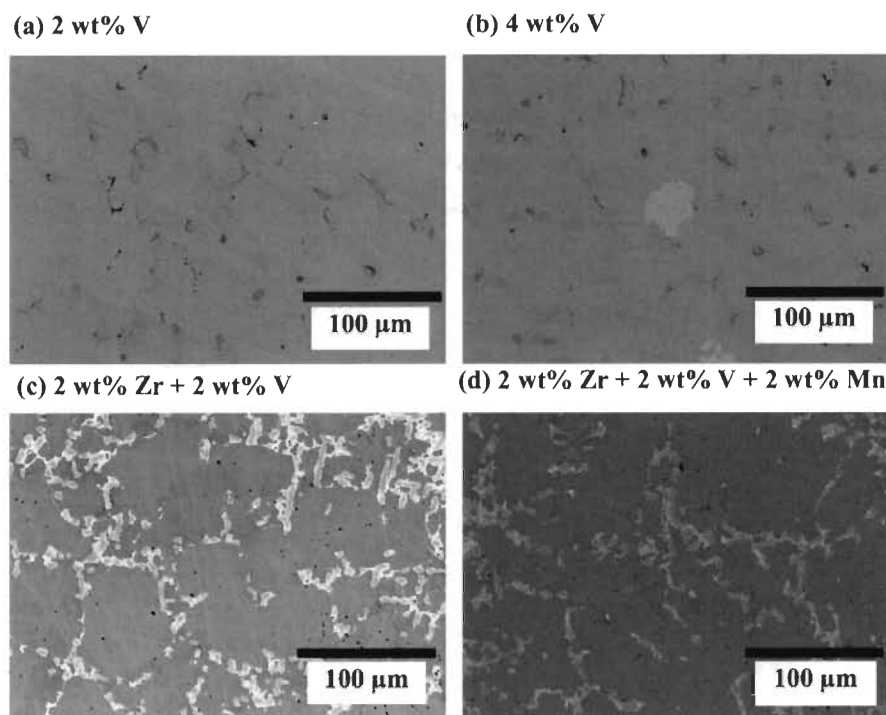


**Figure 4.12:** Back-scattered electron micrograph of TiFe alloy with (a) 2 wt% V, (b) 4 wt% V, (c) 2 wt% Zr + 2 wt% V and (d) 2 wt% Zr + 2 wt% V + 2 wt% Mn as additives

EDX analysis of TiFe alloys with V are shown in **Figure 4.13**. For TiFe with the addition of V only (2 and 4 wt% V), the chemical composition of each phase is presented in **Table 4.10**. In both alloys, there are three phases present; (1) grey phase (TiFe) (2) dark grey phase (3) light grey phase. Grey phase is TiFe enriched with vanadium. In both alloys, the light grey phase has an almost  $\text{Ti}_2\text{Fe}$  composition with a small amount of vanadium. The dark grey phase is Ti-rich. In the case of 4 wt% V, there is one bright phase which has a composition close to  $\text{TiFe}_2$ .

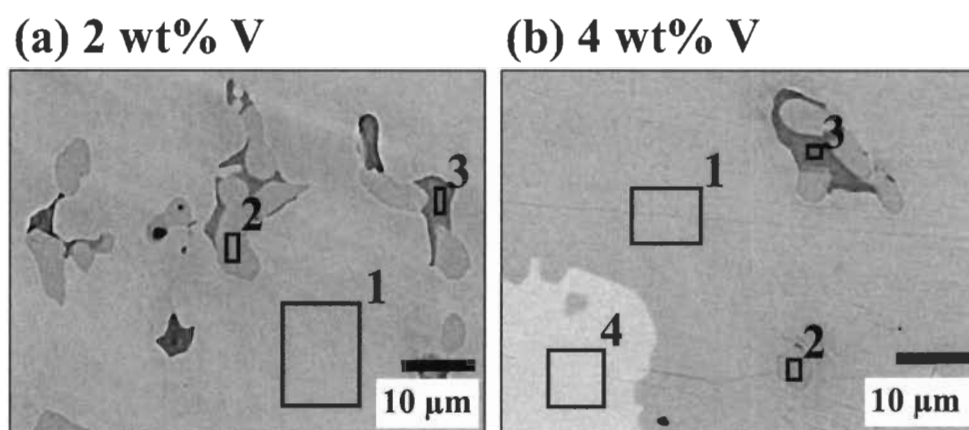


**Figure 4. 13: EDX analysis of TiFe with the addition of V only(a) 2 wt% V and (b) 4 wt% V**

**Table 4.10: Chemical composition of each phase present in alloys with V only (uncertainty on all values is  $\pm 1$ )**

Alloys	Ti (at. %)	Fe (at. %)	V (at. %)
<b>TiFe + 2 wt% V</b>			
<i>Area 1 (grey phase)</i>	49	48	3
<i>Area 2 (light grey phase)</i>	61	34	6
<i>Area 3 (dark grey phase)</i>	72	21	7
<b>TiFe + 4 wt% V</b>			
<i>Area 1 (grey phase)</i>	48	49	4
<i>Area 2 (light grey phase)</i>	58	34	8
<i>Area 3 (dark grey phase)</i>	67	22	11
<i>Area t 4 (bright phase, <math>\text{TiFe}_2</math>)</i>	38	56	6

The area analysis of alloy with the addition of 2 wt% Zr + 2 wt% V simultaneously is shown in **Figure 4.14**. It could be seen that TiFe alloy with the addition of 2 wt% Zr + 2 wt% V simultaneously has four phases: (1) grey phase (2) light grey phase (3) bright phase and (4) dark grey phase. The chemical composition of each phase is shown in **Table 4.11**. Grey phase has composition of TiFe with ~ 2 at. % of V. Light grey phase has composition of Ti<sub>2</sub>Fe with 3 at. % of Zr and 4 at.% of V. Zr is absent from the TiFe-matrix as it was seen in the case of 2 wt% Zr. Bright phase has almost same composition as found for alloys with Zr + Mn (**Table 4.5**) in previous section. Dark grey phase is Ti-rich as it was seen for the alloy having 2 and 4 wt% of V only.

### 2 wt% Zr + 2 wt% V

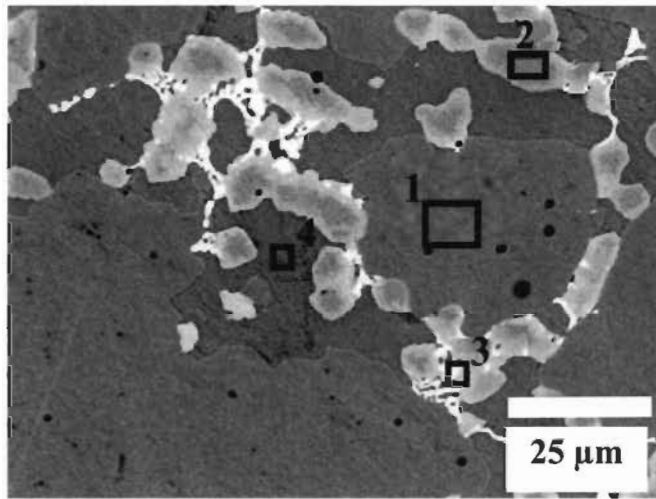


**Figure 4.14:** EDX analysis of TiFe with the simultaneous addition of 2 wt% Zr + 2 wt% V

**Table 4.11:** Chemical composition of each phase present in TiFe with the simultaneous addition of 2 wt% Zr + 2 wt% V (uncertainty on all values is ± 1)

Alloy	Ti (at. %)	Fe (at. %)	V (at. %)	Zr (at. %)
<b>TiFe + 2 wt% Zr + 2 wt% V</b>				
<i>Area 1 (grey phase)</i>	50	48	2	
<i>Area 2 (light grey phase)</i>	61	33	4	3
<i>Area 3 (bright phase)</i>	54	29	4	14
<i>Area 4 (dark grey phase)</i>	72	22	5	2

The chemical composition of each phase present in alloy with the simultaneous addition of 2 wt% Zr + 2 wt% V + 2 wt% Mn was determined by EDX analysis as shown in **Figure 4.15** and reported in **Table 4.12**. Grey phase is TiFe with 2 at. % of Mn and V. Zr is almost absent in the grey phase. Light and bright phases have compositions close to Ti<sub>2</sub>Fe, where Zr substitute for Ti. Light grey phase has almost ½ concentration of Zr present in bright phase as it was found in the case of alloy with the simultaneous addition of 2 wt% Mn and 4 wt% Zr. Dark grey is found to be Ti-rich as it was seen for alloys with only V and alloy with the combination of 2 wt% Zr + 2 wt% V.

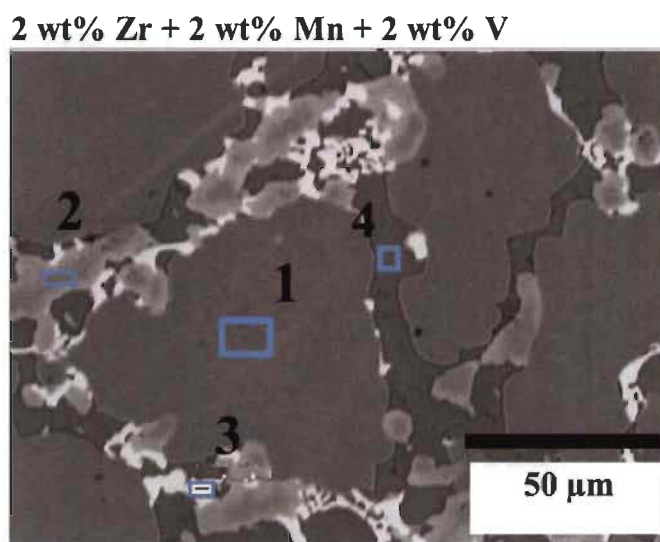


**Figure 4.15:** EDX analysis of TiFe alloy with the simultaneous addition of 2 wt% Zr + 2 wt% V + 2 wt% Mn

**Table 4.12:** Chemical composition of TiFe + 2 wt% Zr + 2 wt% V + 2 wt% Mn (uncertainty on all values is ± 1)

Alloy	Ti (at. %)	Fe (at. %)	V (at. %)	Zr (at. %)	Mn (at. %)
<b>TiFe + 2 wt% Zr + 2 wt%</b>					
<b>V + 2 wt% Mn</b>					
<i>Area 1 (grey phase)</i>	50	47	2	< 1	2
<i>Area 2 (light grey phase)</i>	57	32	3	7	2
<i>Area 3 (bright phase)</i>	45	33	5	14	3
<i>Area 4 (dark grey phase)</i>	78	17	5	3	2

#### 4.4.1.2. Structural characterization

The X-ray diffraction (XRD) pattern of each alloy is shown in **Figure 4.16**. It consists of major peaks of TiFe (space group Pm-3m) phase with minor peaks of TiFe<sub>2</sub> type (space group P6<sub>3</sub>/mmc), Ti<sub>2</sub>Fe type (space group Fd-3m) and Ti (space group P6<sub>3</sub>/mmc) phases. X-ray pattern of alloys with vanadium only has quite limited minor peaks of TiFe<sub>2</sub> phase along with TiFe phase. This result is also evidenced by the chemical composition analysis of alloys with V only as shown in **Table 4.10**. In the EDX result of alloy with 4 wt% V only, three secondary phases (Ti<sub>2</sub>Fe, TiFe<sub>2</sub> and Ti) were seen. While, in XRD results of alloys with V only (2, 4 wt%), only the minor peaks of TiFe<sub>2</sub> phase could be seen.

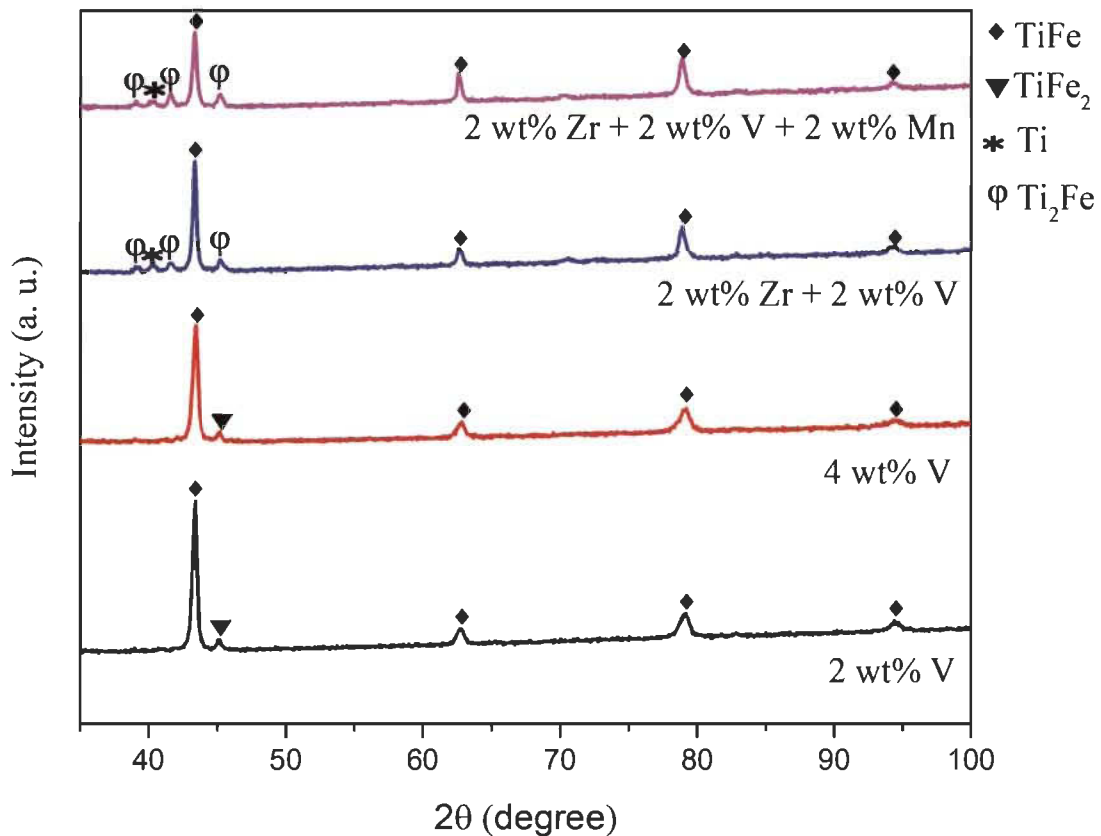
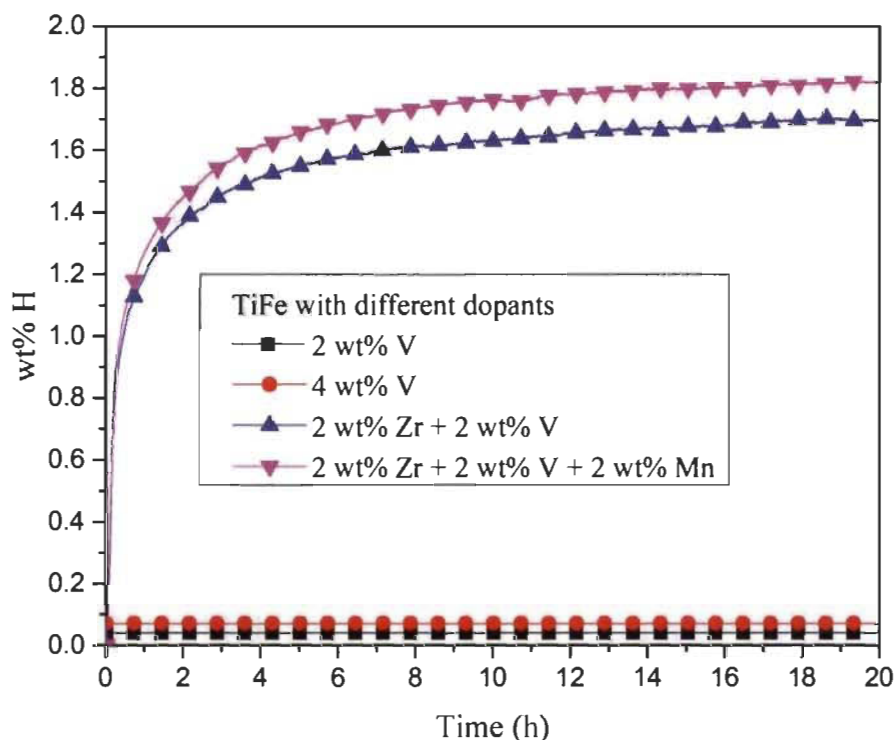


Figure 4.16: X-ray pattern of TiFe alloys with the addition of V only, Zr + V, and Zr + V + Mn

The main reason responsible for this is that addition of V does not produce enough secondary phase so that it could be detected by XRD, as it was seen in the micrograph of TiFe alloy with V. Addition of combination of Zr + V at concentration level of 2 wt% each results in the formation of TiFe<sub>2</sub> Ti<sub>2</sub>Fe and Ti phases along with TiFe phase. These phases were also seen in the chemical composition analysis of TiFe + 2 wt% Zr + 2 wt% V. Similar kind of minor peaks related to these secondary phases were also observed for the alloy with 2 wt% Zr + 2 wt% V + 2 wt% Mn.

#### 4.4.1.3. Activation kinetics

First hydrogenation (activation) curves of TiFe alloys with 2, 4 wt% V only, 2 wt% Zr + 2 wt% V and 2 wt% Zr + 2 wt% V + 2 wt% Mn as additives are shown in **Figure 4.17**. It was observed that addition of only V is not beneficial for the activation of TiFe alloy. The reason could be the presence of TiFe<sub>2</sub> phase, which is a non-hydrating phase and also minimum production of secondary phases compared to other alloys.



**Figure 4.17: Activation kinetics of TiFe alloy with V, Zr + V and Zr + V + Mn under 20 bar H<sub>2</sub> pressure at room temperature**

Combination of 2 wt% Zr + 2 wt% V leads to good kinetics and reaches its maximum hydrogen capacity (1.6 wt%) in 6 hours. Previously, we saw that alloy with 2 wt% Zr only, alloy with 2 wt% V only do not activate. However, simultaneous addition of these two elements at the same concentration level (2 wt%) improves the first hydrogenation kinetics and also maximum hydrogen capacity. In this way, concentration level of additives could be reduced and TiFe alloy could be activated with improved kinetics at minimum amount of these elements. TiFe alloy with the simultaneous addition of 2 wt% Zr + 2 wt% V + 2 wt% Mn has better kinetics and also higher hydrogen capacity (1.8 wt%) than the alloy with 2 wt% Zr + 2 wt% V. In the case of alloy with 2 wt% Zr + 2 wt% V and alloy with 2 wt% Zr + 2 wt% V + 2 wt% Mn, the main cause of the improvement in kinetics and good hydrogen capacity is probably the presence of  $\text{TiFe}_2$  and Ti phases.

#### 4.4.1.4 Rate limiting step of first hydrogenation

Rate limiting step has been determined for the activated alloys by linear fitting of different kinetic models (Table 4.7). The same procedure was followed for linear regression as mentioned in section 4.3.1.4. The linear fitting for the different kinetic models for the TiFe alloy having 2 wt% + 2 wt% V and 2 wt% Zr + 2 wt% V + 2 wt% Mn could be seen in Figure 4.18. The best linear fitted model was found to be GB3D model for each activated alloy. The goodness of linear fitting was confirmed by the adjusted  $R^2$  value for the different kinetic model shown in Table 4.13. The adjusted  $R^2$  value for GB3D model is closer to 1 compared to other kinetic model's adjusted  $R^2$  values.

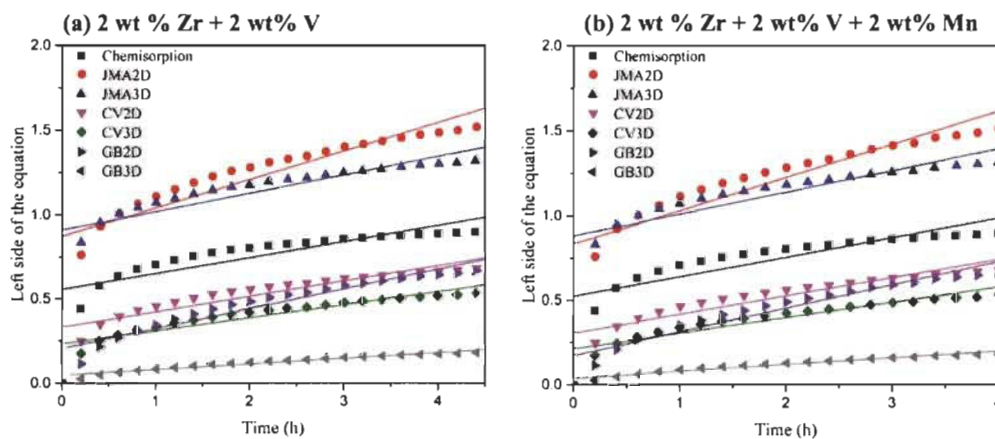


Figure 4.18: Linear fitting of each rate limiting step model for each activated alloy



**Table 4.13: Adjusted R<sup>2</sup> value for the linear regression of different kinetic model**

Adjusted R <sup>2</sup>	Chemisorption	JMA2D	JMA3D	CV2D	CV3D	GB2D	GB3D
<b>2 wt% Zr + 2 wt% V</b>	0.66118	0.79104	0.71276	0.81843	0.86115	0.91201	<b>0.94241</b>
<b>2 wt% Zr + 2 wt% V + 2 wt% Mn</b>	0.67025	0.79372	0.71706	0.81798	0.85985	0.91738	<b>0.94235</b>

#### 4.4.2 Summary

Microstructure and hydrogen storage properties of TiFe with addition of V only, combination of Zr + V and combination of Zr + V + Mn were studied. It was found that addition of V at concentration level of 2 and 4 wt% do not activate the TiFe alloy. However, simultaneous addition of 2 wt% Zr + 2 wt% V improved the kinetics and also the maximum hydrogen capacity (1.6 wt%). This result will be beneficial in terms of minimizing the concentration level of elements as additives. Simultaneous addition of 2 wt% Zr + 2 wt% V + 2 wt% Mn to TiFe alloy leads to the improvement in kinetics and also the maximum hydrogen capacity (1.8 wt%). The main reason for activation of alloys with 2 wt% Zr + 2 wt% V and 2 wt% Zr + 2 wt% V + 2 wt% Mn was the presence of Ti-rich phases (Ti<sub>2</sub>Fe, Ti). The rate limiting step for each activated alloy was found to be a three-dimensional growth, where diffusion controlled with decreasing interface velocity.

## 4.5 TiFe alloy with Mn + V as additives

In this section, simultaneous addition of Mn and V at different concentration level to TiFe alloy is reported. A comparison of bulk measured atomic abundance with the nominal composition of each alloy with the combination of Mn and V is shown in **Table 4.14**. The bulk measured composition is close to the nominal one. However, a higher concentration of Ti than nominal values could be seen. In earlier sections of chapter 4, TiFe alloy with Mn only and V only was reported. We saw that 1 wt% Mn was enough to activate the TiFe alloy. However, the addition of V only at a concentration level of 2 and 4 wt% do not have any effect on the activation curve of TiFe alloy. Therefore, combination of Mn and V has been studied in order to have a possible synergy effect and compare it with the microstructure of alloys studied in previous chapters.

**Table 4.14: Bulk chemical analysis: nominal and as measured by XRF (X-ray fluorescence) spectrometer of all alloys. Uncertainty on all values is  $\pm 1$  at. %**

Alloy		Ti (at. %)	Fe (at. %)	V (at. %)	Mn (at. %)
<b>Heat#12</b> (TiFe+ 2 wt% Mn + 1 wt% V)	Nominal composition	49	49	1	2
	Measurement	52	45	< 1	2
<b>Heat#3</b> (TiFe+ 2 wt% Mn + 2 wt% V)	Nominal composition	48	48	2	2
	Measurement	54	43	2	2
<b>Heat#4</b> (TiFe+ 2 wt% Mn + 4 wt% V)	Nominal composition	47	47	4	2
	Measurement	53	42	4	2
<b>Heat#15</b> (TiFe+ 4 wt% Mn + 4 wt% V)	Nominal composition	46	46	4	4
	Measurement	52	42	3	4

### 4.5.1 Result and discussion

#### 4.5.1.1. Morphology

Back-scattered micrographs of all samples are shown in **Figure 4.19**. There are three kinds of phases that could be seen: a grey phase, a light grey phase, and a dark grey phase. Grey phase represents the TiFe matrix. Light grey phase is mainly Ti-rich and dark grey phase is enriched in V and Ti. When V content was 1 wt% along with 2 wt% Mn, there was no light grey phase and dark grey phase area was very small compared to other alloys. When V content is getting higher

from 2 to 4 wt%, fine distribution of dark grey phase and light grey phase could be seen. The chemical composition of each phase was identified by EDX analysis. The area analysis of all alloys is shown in **Figure 4.20**. A clear difference in the dark grey and light grey phase could be seen.

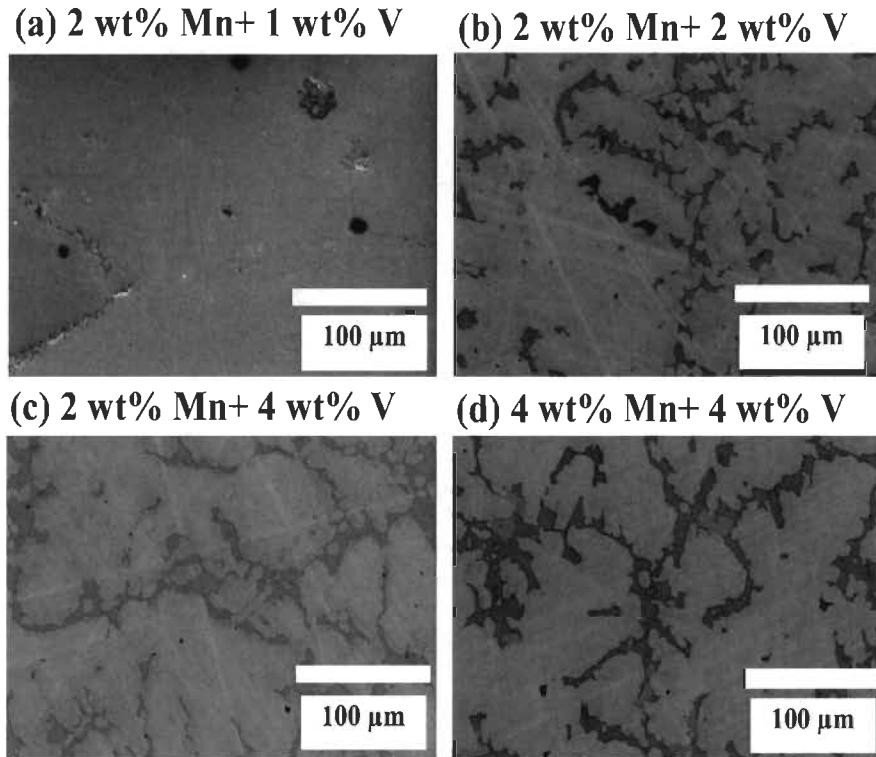


**Figure 4.19:** Back-scattered micrograph of TiFe alloy with (a) 2 wt% Mn + 1 wt% V, (b) 2 wt% Mn + 2 wt% V, (c) 2 wt% Mn + 4 wt% V and (d) 4 wt% Mn + 4 wt% V as additives

Area 1 indicates the grey phase, which is TiFe and its composition is shown in **Table 4.15**. As it could be clearly seen that some part of the Fe is substituted by V and Mn in each alloy. Area 2 indicates the dark grey phase. The chemical composition of the dark grey phase in each alloy is shown in **Table 4.16**. It could be seen that dark grey phase is Ti-rich.

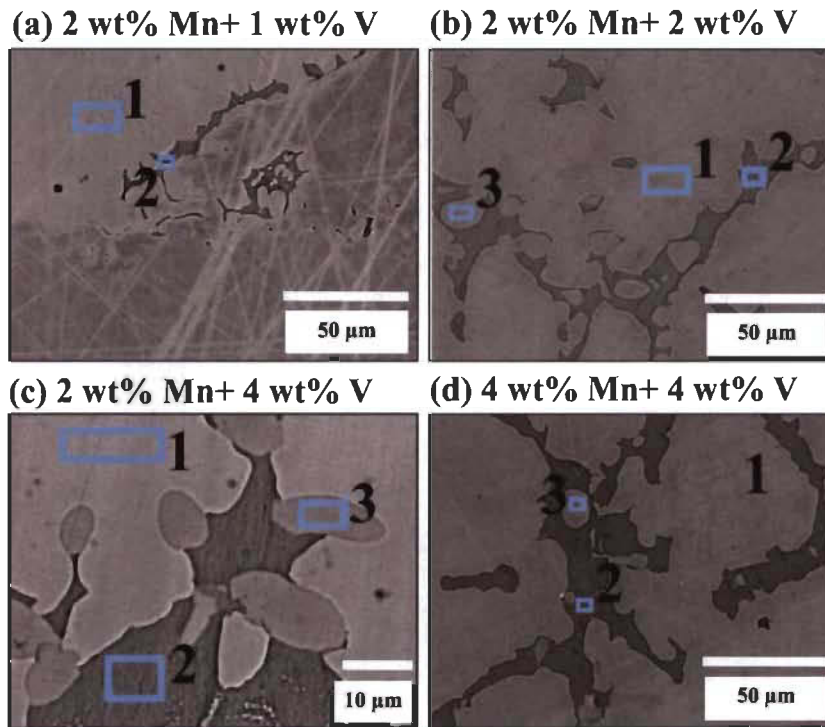


Figure 4.20: EDX analysis of TiFe alloy with the combination of (a) 2wt% Mn + 1 wt% V, (b) 2 wt% Mn + 2 wt% V, (c) 2 wt% Mn + 4 wt% V and (d) 4 wt% Mn + 4 wt% V as additives

Table 4.15: Chemical composition of area 1 (Grey phase) in all alloys (uncertainty on all values is  $\pm 1$ )

(Area 1) Alloy	Ti (at. %)	Fe (at. %)	V (at. %)	Mn (at. %)
2 wt% Mn+ 1 wt% V	51	45	< 1	3
2 wt% Mn+ 2 wt% V	51	46	2	2
2 wt% Mn+ 4 wt% V	49	44	4	2
4 wt% Mn+ 4 wt% V	50	45	3	3

Light grey phase has been indicated by area 3 and its composition is shown in **Table 4.17**. Light grey phase has a composition close to  $Ti_2Fe$ . This light grey phase is not present in alloy having 2 wt% Mn and 1 wt% V. In each alloy, light grey phase has almost same concentration of Mn.

**Table 4.16: Chemical composition of area 2 (dark grey phase) in all alloys (uncertainty on all values is  $\pm 1$ )**

(Area 2)	Ti (at. %)	Fe (at. %)	V (at. %)	Mn (at. %)
Alloy				
2 wt% Mn+ 1 wt% V	79	16	3	<1
2 wt% Mn+ 2 wt% V	74	19	4	<1
2 wt% Mn+ 4 wt% V	68	23	7	<1
4 wt% Mn+ 4 wt% V	69	23	7	1

**Table 4.17: Chemical composition of area 3 (light grey phase) in all alloys (uncertainty on all values is  $\pm 1$ )**

(Area 3)	Ti (at. %)	Fe (at. %)	V (at. %)	Mn (at. %)
Alloy				
2 wt% Mn+ 1 wt% V	--	--	--	--
2 wt% Mn+ 2 wt% V	62	33	4	<1
2 wt% Mn+ 4 wt% V	59	33	6	<1
4 wt% Mn+ 4 wt% V	61	32	6	1

#### 4.5.1.2. Structural characterization

The X-ray diffraction (XRD) pattern of each alloy is shown in **Figure 4.21**. Major peaks of TiFe (space group Pm-3m) phase with minor peaks of Ti<sub>2</sub>Fe type (space group Fd-3m) and Ti (space group P6<sub>3</sub>/mmc) phases could be seen. Alloys with 2 wt% Mn + 2 wt% V, 2 wt% Mn + 4 wt% V and 4 wt% Mn + 4 wt% V have Ti and Ti<sub>2</sub>Fe secondary phases along with TiFe phase, which is also seen in the chemical composition analysis of these alloys. Alloy with 2 wt% Mn + 1 wt% V has only Ti secondary phase along with TiFe phase. The appearance of only Ti secondary phase along with TiFe phase could be also evidenced by the chemical composition analysis of alloy with 2 wt% Mn + 1 wt% V.

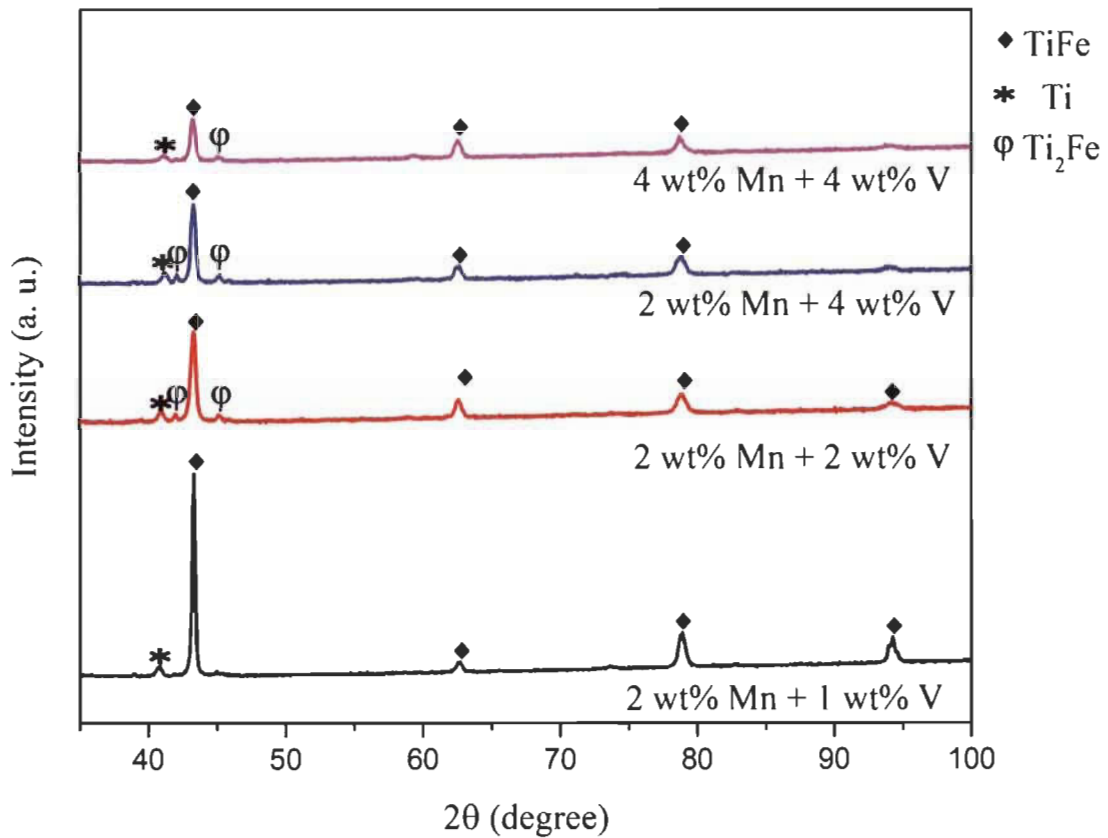
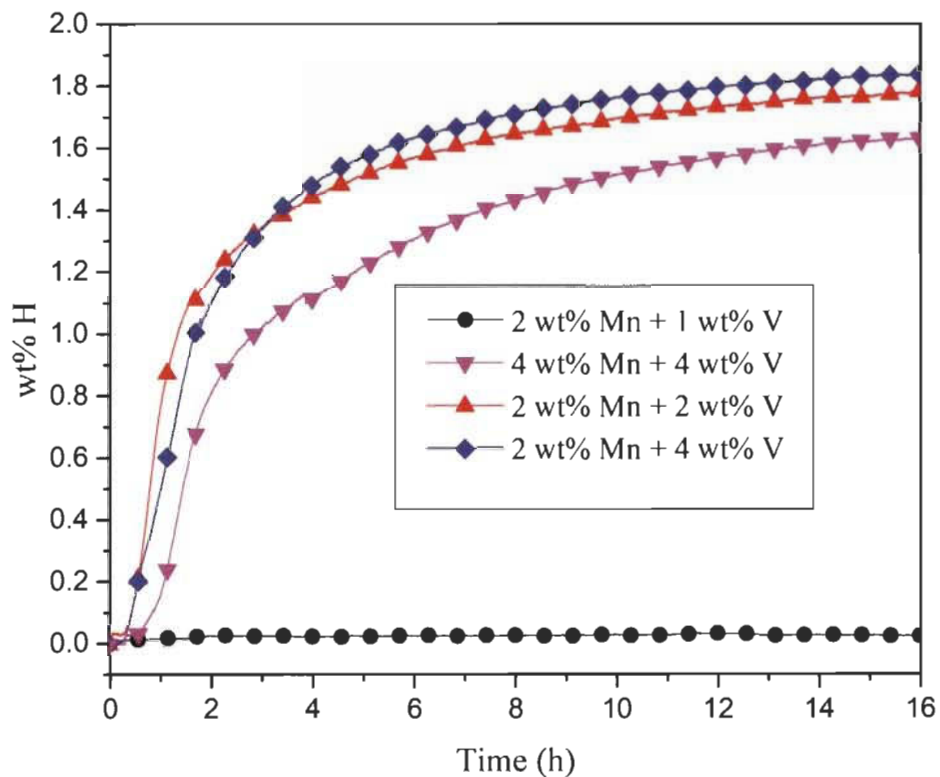


Figure 4.21: X-ray pattern of TiFe alloys with the combination of Mn + V as additives

### 4.5.1.3 Activation kinetics

First hydrogenation curves of all samples are shown in **Figure 4.22**. From this graph, it could be clearly seen that addition of 1 wt% V alongside with 2 wt% Mn is not enough to activate the TiFe alloy. The cause of no activation is the lower phase abundance of secondary phase. The addition of 2 wt% V with 2 wt% Mn leads to fast kinetics and its maximum hydrogen capacity is  $\sim 1.78$  wt%. By increasing the proportion of V up to 4 wt% and keeping the Mn concentration constant at 2 wt%, maximum hydrogen capacity could be increased up to 1.8 wt%, however, it has almost same kinetics as for the alloy having 2 wt% Mn and 2 wt% V. Combination of 4 wt% Mn and 4 wt% V retards the kinetics and maximum hydrogen capacity. The main cause of activation for these alloys could be the presence of Ti,  $Ti_2Fe$  phases.



**Figure 4.22: First hydrogenation curve of TiFe alloys with the combination of Mn + V as additives at room temperature and 20 bar hydrogen pressure**

#### 4.4.1.4 Rate limiting step of first hydrogenation

Rate limiting step was determined by the plotting the different kinetic models and performing the linear regression on each kinetic model curve. The linear regression of each kinetic model curve is shown in **Figure 4.23** and the best fitted curve could be seen for the GB3D model. Adjusted  $R^2$  value has given in **Table 4.18** for the confirmation of best fitted curve. The adjusted  $R^2$  value for GB3D model is closer to 1 than for the other kinetic models.

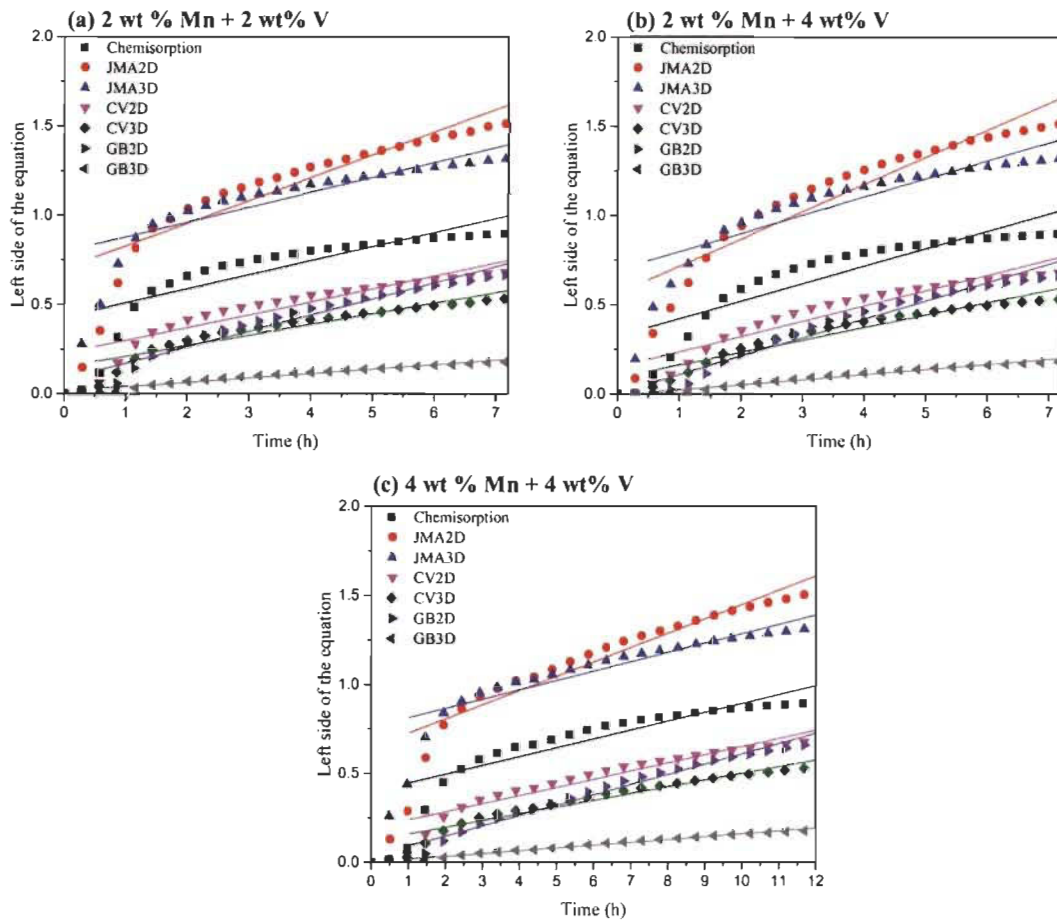


Figure 4.23: Linear regression of different kinetic model for each TiFe alloy with the combination of Mn and V as additives



**Table 4.18: Adjusted R<sup>2</sup> value for linear fitting of different kinetic model**

Adjusted R <sup>2</sup>	Chemisorption	JMA2D	JMA3D	CV2D	CV3D	GB2D	GB3D
<b>2 wt % Mn + 2 wt% V</b>	0.7341	0.85138	0.80277	0.85764	0.89266	0.93785	<b>0.95933</b>
<b>2 wt % Mn + 4 wt% V</b>	0.79722	0.89003	0.85047	0.89547	0.9232	0.95721	<b>0.97333</b>
<b>4 wt % Mn + 4 wt% V</b>	0.82321	0.91783	0.88119	0.92221	0.9469	0.97571	<b>0.98751</b>

#### 4.5.2 Summary

Microstructure, structural characterization and first hydrogenation kinetics with rate limiting step for TiFe with the combination of Mn and V were investigated. It was found that activation kinetics and maximum hydrogen capacity could be enhanced by a combination of Mn and V. Maximum hydrogen capacity ~ 1.8 wt% could be achieved at room temperature under 20 bar hydrogen pressure by the addition of Mn and V simultaneously at minimum concentration level of 2 wt% V and 2 wt% Mn. Similar to the compositions reported in the previous chapters, the cause for the activation was found to be the presence of Ti, Ti<sub>2</sub>Fe secondary phases. In rate limiting step determination, GB3D model was found to be best linear fitted, which governs the three-dimensional growth of hydride phase with decreasing interface velocity.

## Chapter 5

# Effect of heat treatment on microstructure and hydrogenation properties of TiFe + X wt% Zr (X = 4, 8)

---

### 5.1 Introduction

In the previous chapter, it could be seen that microstructure plays an important role for activation. In this chapter, a systematic investigation of the effect of microstructure on activation kinetics of TiFe alloy is shown by applying heat treatment. This is done by studying TiFe alloy with the addition of 4 and 8 wt% of zirconium. TiFe alloy with Zr additive has been synthesized at laboratory scale using arc melting. Thereafter, heat treatment was performed on each composition of alloy.

### 5.2 Result and discussion

#### 5.2.1 Morphology

The backscatter electron micrograph of all alloys (as-cast and after heat treatment) is shown in **Figure 5.1**. In all micrographs, three different phases could be seen: a bright phase, a grey phase, and some black precipitates.

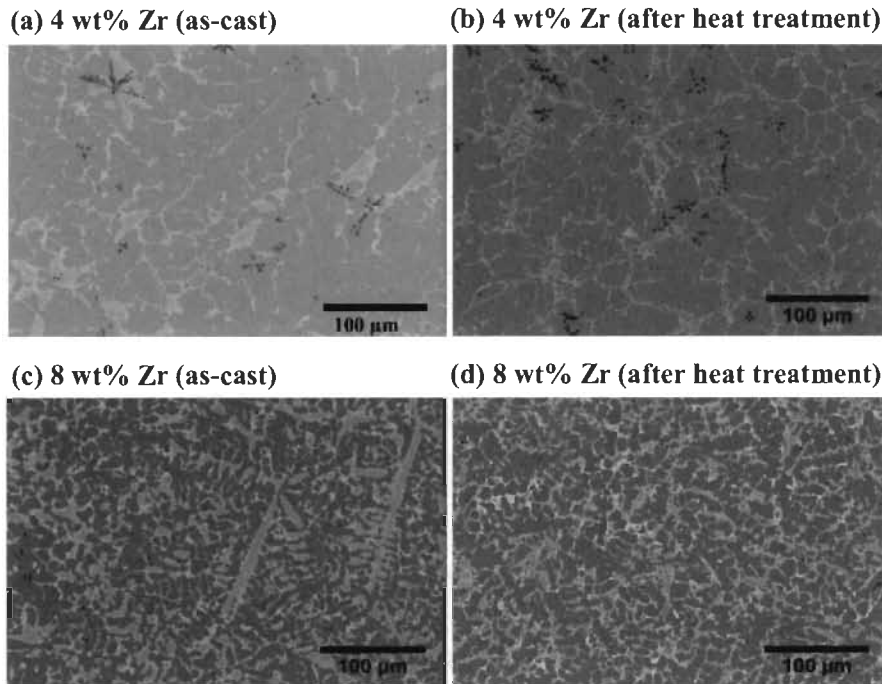


**Figure 5.1: Backscatter electron micrograph of TiFe + X wt% Zr (X= 4, 8) alloys before (a, c) and after heat treatment (b, d)**

It is clear that, as the amount of zirconium increases, the surface area of the bright phase also increases. For each composition, the micrographs become finer after heat treatment. Using ImageJ software, the respective areas of the different phases were evaluated using one randomly selected image at the magnification value of 300. The field of view of this image is sufficient to ensure that it represents the bulk value. Results are reported in **Table 5.1**. It could be seen that the bright phase area increases for increasing Zr content but also that heat treatment had the effect of decreasing the area of the bright phase.

**Table 5.1: Area percentages of different phases for TiFe + X wt% Zr micrographs shown in Figure 4.1. Uncertainty on all values is  $\pm 1$**

Phase	(as-cast)	(after heat treatment)
<b>TiFe + 4 wt% Zr</b>		
Grey (%)	75	86
Bright (Zr – rich) (%)	24	13
Black precipitate (%)	1	1
<b>TiFe + 8 wt% Zr</b>		
Grey (%)	62	75
Bright (Zr – rich) (%)	38	25

Elemental mapping of all alloys is shown in **Figure 5.2**. It shows that Zr is mainly concentrated in the bright phase. It could also be seen that Ti and Fe are both present in the matrix and the bright phase. Black precipitates are mainly Ti-rich. Besides the fact that heat treatment had the effect of slightly reducing the area of secondary phase, we see that heat treatment made the morphology of the secondary phase much more complex. For both compositions, the secondary phase in the heat-treated sample has an intricate structure where some grey phase is embedded inside the bright phase. From ternary phase diagram of Fe-Ti-Zr system at 1173 K, possible phase for 4 and 8 wt% Zr could be TiFe + Fe<sub>2</sub>Ti +  $\alpha$  Fe [108].

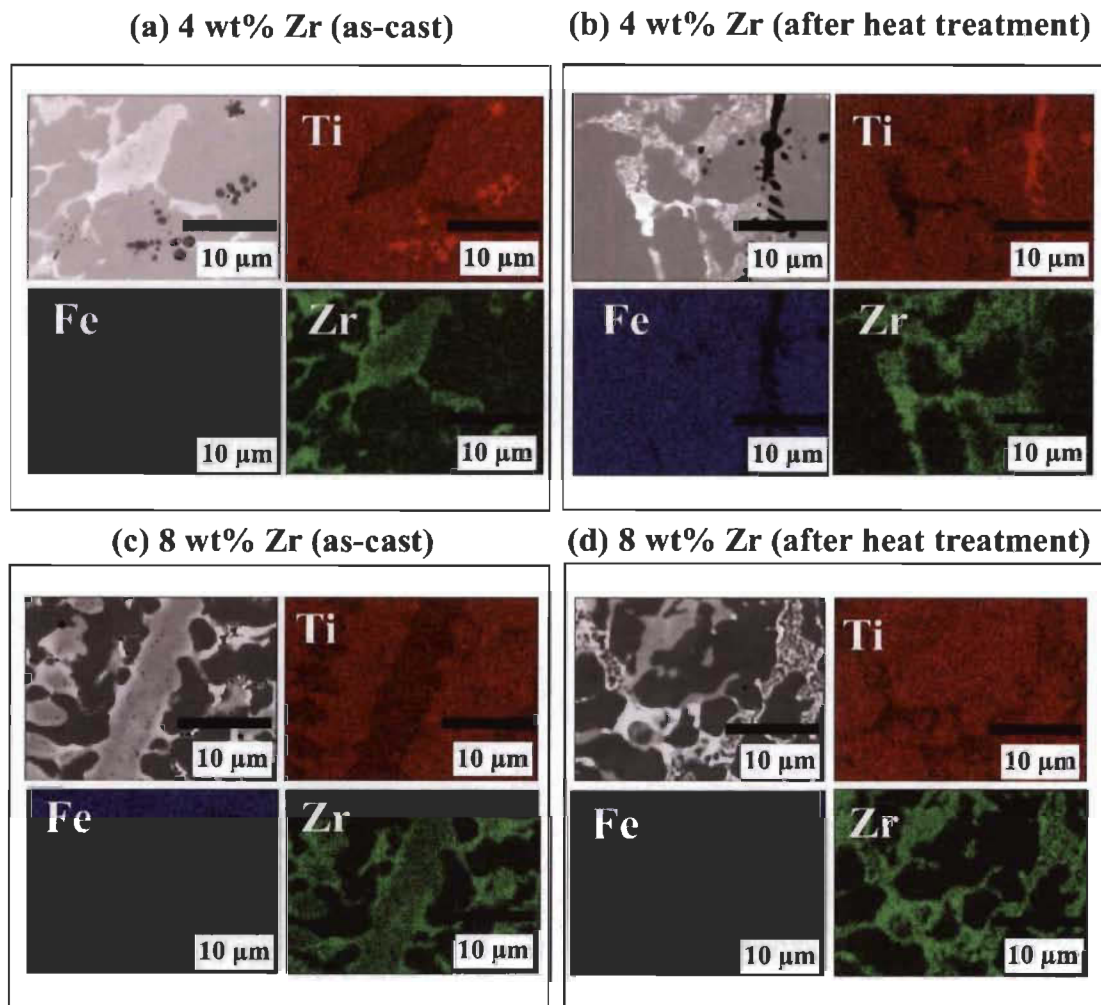


Figure 5.2: Elemental mapping of TiFe + X wt% Zr (X= 4, 8) alloys before (a, c) and after heat treatment (b, d)

In order to know the chemical composition of each phase present in each alloy, EDX measurements were taken.

#### 5.2.1.1 TiFe with 4 wt% Zr (as-cast and heat-treated)

The microstructure before and after heat treatment is shown in **Figure 5.3**. In both micrographs, the grey phase is mainly TiFe and bright phase is Zr-rich. There are also some black precipitates which are Ti-rich.

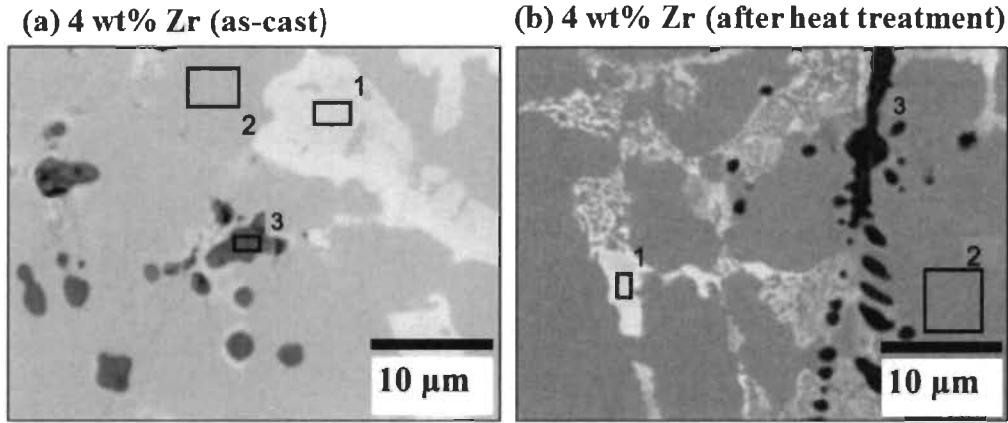


Figure 5.3: EDX analysis of TiFe + 4wt% Zr as-cast (a) and after heat treatment (b)

Chemical composition of the phases shown in **Figure 5.3** as determined by EDX are presented in **Table 5.2**. It could be seen that after heat treatment, the bright phase is getting enriched in Zr. Grey phase has an almost equal atomic concentration of Ti and Fe with a small amount of Zr for as-cast and heat-treated alloys.

**Table 5.2: Chemical compositions of TiFe + 4 wt% Zr in as-cast and heat-treated states.**  
Uncertainty on all values is  $\pm 1$

Alloys	Ti (at. %)	Fe (at. %)	Zr (at. %)
<b>TiFe + 4 wt% Zr (as-cast)</b>			
<i>Bright phase (area 1)</i>	38	55	7
<i>Grey phase (area 2)</i>	49	48	3
<i>Black precipitate (area 3)</i>	97	1	1
<b>TiFe + 4 wt% Zr (heat-treated)</b>			
<i>Bright phase (area 1)</i>	31	47	22
<i>Grey phase (area 2)</i>	50	49	<1
<i>Black precipitate (area 3)</i>	96	2	2

Black precipitates are mostly Ti ( $\sim 97$  at. %) before and after heat treatment. We see that the main result of heat treatment is that zirconium diffuses out of the grey phase (TiFe phase) and enters into the bright phase making the zirconium content higher. The composition of the black precipitates barely changed.

### 5.2.1.2 TiFe with 8 wt% Zr (as-cast and heat-treated)

Microstructure of as-cast and heat-treated alloy having 8 wt% Zr is shown in **Figure 5.4**. Three phases could be seen, grey phase (area 1) which is TiFe, bright phase which is Zr-rich (area 2) and light grey phase which has less Zr content than bright phase (area 3). The chemical composition of these phases was measured by EDX analysis and are presented in **Table 5.3**. After heat treatment, three main observations could be made: (i) the grey phase composition did not significantly change after heat treatment. (ii) bright and light grey phases are getting enriched in Zr. (iii) light grey phase is getting reduced in Fe and enriched in Ti.

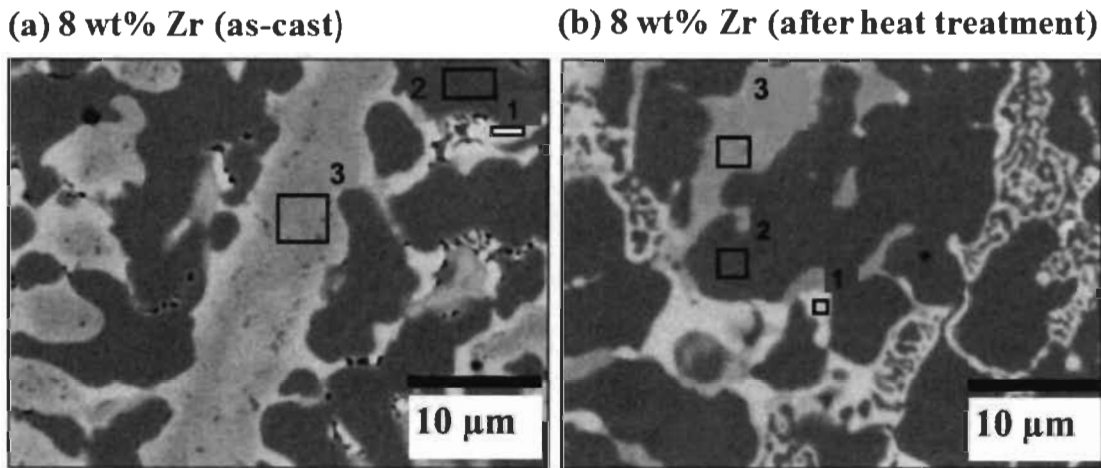


**Figure 5.4:** EDX analysis of TiFe + 8 wt% Zr as cast (a) and after heat treatment (b)

**Table 5.3:** Chemical compositions of TiFe + 8 wt% Zr in as-cast and heat-treated states. Uncertainty on all values is  $\pm 1$

Alloys	Ti (at. %)	Fe (at. %)	Zr (at. %)
<b>TiFe + 8 wt% Zr (as-cast)</b>			
Bright phase (area 1)	43	39	18
Grey phase (area 2)	50	49	<1
Light grey phase (area 3)	39	55	6
<b>TiFe + 8 wt% Zr (heat-treated)</b>			
Bright phase (area 1)	38	37	25
Grey phase (area 2)	50	49	<1
Light grey phase (area 3)	52	32	16

From these analyses for  $X = 4$  and  $8$ , we see that grey phase is TiFe with a very small amount of Zr before and after heat treatment. Thus, the solubility of Zr in TiFe is limited to below 1 at.%. When  $X = 8$ , the bright phase has more Zr content than when  $X = 4$ .

### 5.2.2 Structural characterization

X-ray diffraction patterns of all alloys are shown in **Figure 5.5**. All XRD pattern shows the TiFe phase. Because of the strong fluorescence of iron with Cu-radiation, it is difficult to detect the secondary phases except for the alloy TiFe + 8 wt% Zr after heat treatment. Even for this composition, the peaks are too small, and we were unable to identify the crystal structure. Lattice parameters and crystallite sizes of all alloys as determined by Rietveld refinement are shown in **Table 5.4**. Lattice parameters do not differ very much after heat treatment which confirms the fact that the composition of TiFe phase does not change upon heat treatment. In a similar way, crystallite size does not drastically change upon heat treatment.

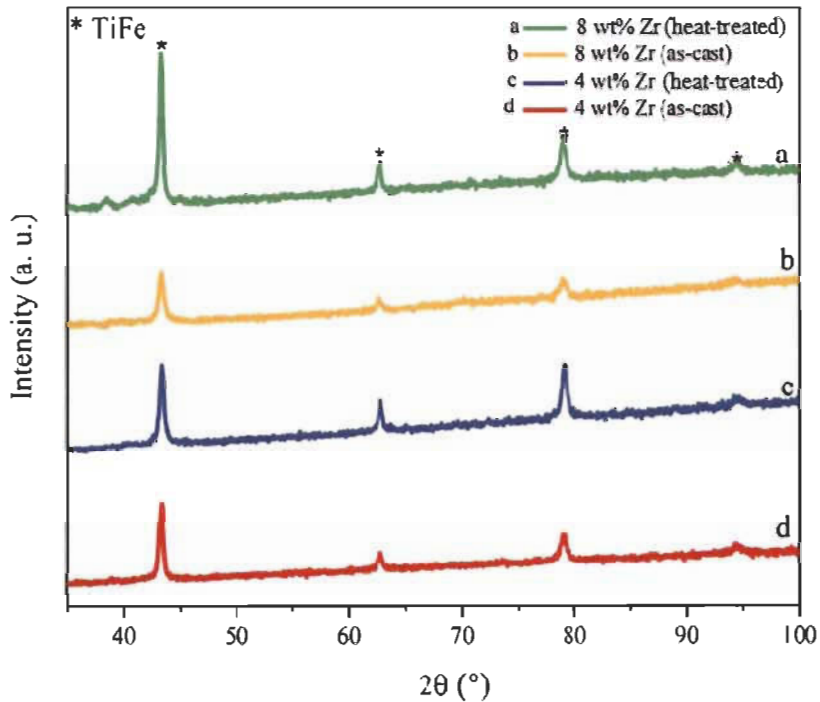


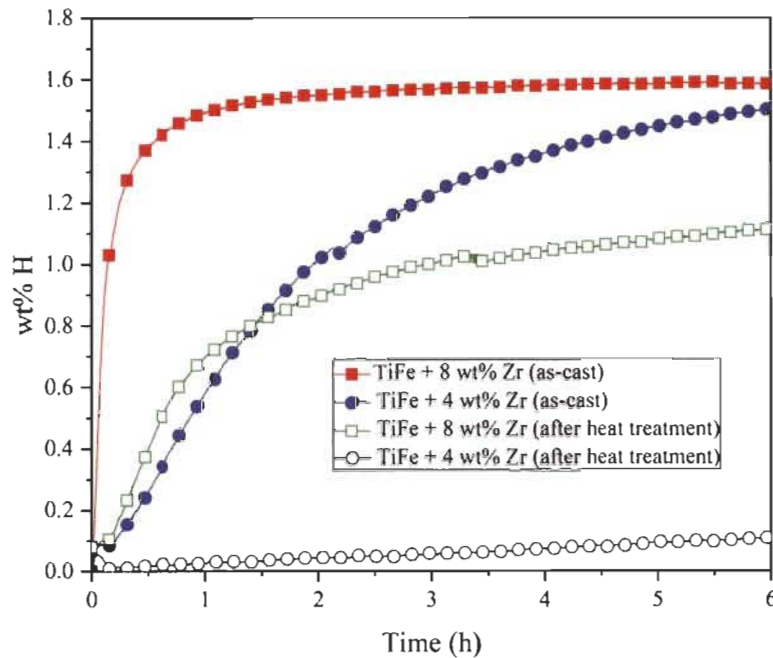
Figure 5.5: X-ray diffraction patterns of TiFe + X wt% Zr ( $X = 4, 8$ ) as-cast and heat-treated at 1173 K

**Table 5.4: Lattice parameter and crystallite size of all alloys**

Alloys	Lattice Parameter (Å)	Crystallite size (nm)
TiFe + 4 wt% Zr (As-cast)	2.9819(4)	19.0(4)
TiFe + 4 wt% Zr (heat-treated)	2.9813(3)	17.1(4)
TiFe + 8 wt% Zr (As-cast)	2.9859(8)	13.2(4)
TiFe + 8 wt% Zr (heat-treated)	2.9832(4)	20.6(4)

### 5.2.3 Activation kinetics

First hydrogenation curve of all samples was measured at room temperature under 2 MPa of hydrogen pressure. First hydrogenation curves of TiFe + X wt% Zr (X = 4, 8) before and after heat treatment are shown in **Figure 5.6**. For X = 4, the as-cast sample readily absorbs hydrogen and reaches a capacity of around 1.6 wt% in about 6 hours. The effect of heat treatment is greatly detrimental; the heat-treated TiFe + 4 wt% Zr sample could barely absorb 0.1 wt% of hydrogen after 6 hours.

**Figure 5.6: First hydrogenation curve of TiFe + X wt% Zr (X = 4, 8) alloys before and after heat treatment**



In the case of  $X = 8$ , the as-cast sample absorbs hydrogen much faster than the as-cast TiFe + 4 wt% Zr. It reaches its maximum hydrogen capacity within two hours. However, as in the previous case, heat treatment had for the effect of strongly reducing the kinetics and hydrogen capacity. After 6 hours the hydrogen capacity is only 1 wt%. Therefore, heat treatment has a detrimental effect on as-cast TiFe alloy with Zr as additive.

The reason for the negative effect of heat treatment is most likely due to the modifications of the secondary phases. Their chemical composition and relative abundance change, mainly by having a higher proportion of zirconium. The fact that the secondary phases change composition upon heat treatment also means that in the as-cast state these phases are in a metastable state. This could greatly influence their behavior under hydrogen exposure.

### **5.3 Summary**

The effect of heat treatment on the microstructure and hydrogen storage characteristics of TiFe + X wt% Zr ( $X = 4, 8$ ) alloys have been investigated. The following results were obtained:

- The main effect of heat treatment was to push out the Zr from the TiFe phase (for  $x = 4$ ) and diffuse it into the secondary phases.
- From the hydrogenation curve, it was concluded that heat treatment reduced the hydrogen capacity and kinetics.

From these results, it was concluded that heat treatment is not suitable for the TiFe alloy with zirconium as additive. The reason is probably that as-cast secondary phases are metastable and thus more sensitive to hydrogen while the heat-treated secondary phases are more zirconium rich and less receptive to hydrogen. Heat treatment had for effect of producing secondary phases that could not absorb hydrogen thus making the total capacity smaller compared to the as-cast alloy.

## Chapter 6

# Effect of cooling rate on the microstructure and hydrogen storage properties of TiFe with 4 wt% Zr as an additive

---

### 6.1 Introduction

From previous investigations, it is known that addition of 4 wt% Zr enhances the activation (first hydrogenation) kinetics of TiFe alloy at laboratory scale [41, 42, 57, 58]. Ti (99.9%, sponge), Fe (99.5%, pieces), Zr (99.5%, sponge) purchased from Alfa Aesar were used as raw materials in these studies. In the previous chapter 4, it could also be seen that 4 wt% Zr enhances the activation kinetics at industrial scale using industrial grade raw material. For industrial scale synthesis, it is important to know the effect of cooling rate on the microstructure and thereby on the hydrogen storage properties. In this investigation, we studied the effect of cooling rate on hydrogen storage properties of TiFe with 4 wt% Zr as an additive. In this way, we could distinguish between the chemical effect of having secondary phases of different compositions and the effect of morphology of the dispersion of the secondary phase. Moreover, this may enable us to see if the cooling rate has some effect on the chemical composition of the secondary phase. In order to be as close as possible to the industrial process, industrial grade raw materials were used instead of laboratory grade elements.

### 6.2 Result and discussion

#### 6.2.1 Morphology

Backscattered micrographs of as-cast TiFe + 4 wt% Zr alloy for different thicknesses of mold representing different cooling rates are shown in **Figure 6.1**. It is clear that the microstructure depends on the cooling rate. For 3 mm thickness, a fine dendritic structure is clearly seen. This dendritic structure gets coarser at each step starting with a dendritic arm spacing (DAS) of only a few microns to close to 50 microns at the biggest step. This is directly linked to the different cooling rate, i.e.: higher heat extraction leads to smaller dendrites formation. It could be seen that, in each micrograph, three different phases are present; (1) grey phase (2) light grey phase and (3) bright phase (at the edge of light grey phase).

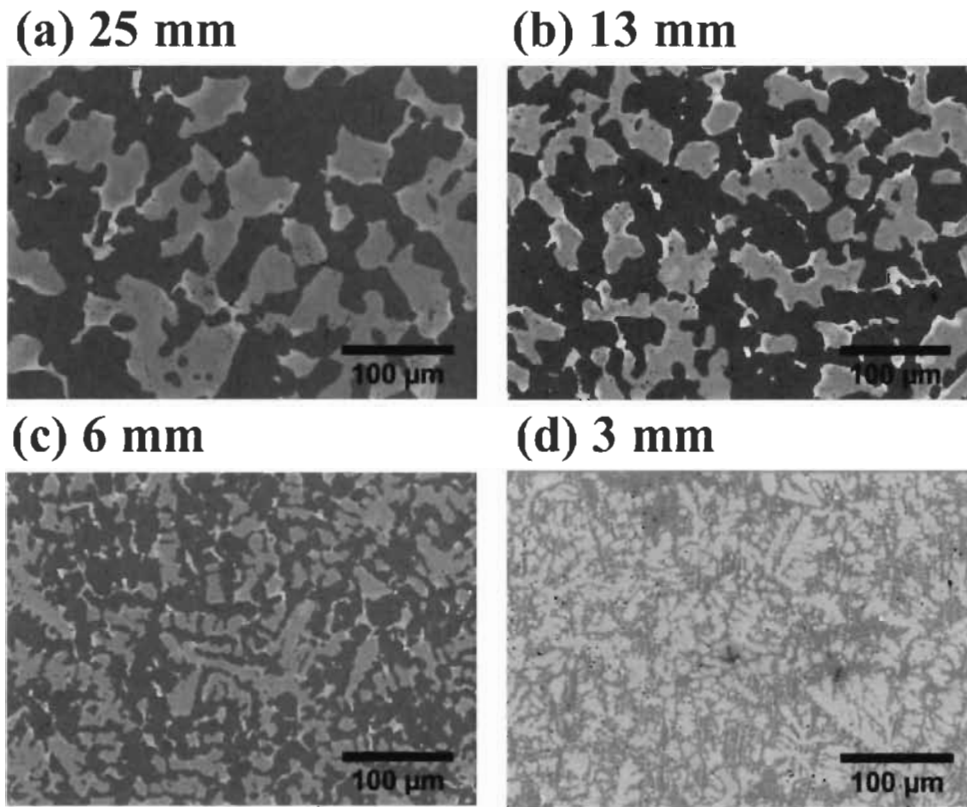


**Figure 6.1: Backscattered micrographs of TiFe + 4 wt% Zr at different step mold thickness (a) 25 mm, (b) 13 mm, (c) 6 mm and (d) 3 mm**

For the same area covered by the secondary phase, a smaller dendritic structure has more interface with the main phase than a bigger structure. For all samples, the perimeters of the secondary phase over the total area of micrograph were evaluated using the 100  $\mu\text{m}$  scale micrographs. Results are reported in **Table 6.1** and clearly show that the perimeter of the secondary phase increases with increasing cooling rates. Area fraction of grey, light grey, and bright phases has also been calculated by ImageJ and are shown in **Table 6.1**. The grey phase area fraction is constant except for the 3 mm thickness.

**Table 6.1: Perimeter of the secondary phase over the total area of micrograph as calculated by ImageJ software**

Thickness (mm)	Perimeter ( $\mu\text{m}/\mu\text{m}^2$ )	Grey phase area (%)	Light grey + bright phase area (%)
25	$3.6 \pm 0.4$	$60 \pm 1$	$40 \pm 1$
13	$6.1 \pm 0.6$	$63 \pm 1$	$37 \pm 1$
6	$10 \pm 1$	$65 \pm 1$	$35 \pm 1$
3	$25 \pm 3$	$50 \pm 1$	$50 \pm 1$

The phase's chemical compositions were measured by EDX. The EDX analysis and mapping of 25 mm thickness sample are shown in **Figure 6.2**. Areas 1, 2 and 3 respectively represent the grey, light grey, and bright phases. From mapping, it could be seen that Ti is abundant in the grey phase but deficient in light grey and bright phases. Iron (Fe) is evenly distributed through all phases but Zr is mainly concentrated in light grey and bright phases. Identical phases and similar distribution of elements were seen for the 13, 6, and 3 mm thicknesses as in the case of 25 mm thickness.

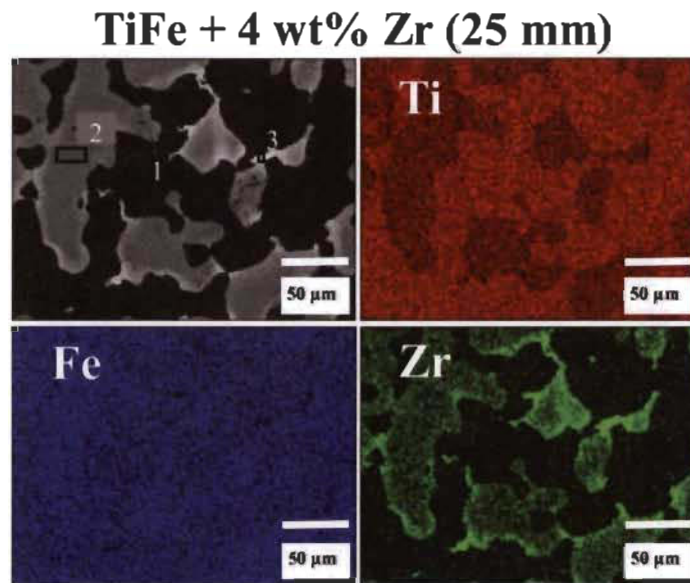


**Figure 6.2: EDX analysis with mapping of an alloy having a 25 mm thickness of step mold**

Chemical compositions of grey phase in each thickness are shown in **Table 6.2**. Grey phase has an almost equal atomic concentration of Fe and Ti with a small amount of Zr. Atomic percentages of Ti, Fe, and Zr are essentially the same for the different cooling rate and it is clear that this phase is TiFe alloy.

**Table 6.2: Chemical composition of grey phase (Area 1) of TiFe + 4 wt% Zr at the different cooling rate. Uncertainty on all values is  $\pm 1$  at. %**

Element	25 mm	13 mm	6 mm	3 mm
Ti (at. %)	51	50	50	51
Fe (at. %)	49	49	49	49
Zr (at. %)	<1	<1	<1	<1

The chemical compositions of the light grey phase for all thicknesses are given in **Table 6.3**. As for TiFe phase, this phase has a constant composition with cooling rates. The stoichiometry of this phase is very close to  $\text{TiFe}_2$ , a compound that is present in the Ti-Fe phase diagram. This phase also contains 3 at. % of zirconium.

**Table 6.3: Chemical composition of light grey phase (Area 2) of TiFe + 4 wt% Zr at the different cooling rate. Uncertainty on all values is  $\pm 1$  at. %**

Element	25 mm	13 mm	6 mm	3 mm
Ti (at. %)	39	38	38	38
Fe (at. %)	58	59	59	59
Zr (at. %)	3	3	3	3

Chemical compositions of the bright phase for all thicknesses are shown in **Table 6.4**. Here, there is a slight variation in the chemical composition with thickness, but overall, we could consider that this phase composition is roughly constant except for the 3 mm thickness, which contains less zirconium than the other three thicknesses. As this Zr-rich, bright phase is located at the interface between the grey and the light grey phases, we could conclude that zirconium tends to be excluded from the TiFe and the  $\text{TiFe}_2$  phases. A close inspection of the abundances given in **Table 6.4** seems to indicate that this region has a composition  $(\text{Ti, Zr})_2\text{Fe}$ . The compound  $\text{Ti}_2\text{Fe}$  is not present in

the phase diagram but it has been seen in the titanium-iron-boron system [109]. As we could see in **Figure 6.2**, bright phase area is very small, only a few % of the total surface.

**Table 6.4: Chemical composition of bright phase (Area 3) of TiFe + 4 wt% Zr at the different cooling rate. Uncertainty on all values is  $\pm 1$  at. %**

Element	25 mm	13 mm	6 mm	3 mm
Ti (at. %)	44	47	44	46
Fe (at. %)	39	35	36	41
Zr (at. %)	17	17	20	12

### 6.2.2 Structural characterization

The crystal structure for samples coming from different thicknesses was determined by analyzing the XRD pattern. The XRD pattern of each sample in the as-cast state is shown in **Figure 6.3**. The major diffraction peaks for all thicknesses were found to be TiFe (space group Pm-3m). There are some minor peaks of low intensity, which could be indexed as TiFe<sub>2</sub> type (space group P6<sub>3</sub>/mmc) and Ti (space group P6<sub>3</sub>/mmc). The small shoulder on the right side of the main TiFe peak is a TiFe<sub>2</sub> peak. The TiFe is the grey phase seen in the SEM micrographs while the TiFe<sub>2</sub> is the light grey phase. The absence of the bright phase in the X-ray patterns could be explained in two ways. First, the area of this phase in the SEM micrographs is very small, only a few % of the total surface. Therefore, it is at the limit of detection for X-ray diffraction. Secondly, from the SEM observation and EDX measurements, this phase is most likely related to the light grey phase. Also, the peak at around 45° could be indexed to the Ti phase but, after Rietveld refinement, there is still a non-negligible residue. Moreover, one could notice a series of very small peaks between 75 and 93°. These peaks may belong to the bright phase, but the intensities are too small and the peaks are too broad to make a precise identification impossible. The Rietveld analysis was performed on each alloy's XRD pattern and the R-values are given in **Table 6.5**. The relatively high value of R<sub>wp</sub> is probably due to the relatively high background of these patterns as discussed by Toby [110].

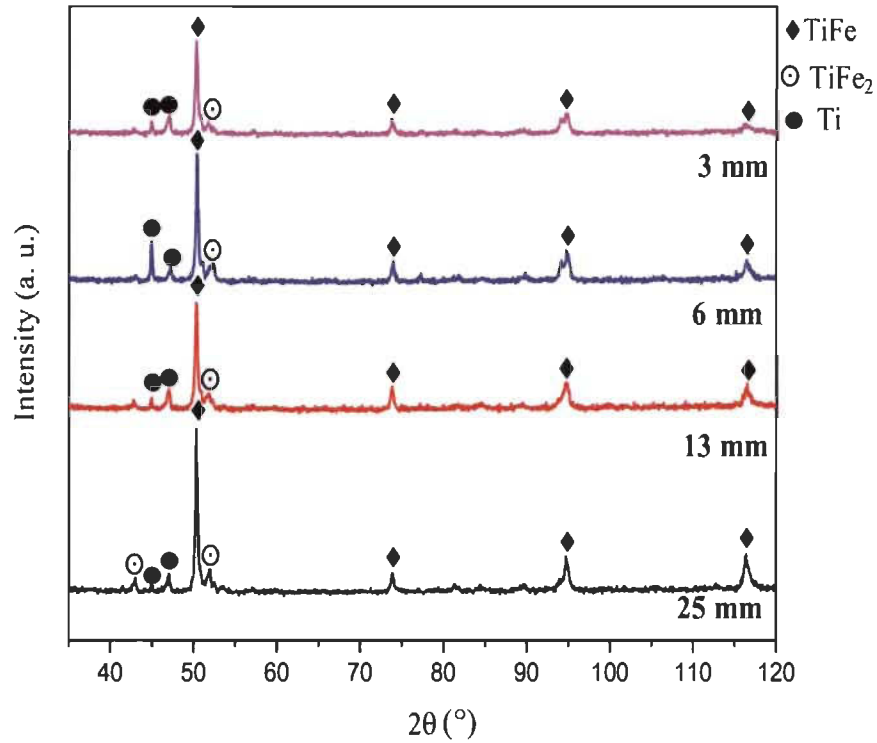


Figure 6.3: X-ray diffraction patterns of each alloy at a different thickness of step mold

Table 6.5: The weighted profile factor R-factor ( $R_{wp}$ ) and the expected R-factor ( $R_{exp}$ ) in Rietveld's analysis for each alloy

Thickness (mm)	$R_{wp}$	$R_{exp}$
25	13.07	9.18
13	12.20	9.57
6	14.98	9.65
3	13.87	11.28

The main parameters determined by Rietveld refinements are summarized in **Table 6.6**. Phase fraction of each phase presented in **Table 6.6** is on weight basis. Pure zirconium phase was also considered during the Rietveld analysis, but this phase is not present in any pattern. We see that the phase fraction of TiFe is practically constant except for the 6 mm sample that is slightly higher. The Ti fraction increases with cooling rates and the fraction of TiFe<sub>2</sub> has one value for the 25 and 13 mm samples and smaller value for the 6 and 3 mm samples. For all cooling rates, the individual

phases have different crystallite size, but they do not change much with cooling rates. For all phases, microstrains were found to be zero within experimental errors.

**Table 6.6: Phase fraction, lattice parameter and crystallite size of each alloy having different thicknesses**

Phase name	Phase fraction (%)	Lattice parameter (Å)	Crystallite size (nm)
<b>25 mm</b>			
TiFe	59(1)	a = 2.98(1)	47(2)
TiFe <sub>2</sub>	32(1)	a = 4.91(1) c = 7.24(1)	10(2)
Ti	9(1)	a = 2.96(1) c = 4.68(1)	33(1)
<b>13 mm</b>			
TiFe	57(1)	a = 2.98(1)	37(2)
TiFe <sub>2</sub>	31(1)	a = 4.93(1) c = 7.23(1)	11(2)
Ti	12(1)	a = 2.98(1) c = 4.60(1)	30(1)
<b>6 mm</b>			
TiFe	67(1)	a = 2.98(1)	35(2)
TiFe <sub>2</sub>	21(1)	a = 4.91(1) c = 7.00(1)	18(2)
Ti	13(1)	a = 2.94(1) c = 4.70(1)	25(2)
<b>3 mm</b>			
TiFe	61(1)	a = 2.98(1)	35(2)
TiFe <sub>2</sub>	23(1)	a = 4.95(1) c = 7.18(1)	10(2)
Ti	16(1)	a = 2.96(1) c = 4.69(1)	27(2)



From **Table 6.6**, it could be seen that the lattice parameters of the  $\text{TiFe}_2$  range from  $a = 4.91$  to  $4.95$  nm,  $c = 7.00$  to  $7.24$  and the  $c/a$  ratio from  $1.43$  to  $1.48$ . The  $c/a$  ratio is particularly problematic. This number is too far from the theoretical value of a hexagonal phase. This is a strong indication that the structure is metastable. Other possible phases were tested but the  $\text{TiFe}_2$  structure was the one giving the best fitting.

### 6.2.3 Activation kinetics

Activation (first hydrogenation) curves of  $\text{TiFe}$  with  $4\text{wt}\%$   $\text{Zr}$  at different cooling rates are shown in **Figure 6.4**. It is clear that the activation kinetics increases with cooling rates. This is most likely due to the finer distribution and large perimeter of the secondary phase as cooling rate increases. There is also less diffusion distance between the secondary phase and the center of the  $\text{TiFe}$  phase. The total capacity gives some indication of the hydrogenation reaction. For example, for the  $3$  mm sample, the total capacity reached was  $1.4$  wt%. Considering that, from Rietveld refinement,  $\text{TiFe}$  phase is  $61\%$  and that  $\text{TiFe}$  absorbs  $1.86$  wt% of hydrogen then, the amount of hydrogen taken by the  $\text{TiFe}$  phase is  $1.13$  wt%. The missing capacity is due to the secondary phase ( $\text{TiFe}_2$  and  $\text{Ti}$ ).

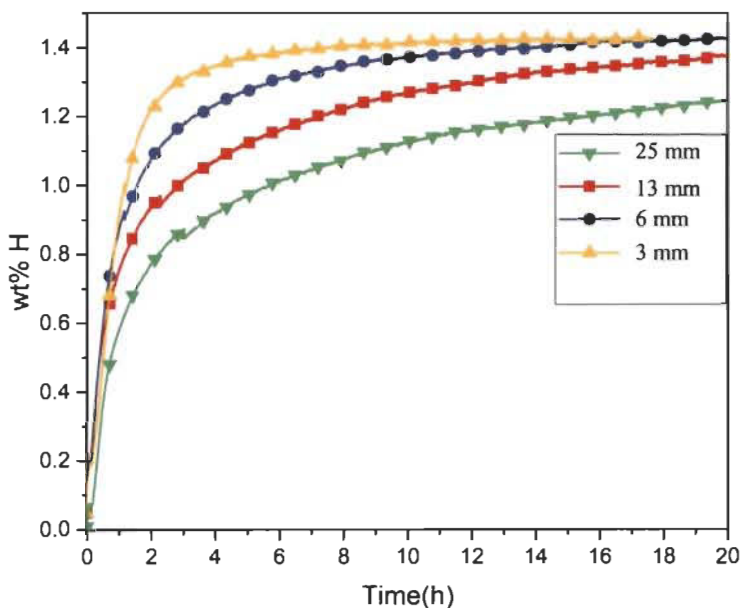


**Figure 6.4: Activation at room temperature and under 20 bars of hydrogen of  $\text{TiFe}+4\text{wt}\%$   $\text{Zr}$  at different thicknesses of step mold**

As the missing capacity is only  $0.27$  wt% and the secondary phases are counting for  $39$  wt%. This means that these phases absorbed only a small amount of hydrogen. The preceding analysis found

that the secondary phases are  $\text{TiFe}_2$ ,  $\text{Ti}_2\text{Fe}$ , and  $\text{Ti}$ . It is known that the  $\text{TiFe}_2$  phase does not absorb hydrogen [111]. It leaves the  $\text{Ti}_2\text{Fe}$  and  $\text{Ti}$  phases, which are possible hydrogen absorbers. Titanium forms a hydride, but the amount formed is too small to be accurately detected by X-ray. As for the  $\text{Ti}_2\text{Fe}$  phase, there is some evidence by SEM/EDX, but the amount is not sufficient to be seen on the XRD pattern. Therefore, more dedicated experiment is needed in order to determine secondary phase absorbs hydrogen and what is the capacity.

The shape of activation curves could give some information about the hydrogenation mechanism. As in previous **Table 4.7**, usual models of rate-limiting steps in hydrogenation were shown. As different models have different functional forms, one way to find the model that fits our experiments is to plot the left side of the equations as a function of time. The model that fits the best will give a straight line. The linear regression was performed from 10 to 90% of the transformed fraction ( $X = [0.1 \dots 0.9]$ ) and the results are shown in **Figure 6.5** for the 3 mm thickness. At 3 mm thickness, the best linear fitted plot is for the GB3D, 3D growth, diffusion controlled with decreasing interface velocity model. GB3D was also found to be the best-fitted model for the other thicknesses.

The rate constant of the reaction for each thickness is shown in **Table 6.7**. Rate constant value increases with increasing cooling rate (decrease in mold thickness). The relationship between the rate constant and perimeter of the secondary phase is shown in **Figure 6.6**. It is clear that the rate constant is linearly proportional to the perimeter. It has already been shown by Edalati et al. that grain boundaries, vacancies concentration, and high dislocation density acts as a pathway for hydrogen diffusion [48, 95]. In the present case, the activation mechanism is at the interface between the  $\text{TiFe}$  phase and the secondary  $\text{TiFe}_2$  phase. From the measured and calculated hydrogen capacity, we could conclude that the secondary phase absorbs only a small amount of hydrogen. Thus, it acts as a gateway for hydrogen. In previous chapter, work on effect of heat treatment, we found that the phases present in the as-cast alloy were metastable and heat treatment was responsible for the effect of changing the nature of the secondary phase and also the metastability of the phases, which had for the consequence of drastically reducing the activation kinetics and total capacity. The present result agrees with these conclusions. In the as-cast state the phases are in a metastable state and thus, probably have an unstable boundary between them. Such an unstable boundary could provide an easy diffusion of hydrogen between the phases.

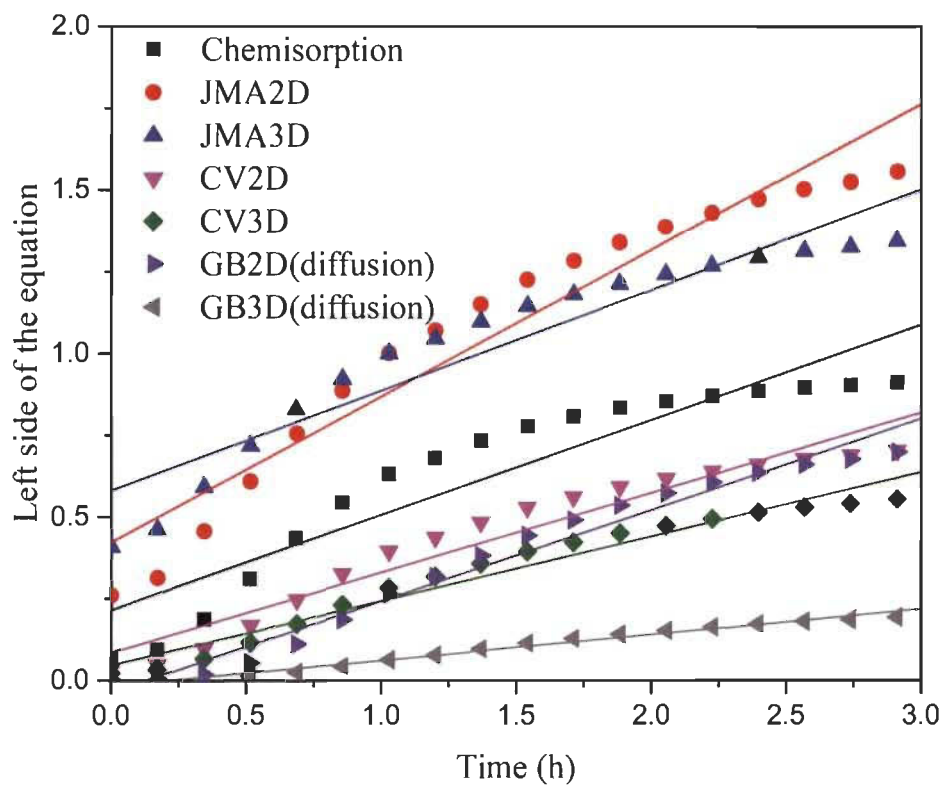
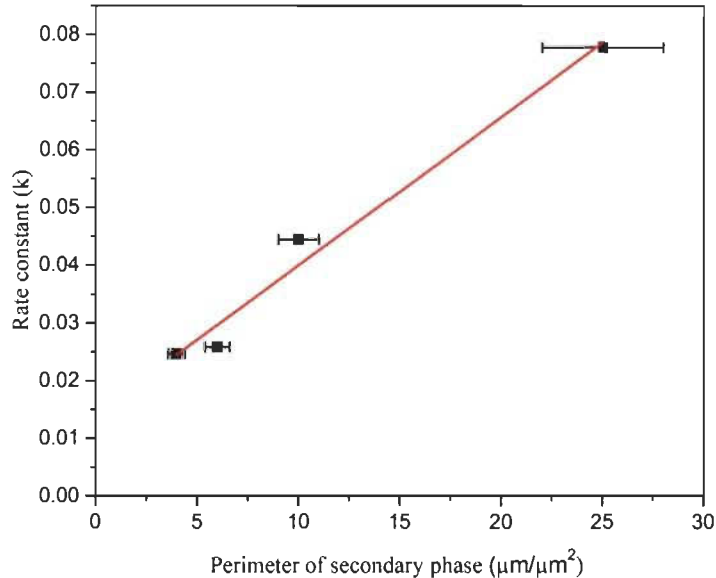


Figure 6.5: Linear fitting of each rate limiting step model for 3 mm thickness

Table 6.7: Rate constant in case of diffusion model equation for each thickness. Error on the last significant digit is in parentheses

Step mold thickness (mm)	Rate constant k (diffusion)
25	0.0247(1)
13	0.0258(2)
6	0.0444(2)
3	0.0777(4)



**Figure 6.6: Activation kinetics rate constant as a function of the perimeter of the secondary phase**

### 6.3 Summary

The effect of cooling rate on TiFe alloy with 4wt% Zr as additive was studied by using step casting. Casting was done at a scale of a few kg in order to be as close as possible to the industrial process. The raw materials were also industrial grade. The cast alloy consisted of a main TiFe phase and a zirconium-rich secondary phase. It was observed that cooling rate had an influence on the alloy's microstructure. Fast cooling rates produced a dendritic structure with fine distribution of the secondary phase. Slower cooling rates produced a coarser structure for the secondary phase. However, the chemical composition of each phase was essentially constant with respect to cooling rates.

In this work it was shown that activation kinetics of as-cast alloys has a clear increase in the reaction rate with increasing cooling rates. The reaction rate was found to be proportional to the secondary phase perimeter and the rate-limiting was identified to be diffusion controlled for all cooling rates. The fact that the rate of the first hydrogenation kinetic is proportional to the perimeter between the TiFe phase and the secondary phase is a strong indication of the gateway mechanism of hydrogen entering first the secondary phase and then transfer to the main TiFe phase.

## Chapter 7

### Microstructure and hydrogen storage properties of $Ti_xFe_{2-x} + 4 \text{ wt\% Zr}$ ( $x = 1.1, 1.05, 0.99, 0.94$ )

#### 7.1 Introduction

In previous chapters, TiFe alloys with the different combinations of additives have been studied. In all these studies, Ti-rich phases could be seen in the microstructure of TiFe alloys with additives. In this chapter, four compositions of TiFe with 4 wt% Zr have been synthesized in order to optimize chemical composition and fully understand the effect of Ti-rich phase on the activation curve of these alloys. The binary phase diagram of TiFe alloy is shown in **Figure 7.1**. In this phase diagram, the composition range of TiFe is very small. Therefore, by varying the concentration of Ti across the  $Ti_xFe_{2-x}$  region ( $x = 1.1, 1.05, 0.99, 0.94$ ), four samples were synthesized with 4 wt% Zr as additive. The effect of variation in the concentration of Ti on the microstructure and activation curve of TiFe alloy is reported in this chapter.

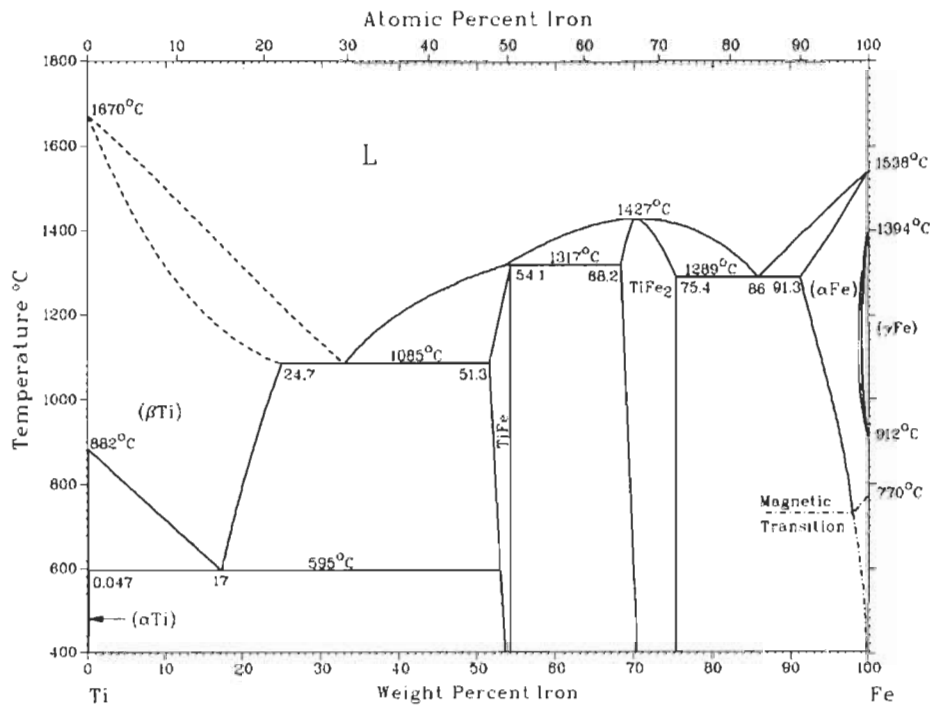


Figure 7.1: Ti-Fe binary phase diagram [112]

## 7.2 Result and discussion

### 7.2.1 Morphology

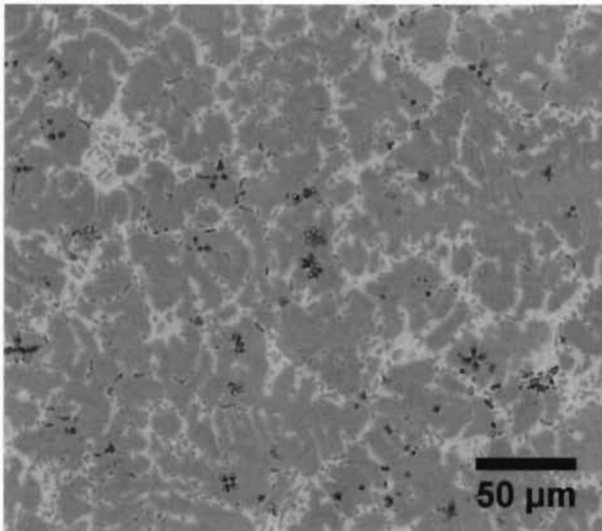
Back-scattered micrographs of all alloys are shown in **Figure 7.2**. A grey phase (TiFe matrix) with secondary phases (bright, light grey and black precipitate) is present in all micrographs. The microstructure is different for each alloy. For  $x = 1.1$ , the secondary phase is finely distributed. When the value of  $x$  decreases (**Figure 7.2 (b), (c) and (d)**), the secondary phase is getting more globular and the black precipitates are more abundant. **Figure 7.3** shows the microstructure at higher magnification for each alloy. For  $x = 1.1$ , the black precipitates present a hexagonal structure (**Figure 7.3 (a)**), whereas, for other alloys, the black precipitates have more irregular shapes. Area percentage of each phase in the micrograph of each alloy was evaluated using ImageJ software and is shown in **Table 7.1**. It could be clearly seen that area fractions are almost constant for  $x = 1.1, 1.05$  and  $0.99$ . In the case of the  $x = 0.94$  composition, we see a drastic change of the proportion of the three phases.

**Table 7.1: Area fraction (%) of different phases in the micrograph of  $Ti_xFe_{2-x}$  with 4 wt% Zr as additive, where  $x = 1.1, 1.05, 0.99$  and  $0.94$  (uncertainty on all values is  $\pm 1$ )**

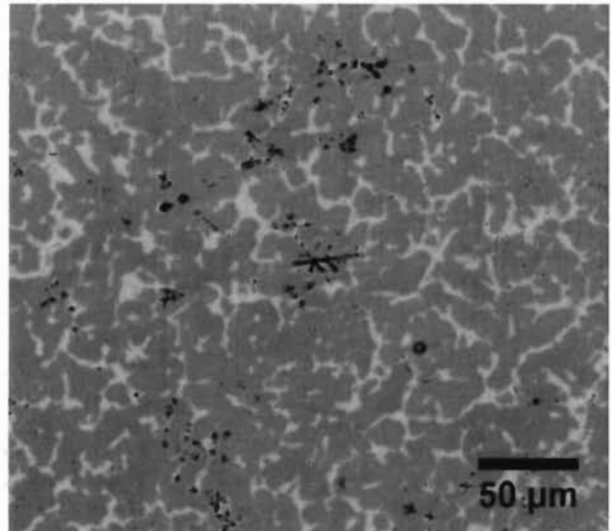
Phases	$x = 1.1$	$x = 1.05$	$x = 0.99$	$x = 0.94$
Bright	20	19	20	40
Light grey	77	78	76	50
Black precipitate	3	3	4	11

The chemical composition of each phase was evaluated by EDX analysis as shown in **Figure 7.3**. The chemical composition of each phase for  $x = 1.1$  is shown in **Table 7.2**. The matrix (area 1) is TiFe phase with 3 at. % of Zr. The bright phase (area 2) has a composition close to  $Ti_2Fe$  with 8 at. % of Zr substituting with Ti. Areas 3, 4 and 5 are essentially Ti-rich regions. In particular, area 5 shows the hexagonal structure of Ti crystal structure.

**(a)  $x = 1.1$**



**(b)  $x = 1.05$**



**(c)  $x = 0.99$**



**(d)  $x = 0.94$**

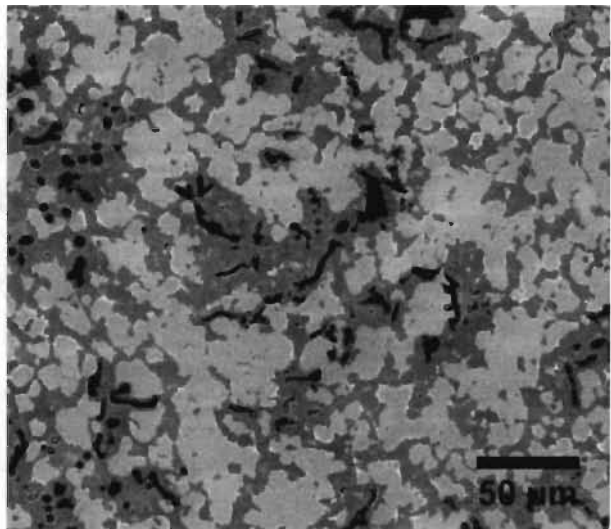
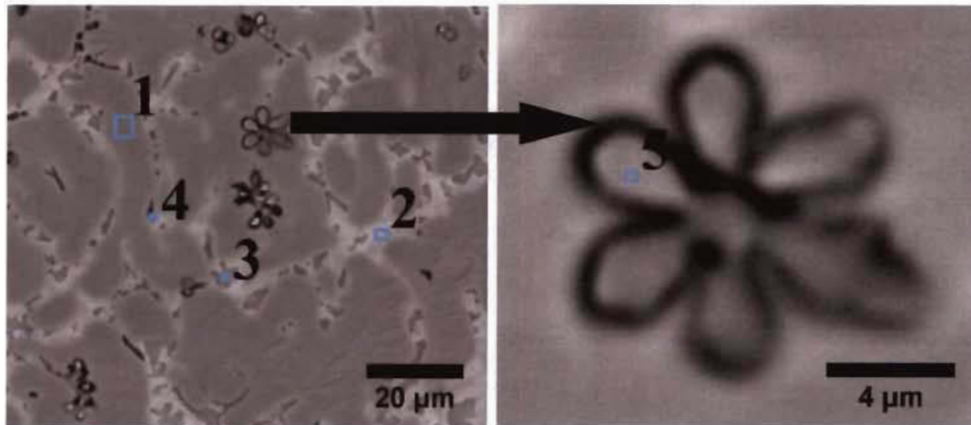
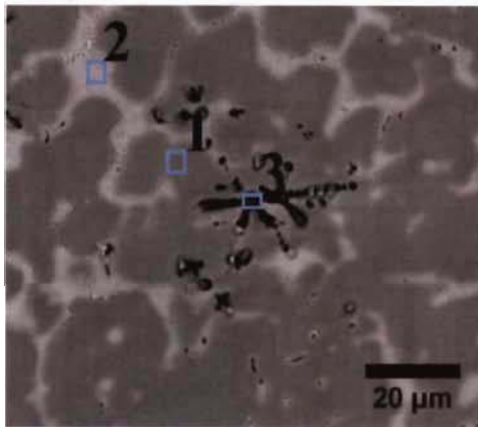


Figure 7.2: Back-scattered micrograph of  $Ti_xFe_{2-x}$  with 4 wt% Zr as additive, where  $x = 1.1, 1.05, 0.99$  and  $0.94$

**(a)  $x = 1.1$**



**(b)  $x = 1.05$**



**(c)  $x = 0.99$**



**(d)  $x = 0.94$**

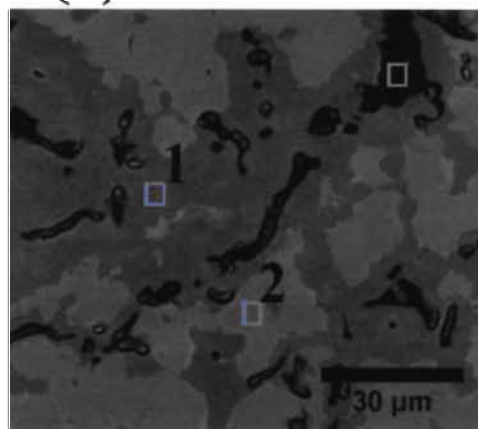


Figure 7.3: Chemical composition analysis of  $\text{Ti}_x\text{Fe}_{2-x}$  with 4 wt% Zr as additive, where  $x = 1.1$ , 1.05, 0.99 and 0.94



**Table 7.2: Chemical composition of each phase for  $x = 1.1$  (uncertainty on all values is  $\pm 1$ )**

Alloy	Ti (at. %)	Fe (at. %)	Zr (at. %)
<b><math>x = 1.1</math></b>			
<i>Matrix (area 1)</i>	51	46	3
<i>Bright phase (area 2)</i>	59	33	8
<i>Ti-rich (area 3)</i>	70	24	6
<i>Ti-rich (area 4)</i>	69	27	4
<i>Ti-rich (area 5)</i>	71	27	3

The chemical composition of each phase for  $x = 1.05$  as shown in **Figure 7.3 (b)** is presented in **Table 7.3**. The matrix (area 1) and bright phase (area 2) have compositions very similar to their equivalents in alloy  $x = 1.1$ . Ti-rich phase (area 3) is now more enriched in Ti compared to  $x = 1.1$ .

**Table 7.3: Chemical composition of each phase for  $x = 1.05$  (uncertainty on all values is  $\pm 1$ )**

Alloy	Ti (at. %)	Fe (at. %)	Zr (at. %)
<b><math>x = 1.05</math></b>			
<i>Matrix (area 1)</i>	50	46	4
<i>Bright phase (area 2)</i>	55	37	8
<i>Ti-rich (area 3)</i>	85	12	3

The chemical composition of the phases presents in the alloy  $x = 0.99$  are shown in **Table 7.4** with the corresponding micrograph shown in **Figure 7.3 (c)**. Here, the matrix phase has an almost equal atomic concentration of Ti and Fe with a small concentration ( $<1$  at. %) of Zr. The bright phase has also a totally different composition compared to the previous alloys. In fact, the composition of the bright phase seems to be close to  $\text{TiFe}_2$ . Area 3 has the same composition as for  $x = 1.05$  which is Ti-rich.

**Table 7.4: Chemical composition of each phase for x = 0.99 (uncertainty on all values is ± 1)**

Alloy	Ti (at. %)	Fe (at. %)	Zr (at. %)
<b>x = 0.99</b>			
<i>Matrix (area 1)</i>	50	49	< 1
<i>Bright phase (area 2)</i>	36	56	6
<i>Ti-rich (area 3)</i>	80	18	4

For x = 0.94, chemical composition for each phase (**Figure 7.3 (d)**) has been evaluated by the EDX analysis and shown in **Table 7.5**. Area 1 is TiFe which has more Zr (~ 3 at%) than for x = 0.99 and almost the same as for x = 1.1 and 1.05. Bright phase has TiFe<sub>2</sub> composition as found for x = 0.99.

**Table 7.5: Chemical composition of each phase for x = 0.94 (uncertainty on all values is ± 1)**

Alloys	Ti (at. %)	Fe (at. %)	Zr (at. %)
<b>x = 0.94</b>			
<i>Matrix (area 1)</i>	50	48	3
<i>Bright phase (area 2)</i>	39	56	4
<i>Ti-rich (area 3)</i>	81	16	3

In the bright phase, Zr content is comparable to x = 0.99 and almost half of the concentration of Zr in the bright phase of x = 1.1 and 1.05. Area 3 is mainly Ti-rich phase. From chemical composition analysis of these alloys, we could conclude that variation in the Ti/Fe concentration leads to the change in the bright phase's composition and also change in the solubility of zirconium in all phases in each alloy.

### 7.2.2 Structural characterization

X-ray diffraction patterns of each alloy are shown in **Figure 7.4**. In the case of x = 1.1 and x = 1.05, major peaks of TiFe with minor peaks of Ti<sub>2</sub>Fe could be seen. When x value decreases, appearance of minor peaks of TiFe<sub>2</sub> phase along with major peaks of TiFe phase could be observed for x = 0.99 and x = 0.94. Rietveld analysis for each alloy's X-ray diffraction pattern was

performed and calculated phase fraction with crystallite size and lattice parameter for each phase is shown in **Table 7.6**.

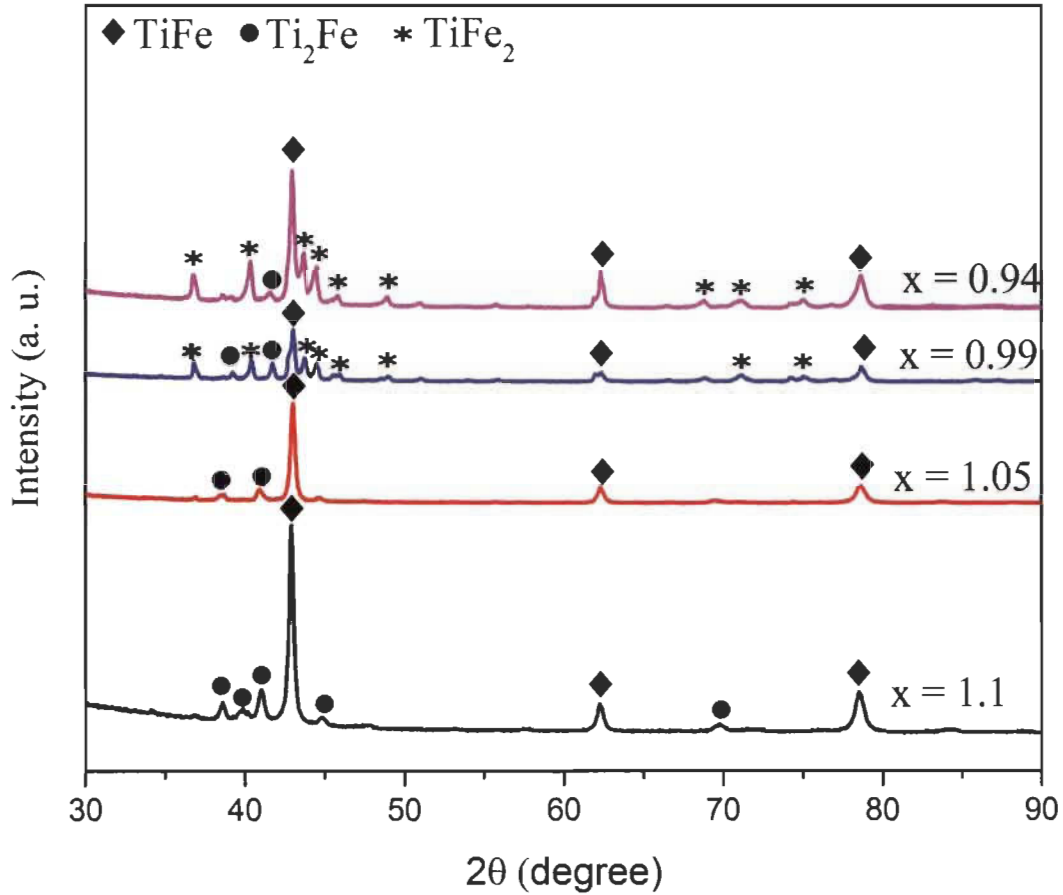


**Figure 7.4:** X-ray diffraction patterns of  $Ti_xFe_{2-x}$  with 4 wt% Zr as additive, where  $x = 1.1, 1.05, 0.99$  and  $0.94$

We could clearly see a decreasing trend for the phase fraction  $Ti_2Fe$  with decreasing  $x$  value. For  $x = 0.99$  and  $x = 0.94$ , phase fraction of  $TiFe_2$  is almost constant. Crystallite size of  $TiFe$  also decreases with the decrease in  $x$  value. Crystallite size of  $Ti_2Fe$  and  $TiFe_2$  phases is found to be almost constant. Lattice parameter is almost constant for each phase in each alloy. Appearance of these phases could also be seen in the chemical composition analysis of each alloy respectively.

**Table 7.6: Evaluated Phase fraction, lattice parameter and crystallite size values for each phase in of  $Ti_xFe_{2-x}$  alloys with 4 wt% Zr as additive**

Phase name	Phase fraction (%)	Lattice parameter (Å)	Crystallite size (nm)
<b>x = 1.1</b>			
TiFe	72(1)	a = 2.98(1)	46(1)
Ti <sub>2</sub> Fe	28(1)	a = 11.45(1)	26(2)
<b>x = 1.05</b>			
TiFe	82(1)	a = 2.98(3)	39(2)
Ti <sub>2</sub> Fe	18(1)	a = 11.48(1)	22(2)
<b>x = 0.99</b>			
TiFe	40(1)	a = 2.97(1)	31(2)
Ti <sub>2</sub> Fe	17(1)	a = 11.26(1)	28(1)
TiFe <sub>2</sub>	43(1)	a = 4.86(1) c = 7.91(1)	44(1)
<b>x = 0.94</b>			
TiFe	48(1)	a = 2.98(1)	32(2)
Ti <sub>2</sub> Fe	9(1)	a = 11.32(1)	16(2)
TiFe <sub>2</sub>	43(1)	a = 4.88(1) c = 7.92(1)	43(1)

### 7.2.3 Activation kinetics

The first hydrogenation curves of all samples at room temperature under 20 bar hydrogen pressure are shown in **Figure 7.5**. Best kinetics and maximum hydrogen capacity were found to be for  $x = 1.1$ . It absorbs 2 wt% hydrogen within 2 hours. When  $x = 1.05$ , kinetics is slower, but the main fact is that the hydrogen capacity reduces to 1.5 wt%. For  $x = 0.99$  and 0.94, the trend of decreasing capacity with lowering of  $x$  value is confirmed. The main reason for this decreasing trend is due to the appearance of non-hydriding TiFe<sub>2</sub> phase for  $x = 0.99$  and 0.94 along with hydriding phase TiFe and Ti<sub>2</sub>Fe. From **Table 7.6**, we could see the phase fractions of TiFe and Ti<sub>2</sub>Fe and a decreasing trend was found with lowering the  $x$  value. From the chemical composition analysis, we observed that when value of  $x$  decreases, bright phase's composition changes from Ti<sub>2</sub>Fe to

TiFe<sub>2</sub>. From the activation kinetics results, it is clear that Ti<sub>2</sub>Fe phase is helpful for the initiation of hydrogen absorption and also leads to the better maximum hydrogen capacity.

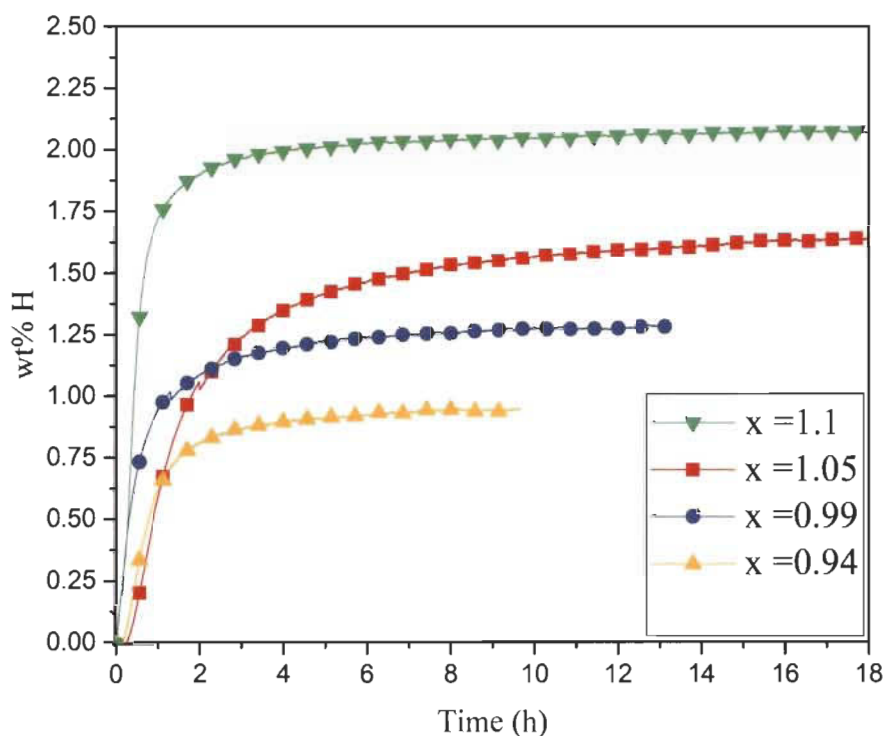


Figure 7.5: Activation kinetics of Ti<sub>x</sub>Fe<sub>2-x</sub> with 4 wt% Zr as additive at room temperature under 20 bar hydrogen pressure

### 7.3 Summary

Effect of Ti-rich phase was clearly observed on the activation kinetics of TiFe alloy with 4 wt% Zr. The best kinetics was found to be for  $x = 1.1$ . Maximum hydrogen capacity for  $x = 1.1$  was 2 wt%. A fine distribution of secondary phase could be seen in the case of  $x = 1.1$ , however, for others, this secondary phase is getting more globular. Therefore, the best alloy according to fast kinetics and maximum hydrogen capacity was found to be Ti<sub>1.1</sub>Fe<sub>0.9</sub> + 4 wt% Zr.

## Chapter 8

### Conclusion and future work

---

Microstructure and hydrogen storage properties of TiFe alloy with Zr, V and Mn have been investigated. The best alloy composition was found to be TiFe alloy with 2 wt% Mn + 4 wt% Zr. It has the best kinetics and maximum hydrogen capacity (2 wt%). Combination of 2 wt% Zr and V leads to a remarkable improvement in the kinetics of TiFe alloy compared to the alloys with Zr only and with V only. Combination of Mn and V has been also studied at different concentration level of Mn and V. Effect of heat treatment and cooling rate on the microstructure and hydrogen storage properties of TiFe alloy with 4 wt% Zr as additive have been also investigated. Heat treatment has a detrimental effect on the activation kinetics, however, higher cooling rate during synthesis of alloy leads to the better kinetics of the TiFe alloy. Four samples of  $Ti_xFe_{2-x}$ ; where, ( $x = 1.1, 1.05, 0.99, 0.94$ ) with 4 wt% Zr has been also synthesized in order to see the effect of Ti-rich phase. The best alloy composition was  $Ti_{1.1}Fe_{0.9} + 4$  wt% Zr. It absorbs 2 wt% hydrogen within 2 hours and it has the best kinetics than other alloys.

These investigations were targeted mainly to the improvement of the first hydrogenation. Future work should be on the thermodynamic and cycling properties of these alloys. To have a better understanding of the exact mechanism of secondary phase in hydrogenation process, secondary phase composition could directly be cast and its hydrogenation properties measured. Cooling rate value could be simulated for getting a better correlation with the activation kinetics. Comparison of different industrial methods for synthesis of TiFe alloy could be studied in order to optimize the synthesis process and also to get a better understanding of microstructure evolution.

After finding the thermodynamic and cycling properties of TiFe alloy with different additive, the best alloy having good hydrogen storage properties could be used as low temperature metal hydride in the metal hydride based reactor. Reactor design of TiFe alloy can be done for heat exchanger. Electrochemical measurements of TiFe alloy with different additives could be made in order to know the charging and discharging capacity.

## List of publications and conferences

---

### Publications:

1. **A.K. Patel**, P. Sharma, J. Huot, Effect of annealing on microstructure and hydrogenation properties of TiFe + X wt% Zr (X = 4, 8), *International Journal of Hydrogen Energy*, 43 (2018) 6238-6243.
2. **A.K. Patel**, B. Tougas, P. Sharma, J. Huot, Effect of cooling rate on the microstructure and hydrogen storage properties of TiFe with 4 wt% Zr as an additive, *Journal of Materials Research and Technology*, 8 (2019) 5623-5630.
3. **A.K. Patel**, A. Duguay, B. Tougas, C. Schade, P. Sharma, J. Huot, Microstructure and first hydrogenation properties of TiFe alloy with Zr and Mn as additives, *International Journal of Hydrogen Energy*, 45 (2020) 787-797.
4. **A.K. Patel**, D. Silva Dos Santos, P. Sharma, and J. Huot, Microstructure and hydrogen storage properties of  $Ti_xFe_{2-x} + 4$  wt% Zr, (x = 1.1, 1.05, 0.99, 0.94) (Submitted)
5. **A.K. Patel**, A. Duguay, B. Tougas, C. Schade, P. Sharma, and J. Huot, Microstructure and hydrogen storage properties of TiFe alloy with Zr + V and combination of Zr + Mn + V as additives (In process)
6. **A.K. Patel**, A. Duguay, B. Tougas, C. Schade, P. Sharma, and J. Huot, Microstructure and hydrogen storage properties of TiFe alloy with Mn + V as additives (In process)

### Conferences:

- (1) **A.K. Patel**, P. Sharma, and J. Huot; *Hydrogen storage properties of TiFe + X wt.% Zr, V (X=0, 4) alloys*; Canadian Association of Physicists (CAP) Congress – University of Ottawa, (Ottawa, Ontario), Canada, 2016 (**Poster presentation**)
- (2) **A.K. Patel**, P. Sharma, and J. Huot; *Effect of annealing on hydrogenation properties and microstructure of TiFe + X wt% Zr (X= 4, 8)*; Gordon Research Conference (Hydrogen-Metal Systems), Stonehill College 320 Washington Street Easton, MA, US, 2017 (**Poster presentation**)

(3) **A.K. Patel**, B. Tougas, P. Sharma, and J. Huot; *Effect of cooling rate on the microstructure and hydrogen storage properties of TiFe with 4 wt% Zr as an additive*; “16th International Symposium on Metal-Hydrogen Systems”, Guangzhou, China, Oct. 28th– Nov. 2nd 2018 (MH 2018) (**Poster presentation**)



## Reference

---

- [1] M. Höök, X. Tang, Depletion of fossil fuels and anthropogenic climate change: A review, *Energy Policy*, 52 (2013) 797-809.
- [2] T. Beer, T. Grant, D. Williams, H. Watson, Fuel-cycle greenhouse gas emissions from alternative fuels in Australian heavy vehicles, *Atmospheric Environment*, 36 (2002) 753-763.
- [3] R.B. Gupta, *Hydrogen fuel: production, transport, and storage*, (2009).
- [4] U.S. Department of Energy, DOE Technical Targets for Onboard Hydrogen Storage for Light-Duty Vehicles, Office of Energy Efficiency and Renewable Energy, Washinton DC, USA, (2017).
- [5] M. Hirscher, *Handbook of hydrogen storage: new materials for future energy storage*, Wiley-VCH, 2010.
- [6] A. Züttel, A. Borgschulte, L. Schlapbach, *Hydrogen as a future energy carrier*, Wiley-VCH, Weinheim, 2008.
- [7] L. Klebanoff, *Hydrogen storage technology: materials and applications*, Boca Raton: CRC Press, 2016.
- [8] R.K. Ahluwalia, T.Q. Hua, J.K. Peng, S. Lasher, K. McKenney, J. Sinha, M. Gardiner, Technical assessment of cryo-compressed hydrogen storage tank systems for automotive applications, *International Journal of Hydrogen Energy*, 35 (2010) 4171-4184.
- [9] S.M. Aceves, G.D. Berry, J. Martinez-Frias, F. Espinosa-Loza, Vehicular storage of hydrogen in insulated pressure vessels, *International Journal of Hydrogen Energy*, 31 (2006) 2274-2283.
- [10] J.J. Reilly, Metal Hydride Technology, *Zeitschrift für Physikalische Chemie*, 117 (1979), 155-184.
- [11] E.M. Borzone, A. Baruj, M.V. Blanco, G.O. Meyer, Dynamic measurements of hydrogen reaction with  $\text{LaNi}_5\text{-xSn}_x$  alloys, *International Journal of Hydrogen Energy*, 38 (2013) 7335-7343.
- [12] R.V. Denys, B. Riabov, V.A. Yartys, R.G. Delaplane, M. Sato, Hydrogen storage properties and structure of  $\text{La}_{1-x}\text{Mg}_x(\text{Ni}_{1-y}\text{Mn}_y)_3$  intermetallics and their hydrides, *Journal of Alloys and Compounds*, 446-447 (2007) 166-172.
- [13] L. Shcherbakova, M. Spodaryk, Y. Solonin, A. Samelyuk, Effects of particle size and type of conductive additive on the electrode performances of gas atomized AB5-type hydrogen storage alloy, *International Journal of Hydrogen Energy*, 38 (2013) 12133-12139.

- [14] V.K. Sharma, E. Anil Kumar, Effect of measurement parameters on thermodynamic properties of La-based metal hydrides, *International Journal of Hydrogen Energy*, 39 (2014) 5888-5898.
- [15] J. Prigent, J.M. Joubert, M. Gupta, Modification of the hydrogenation properties of LaNi<sub>5</sub> upon Ni substitution by Rh, Ir, Pt or Au, *Journal of Alloys and Compounds*, 511 (2012) 95-100.
- [16] H. Ye, B. Xia, W. Wu, K. Du, H. Zhang, Effect of rare earth composition on the high-rate capability and low-temperature capacity of AB<sub>5</sub>-type hydrogen storage alloys, *Journal of Power Sources*, 111 (2002) 145-151.
- [17] S. Mitrokhin, T. Zotov, E. Movlaev, V. Verbetsky, Hydrogen interaction with intermetallic compounds and alloys at high pressure, *Journal of Alloys and Compounds*, 580 (2013) S90-S93.
- [18] R.K. Jain, A. Jain, S. Agarwal, N.P. Lalla, V. Ganesan, D.M. Phase, I.P. Jain, Characterization and hydrogenation of CeNi<sub>5-x</sub>Cr<sub>x</sub> (x=0, 1, 2) alloys, *Journal of Alloys and Compounds*, 430 (2007) 165-169.
- [19] R.K. Jain, A. Jain, I.P. Jain, Effect of La-content on the hydrogenation properties of the Ce<sub>1-x</sub>La<sub>x</sub>Ni<sub>3</sub>Cr<sub>2</sub> (x=0.2, 0.4, 0.6, 0.8, 1) alloys, *International Journal of Hydrogen Energy*, 37 (2012) 3683-3688.
- [20] R.K. Jain, A. Jain, S. Agarwal, N.P. Lalla, V. Ganesan, D.M. Phase, I.P. Jain, Hydrogenation behaviour of Ce-based AB<sub>5</sub> intermetallic compounds, *Journal of Alloys and Compounds*, 440 (2007) 84-88.
- [21] D. Shaltiel, I. Jacob, D. Davidov, Hydrogen absorption and desorption properties of AB<sub>2</sub> laves-phase pseudobinary compounds, *Journal of the Less Common Metals*, 53 (1977) 117-131.
- [22] T. Maeda, T. Fuura, I. Matsumoto, Y. Kawakami, M. Masuda, Cyclic stability test of AB<sub>2</sub> type (Ti, Zr)(Ni, Mn, V, Fe)<sub>2.18</sub> for stationary hydrogen storage in water contaminated hydrogen, *Journal of Alloys and Compounds*, 580 (2013) S255-S258.
- [23] M. Young, S. Chang, K. Young, J. Nei, Hydrogen storage properties of ZrV<sub>x</sub>Ni<sub>3.5-x</sub> (x=0.0–0.9) metal hydride alloys, *Journal of Alloys and Compounds*, 580 (2013) S171-S174.
- [24] K. Young, D.F. Wong, S. Yasuoka, J. Ishida, J. Nei, J. Koch, Different failure modes for V-containing and V-free AB<sub>2</sub> metal hydride alloys, *Journal of Power Sources*, 251 (2014) 170-177.
- [25] K. Young, B. Reichman, M.A. Fetcenko, Electrochemical performance of AB<sub>2</sub> metal hydride alloys measured at -40°C, *Journal of Alloys and Compounds*, 580 (2013) S349-S352.

- [26] K. Young, T. Ouchi, J. Nei, L. Wang, Annealing effects on Laves phase-related body-centered-cubic solid solution metal hydride alloys, *Journal of Alloys and Compounds*, 654 (2016) 216-225.
- [27] Y. Wang, M. Zhao, L. Wang, Effect of La–Mg-based alloy addition on structure and electrochemical characteristics of Ti<sub>0.10</sub>Zr<sub>0.15</sub>V<sub>0.35</sub>Cr<sub>0.10</sub>Ni<sub>0.30</sub> hydrogen storage alloy, *International Journal of Hydrogen Energy*, 34 (2009) 2646-2653.
- [28] Q. Yao, H. Zhou, Z. Wang, X. Huang, The isothermal section at 500°C of the La–Ni–V ternary system, *Journal of Alloys and Compounds*, 448 (2008) 195-197.
- [29] M. Okada, T. Kuriwa, A. Kamegawa, H. Takamura, Role of intermetallics in hydrogen storage materials, *Materials Science and Engineering: A*, 329-331 (2002) 305-312.
- [30] N. Endo, H. Saitoh, A. Machida, Y. Katayama, Formation of BCC TiFe hydride under high hydrogen pressure, *International Journal of Hydrogen Energy*, 38 (2013) 6726-6729.
- [31] L. Pickering, J. Li, D. Reed, A.I. Bevan, D. Book, Ti–V–Mn based metal hydrides for hydrogen storage, *Journal of Alloys and Compounds*, 580 (2013) S233-S237.
- [32] X. Zhao, J. Zhou, X. Shen, M. Yang, L. Ma, Structure and electrochemical hydrogen storage properties of A2B-type Ti–Zr–Ni alloys, *International Journal of Hydrogen Energy*, 37 (2012) 5050-5055.
- [33] J.J. Reilly, R.H. Wiswall, Reaction of hydrogen with alloys of magnesium and nickel and the formation of Mg<sub>2</sub>NiH<sub>4</sub>, *Inorganic Chemistry*, 7 (1968) 2254-2256.
- [34] D.H. Xie, P. Li, C.X. Zeng, J.W. Sun, X.H. Qu, Effect of substitution of Nd for Mg on the hydrogen storage properties of Mg<sub>2</sub>Ni alloy, *Journal of Alloys and Compounds*, 478 (2009) 96-102.
- [35] J.J. Reilly, R.H. Wiswall, Formation and properties of iron titanium hydride, *Inorganic Chemistry*, 13 (1974) 218-222.
- [36] N.A.A. Rusman, M. Dahari, A review on the current progress of metal hydrides material for solid-state hydrogen storage applications, *International Journal of Hydrogen Energy*, 41 (2016) 12108-12126.
- [37] K.C. Hoffman, J.J. Reilly, F.J. Salzano, C.H. Waide, R.H. Wiswall, W.E. Winsche, Metal hydride storage for mobile and stationary applications, *International Journal of Hydrogen Energy*, 1 (1976) 133-151.

- [38] J. Bellosta von Colbe, J.-R. Ares, J. Barale, M. Baricco, C. Buckley, G. Capurso, N. Gallandat, D.M. Grant, M.N. Guzik, I. Jacob, E.H. Jensen, T. Jensen, J. Jepsen, T. Klassen, M.V. Lototskyy, K. Manickam, A. Montone, J. Puszkiel, S. Sartori, D.A. Sheppard, A. Stuart, G. Walker, C.J. Webb, H. Yang, V. Yartys, A. Züttel, M. Dornheim, Application of hydrides in hydrogen storage and compression: Achievements, outlook and perspectives, *International Journal of Hydrogen Energy*, 44 (2019) 7780-7808.
- [39] M. Gambini, T. Stilo, M. Vellini, Hydrogen storage systems for fuel cells: Comparison between high and low-temperature metal hydrides, *International Journal of Hydrogen Energy*, 44 (2019) 15118-15134.
- [40] G. Sandrock, A panoramic overview of hydrogen storage alloys from a gas reaction point of view, *Journal of Alloys and Compounds*, 293-295 (1999) 877-888.
- [41] P. Jain, C. Gosselin, J. Huot, Effect of Zr, Ni and Zr<sub>7</sub>Ni<sub>10</sub> alloy on hydrogen storage characteristics of TiFe alloy, *International Journal of Hydrogen Energy*, 40 (2015) 16921-16927.
- [42] P. Jain, C. Gosselin, N. Skryabina, D. Fruchart, J. Huot, Hydrogenation properties of TiFe with Zr<sub>7</sub>Ni<sub>10</sub> alloy as additive, *Journal of Alloys and Compounds*, 636 (2015) 375-380.
- [43] H.S. Chung, J.Y. Lee, Effect of partial substitution of Mn and Ni for Fe in FeTi on hydriding kinetics, *International Journal of Hydrogen Energy*, 11 (1986) 335-339.
- [44] S.M. Lee, T.P. Perng, Effect of the second phase on the initiation of hydrogenation of TiFe<sub>1-x</sub>M<sub>x</sub> (M = Cr, Mn) alloys, *International Journal of Hydrogen Energy*, 19 (1994) 259-263.
- [45] A. Guéguen, M. Latroche, Influence of the addition of vanadium on the hydrogenation properties of the compounds TiFe<sub>0.9</sub>V<sub>x</sub> and TiFe<sub>0.8</sub>Mn<sub>0.1</sub>V<sub>x</sub> (x=0, 0.05 and 0.1), *Journal of Alloys and Compounds*, 509 (2011) 5562-5566.
- [46] B. Abrashev, T. Spassov, S. Bliznakov, A. Popov, Microstructure and electrochemical hydriding/dehydriding properties of ball-milled TiFe-based alloys, *International Journal of Hydrogen Energy*, 35 (2010) 6332-6337.
- [47] V. Zadorozhnyy, S. Klyamkin, M. Zadorozhnyy, O. Bermesheva, S. Kaloshkin, Hydrogen storage nanocrystalline TiFe intermetallic compound: Synthesis by mechanical alloying and compacting, *International Journal of Hydrogen Energy*, 37 (2012) 17131-17136.
- [48] K. Edalati, J. Matsuda, A. Yanagida, E. Akiba, Z. Horita, Activation of TiFe for hydrogen storage by plastic deformation using groove rolling and high-pressure torsion: Similarities and differences, *International Journal of Hydrogen Energy*, 39 (2014) 15589-15594.

- [49] K. Edalati, M. Matsuo, H. Emami, S. Itano, A. Alhamidi, A. Staykov, D.J. Smith, S.-i. Orimo, E. Akiba, Z. Horita, Impact of severe plastic deformation on microstructure and hydrogen storage of titanium-iron-manganese intermetallics, *Scripta Materialia*, 124 (2016) 108-111.
- [50] X.B. Han, Y. Qian, W. Liu, D.M. Chen, K. Yang, Effect of Preparation Technique on Microstructure and Hydrogen Storage Properties of LaNi<sub>3.8</sub>Al<sub>1.0</sub>Mn<sub>0.2</sub> Alloys, *Journal of Materials Science & Technology*, 32 (2016) 1332-1338.
- [51] H. Nakamura, Y. Nakamura, S. Fujitani, I. Yonezu, Influence of annealing on hydrogenation characteristics and microstructure of LaNi<sub>4.55</sub>Al<sub>0.45</sub> alloy, *Journal of Alloys and Compounds*, 218 (1995) 216-220.
- [52] M. Abe, T. Kuji, Hydrogen absorption of TiFe alloy synthesized by ball milling and post-annealing, *Journal of Alloys and Compounds*, 446-447 (2007) 200-203.
- [53] X. Shi, W. Zeng, Y. Long, Y. Zhu, Microstructure evolution and mechanical properties of near- $\alpha$  Ti-8Al-1Mo-1V alloy at different solution temperatures and cooling rates, *Journal of Alloys and Compounds*, 727 (2017) 555-564.
- [54] J. Zhao, T. Wang, J. Chen, L. Fu, J. He, Effect of Cooling Rate on Morphology of TiAl<sub>3</sub> Particles in Al-4Ti Master Alloy, *Materials (Basel)*, 10 (2017).
- [55] L.Y. Zhang, B.D. Zhou, Z.J. Zhan, Y.Z. Jia, S.F. Shan, B.Q. Zhang, W.K. Wang, Mechanical properties of cast A356 alloy, solidified at cooling rates enhanced by phase transition of a cooling medium, *Materials Science and Engineering: A*, 448 (2007) 361-365.
- [56] B.-Y. Chen, K.-S. Hwang, K.-L. Ng, Effect of cooling process on the  $\alpha$  phase formation and mechanical properties of sintered Ti-Fe alloys, *Materials Science and Engineering: A*, 528 (2011) 4556-4563.
- [57] G. Catherine, S. Dilson, H. Jacques, First hydrogenation enhancement in TiFe alloys for hydrogen storage, *Journal of Physics D: Applied Physics*, 50 (2017) 375303.
- [58] P. Lv, J. Huot, Hydrogenation improvement of TiFe by adding ZrMn<sub>2</sub>, *Energy*, 138 (2017) 375-382.
- [59] L. Schlapbach, *Surface Properties and Activation in Hydrogen in Intermetallic Compounds II*, Springer-Verlag, Berlin, 67 (1992) 15.
- [60] G. Bruzzone, G. Costa, M. Ferretti, G.L. Olcese, Hydrogen storage in a beryllium substituted TiFe compound, *International Journal of Hydrogen Energy*, 5 (1980) 317-322.

- [61] G. Bruzzone, G. Costa, M. Ferretti, G.L. Olcese, Hydrogen storage in aluminium-substituted TiFe compounds, *International Journal of Hydrogen Energy*, 6 (1981) 181-184.
- [62] S.H. Lim, L. Jai-Young, The effects of aluminium substitution in TiFe on its hydrogen absorption properties, *Journal of the Less Common Metals*, 97 (1984) 65-71.
- [63] T.H. Jang, J.I. Han, L. Jai-Young, Effect of substitution of titanium by zirconium in TiFe on hydrogenation properties, *Journal of the Less Common Metals*, 119 (1986) 237-246.
- [64] H. Nagai, K. Kitagaki, K.-i. Shoji, Hydrogen Storage Characteristics of FeTi Containing Zirconium, *Transactions of the Japan Institute of Metals*, 29 (1988) 494-501.
- [65] N. Nishimiya, T. Wada, A. Matsumoto, K. Tsutsumi, Hydriding characteristics of zirconium-substituted FeTi, *Journal of Alloys and Compounds*, 313 (2000) 53-58.
- [66] M. Bououdina, D. Fruchart, S. Jacquet, L. Pontonnier, J.L. Soubeyroux, Effect of nickel alloying by using ball milling on the hydrogen absorption properties of TiFe, *International Journal of Hydrogen Energy*, 24 (1999) 885-890.
- [67] P. Lv, J. Huot, Hydrogen storage properties of Ti<sub>0.95</sub>FeZr<sub>0.05</sub>, TiFe<sub>0.95</sub>Zr<sub>0.05</sub> and TiFeZr<sub>0.05</sub> alloys, *International Journal of Hydrogen Energy*, 41 (2016) 22128-22133.
- [68] S. Lanyin, L. Fangjie, B. Deyou, An advanced TiFe series hydrogen storage material with high hydrogen capacity and easily activated properties, *International Journal of Hydrogen Energy*, 15 (1990) 259-262.
- [69] H. Qu, J. Du, C. Pu, Y. Niu, T. Huang, Z. Li, Y. Lou, Z. Wu, Effects of Co introduction on hydrogen storage properties of Ti-Fe-Mn alloys, *International Journal of Hydrogen Energy*, 40 (2015) 2729-2735.
- [70] H. Leng, Z. Yu, J. Yin, Q. Li, Z. Wu, K.-C. Chou, Effects of Ce on the hydrogen storage properties of TiFe<sub>0.9</sub>Mn<sub>0.1</sub> alloy, *International Journal of Hydrogen Energy*, 42 (2017) 23731-23736.
- [71] P. Modi, K.-F. Aguey-Zinsou, Titanium-iron-manganese (TiFe<sub>0.85</sub>Mn<sub>0.15</sub>) alloy for hydrogen storage: Reactivation upon oxidation, *International Journal of Hydrogen Energy*, 44 (2019).
- [72] W. Wang, C. Chen, H. Xu, H. Li, Q. Wang, Hydrogen storage properties of Ti<sub>1.2</sub>Fe+xCa hydrogen storage alloys, *Rare Metals*, 20 (2001) 265-269.

- [73] H. Xu, C. Chen, W. Wang, G. Cai, L. Chen, Hydrogen storage properties of  $Ti_{1.2}Fe + x\%Mg$  ( $x = 1, 3, 5$ ) alloys, *Xiyou Jinshu Cailiao Yu Gongcheng/Rare Metal Materials and Engineering*, 32 (2003) 220-223.
- [74] X. Wang, R. Chen, C. Chen, Q. Wang, Hydrogen storage properties of  $Ti_xFe + ywt.\% La$  and its use in metal hydride hydrogen compressor, *Journal of Alloys and Compounds*, 425 (2006) 291-295.
- [75] H. Shang, Y. Li, Y. Zhang, Y. Qi, S. Guo, D. Zhao, Structure and hydrogenation performances of as-cast  $Ti_{1.1-x}RE_xFe_{0.8}Mn_{0.2}$  ( $RE = Pr, Sm$  and  $Nd$ ;  $x = 0, 0.01$ ) alloys, *International Journal of Hydrogen Energy*, 43 (2018) 19091-19101.
- [76] H. Shang, Y. Zhang, Y. Li, Y. Qi, S. Guo, D. Zhao, Effects of adding over-stoichiometrical Ti and substituting Fe with Mn partly on structure and hydrogen storage performances of TiFe alloy, *Renewable Energy*, 135 (2019) 1481-1498.
- [77] H. Shang, Y. Zhang, Y. Li, Y. Qi, S. Guo, D. Zhao, Investigation on gaseous and electrochemical hydrogen storage performances of as-cast and milled  $Ti_{1.1}Fe_{0.9}Ni_{0.1}$  and  $Ti_{1.09}Mg_{0.01}Fe_{0.9}Ni_{0.1}$  alloys, *International Journal of Hydrogen Energy*, 43 (2018) 1691-1701.
- [78] Y. Li, H. Shang, Y. Zhang, P. Li, Y. Qi, D. Zhao, Investigations on gaseous hydrogen storage performances and reactivation ability of as-cast  $TiFe_{1-x}Ni_x$  ( $x=0, 0.1, 0.2$  and  $0.4$ ) alloys, *International Journal of Hydrogen Energy*, 44 (2019) 4240-4252.
- [79] W. Ali, Z. Hao, Z. Li, G. Chen, Z. Wu, X. Lu, C. Li, Effects of Cu and Y substitution on hydrogen storage performance of  $TiFe_{0.86}Mn_{0.1}Y_{0.1-x}Cu_x$ , *International Journal of Hydrogen Energy*, 42 (2017) 16620-16631.
- [80] L. Zaluski, P. Tessier, D.H. Ryan, C.B. Doner, A. Zaluska, J.O. Ström-Olsen, M.L. Trudeau, R. Schulz, Amorphous and nanocrystalline Fe-Ti prepared by ball milling, *Journal of Materials Research*, 8 (1993) 3059-3068.
- [81] C.B. Jung, J.H. Kim, K.S. Lee, Electrode characteristics of nanostructured TiFe and ZrCr<sub>2</sub> type metal hydride prepared by mechanical alloying, *Nanostructured Materials*, 8 (1997) 1093-1104.
- [82] H. Hotta, M. Abe, T. Kuji, H. Uchida, Synthesis of Ti-Fe alloys by mechanical alloying, *Journal of Alloys and Compounds*, 439 (2007) 221-226.

- [83] T. Haraki, K. Oishi, H. Uchida, Y. Miyamoto, M. Abe, T. Kokaji, S. Uchida, Properties of hydrogen absorption by nano-structured FeTi alloys, *International Journal of Materials Research*, 99 (2008) 507-512.
- [84] V.Y. Zadorozhnyy, G.S. Milovzorov, S.N. Klyamkin, M.Y. Zadorozhnyy, D.V. Strugova, M.V. Gorshenkov, S.D. Kaloshkin, Preparation and hydrogen storage properties of nanocrystalline TiFe synthesized by mechanical alloying, *Progress in Natural Science: Materials International*, 27 (2017) 149-155.
- [85] H. Aoyagi, K. Aoki, T. Masumoto, Effect of ball milling on hydrogen absorption properties of FeTi, Mg<sub>2</sub>Ni and LaNi<sub>5</sub>, *Journal of Alloys and Compounds*, 231 (1995) 804-809.
- [86] C.H. Chiang, Z.H. Chin, T.P. Perng, Hydrogenation of TiFe by high-energy ball milling, *Journal of Alloys and Compounds*, 307 (2000) 259-265.
- [87] M.W. Davids, M. Lototsky, Influence of oxygen introduced in TiFe-based hydride forming alloy on its morphology, structural and hydrogen sorption properties, *International Journal of Hydrogen Energy*, 37 (2012) 18155-18162.
- [88] H. Emami, K. Edalati, J. Matsuda, E. Akiba, Z. Horita, Hydrogen storage performance of TiFe after processing by ball milling, *Acta Materialia*, 88 (2015) 190-195.
- [89] V.Y. Zadorozhnyy, S.N. Klyamkin, S.D. Kaloshkin, M.Y. Zadorozhnyy, O.V. Bermesheva, Mechanochemical synthesis and hydrogen sorption properties of nanocrystalline TiFe, *Inorganic Materials*, 47 (2011) 1081.
- [90] S.M. Lee, T.P. Perng, Microstructural correlations with the hydrogenation kinetics of FeTi<sub>1+ξ</sub> alloys, *Journal of Alloys and Compounds*, 177 (1991) 107-118.
- [91] Y. Kusadome, K. Ikeda, Y. Nakamori, S. Orimo, Z. Horita, Hydrogen storage capability of MgNi<sub>2</sub> processed by high pressure torsion, *Scripta Materialia*, 57 (2007) 751-753.
- [92] D. Leiva, A. Jorge Junior, T. Toshimi Ishikawa, J. Huot, D. Fruchart, S. Miraglia, C. Shyinti Kiminami, W. Botta, *Nanoscale Grain Refinement and H-Sorption Properties of MgH<sub>2</sub> Processed by High-Pressure Torsion and Other Mechanical Routes*, 2010.
- [93] K. Edalati, A. Yamamoto, Z. Horita, T. Ishihara, High-pressure torsion of pure magnesium: Evolution of mechanical properties, microstructures and hydrogen storage capacity with equivalent strain, *Scripta Materialia*, 64 (2011) 880-883.



- [94] L.E.R. Vega, D.R. Leiva, R.M. Leal Neto, W.B. Silva, R.A. Silva, T.T. Ishikawa, C.S. Kiminami, W.J. Botta, Mechanical activation of TiFe for hydrogen storage by cold rolling under inert atmosphere, *International Journal of Hydrogen Energy*, 43 (2018) 2913-2918.
- [95] K. Edalati, J. Matsuda, H. Iwaoka, S. Toh, E. Akiba, Z. Horita, High-pressure torsion of TiFe intermetallics for activation of hydrogen storage at room temperature with heterogeneous nanostructure, *International Journal of Hydrogen Energy*, 38 (2013) 4622-4627.
- [96] K. Edalati, J. Matsuda, M. Arita, T. Daio, E. Akiba, Z. Horita, Mechanism of activation of TiFe intermetallics for hydrogen storage by severe plastic deformation using high-pressure torsion, *Applied Physics Letters*, 103 (2013) 3902.
- [97] K. Edalati, E. Akiba, Z. Horita, High-pressure torsion for new hydrogen storage materials, *Science and Technology of Advanced Materials*, 19 (2018) 185-193.
- [98] R.W. Cheary, A.A. Coelho, J.P. Cline, Fundamental Parameters Line Profile Fitting in Laboratory Diffractometers, *Journal of Research of the National Institute of Standards and Technology*, 109 (2004) 1-25.
- [99] T. Collins, ImageJ for microscopy, *BioTechniques*, 43 (2007) S25-S30.
- [100] A.K. Singh, *Experimental Methodologies for the Characterization of Nanoparticles, Engineered Nanoparticles*, (2016), 125-170.
- [101] C. Kittel, *Introduction to Solid State Physics*, Wiley, 2004.
- [102] G.S. Rohrer, *Structure and Bonding in Crystalline Materials*, Cambridge University Press, Cambridge, 2001.
- [103] J. Duarte, S. Moreira, J. Pombo, *Implementation of a methodology for elemental analysis of sediments based on a handheld X-ray fluorescence analyzer*, 2018.
- [104] M.H. Mintz, Y. Zeiri, Hydriding kinetics of powders, *Journal of Alloys and Compounds*, 216 (1994) 159.
- [105] M. Avrami, Kinetics of phase change. I: General theory, *The Journal of Chemical Physics*, 7 (1939) 1103-1112.
- [106] Y. Pang, Q. Li, A review on kinetic models and corresponding analysis methods for hydrogen storage materials, *International Journal of Hydrogen Energy*, 41 (2016) 18072-18087.
- [107] J. Lang, M. Eagles, M.S. Conradi, J. Huot, Hydrogenation rate limiting step, diffusion and thermal conductivity in cold rolled magnesium hydride, *Journal of Alloys and Compounds*, 583 (2014) 116-120.

- [108] G.J. Zhou, S. Jin, L.B. Liu, H.S. Liu, Z.P. Jin, Determination of isothermal section of Fe-Ti-Zr ternary system at 1173 K, Transactions of Nonferrous Metals Society of China, 17 (2007) 963-966.
- [109] T.F. Fedorov, Y.B. Kuzma, The Titanium-Iron-Boron System,” Izv. Akad. Nauk SSSR, Neorg. Mater.,3(8), (1967) 1498–99 (in Russian); TR: Inorganic Materials, 8 (1967) 1307-1308.
- [110] B.H. Toby, R factors in Rietveld analysis: How good is good enough?, Powder Diffraction, 21 (2012) 67-70.
- [111] V.N. Fokin, E.E. Fokina, I.I. Korobov, B.P. Tarasov, Phase transformations in the systems Ti<sub>2</sub>Fe–H<sub>2</sub> and Ti<sub>2</sub>Fe–NH<sub>3</sub>, Russian Journal of Inorganic Chemistry, 61 (2016) 891-895.
- [112] R.J. Contieri, E.S.N. Lopes, M. Taquire de La Cruz, A.M. Costa, C.R.M. Afonso, R. Caram, Microstructure of directionally solidified Ti–Fe eutectic alloy with low interstitial and high mechanical strength, Journal of Crystal Growth, 333 (2011) 40-47.